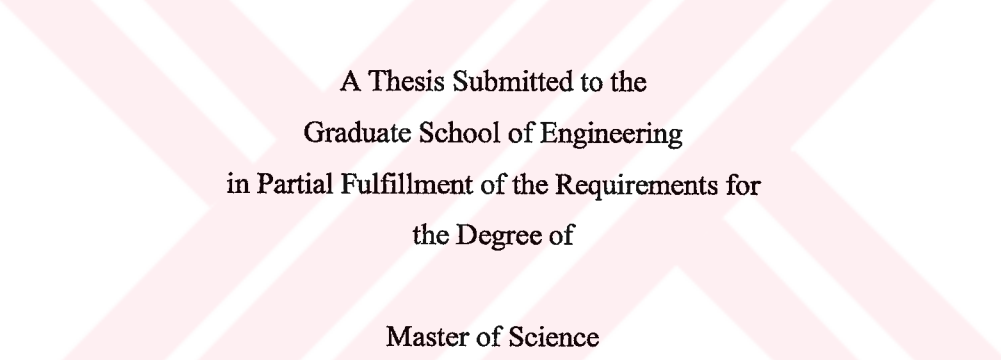


151323

Design, Modeling and Characterization of Electrostatically Actuated
Microscanners

by

Çağlar Ataman



A Thesis Submitted to the
Graduate School of Engineering
in Partial Fulfillment of the Requirements for
the Degree of
Master of Science

in

Electrical & Computer Engineering

151323

Koç University

November, 2004

Koç University
Graduate School of Sciences and Engineering

This is to certify that I have examined this copy of a master's thesis by

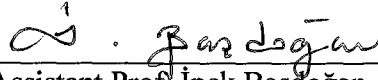
Çağlar Ataman

and found that it is complete and satisfactory in all respects,
and that any and all revisions required by the final
examining committee have been made

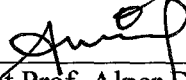
Committee Members:



Assoc. Prof. Hakan Ürey



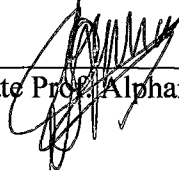
Assistant Prof. İpek Başdoğan



Assistant Prof. Alper Demir



Dr. Harald Schenk



Associate Prof. Alphan Sennaroğlu

Date:

06.12.2004



*anne ve babama...
kaymadigunuz her soru icin
binlerce kez tesekkuler.*

ABSTRACT

Microscanners produced using MEMS technology enable light manipulation at a size, precision, and speed that is far beyond the limits of conventional machining. Microscanners that utilize 1D, 2D, and even 3D scanning are gaining popularity and have found many applications in display, imaging, and telecommunication applications. Accurate modeling, effective testing and characterization of dynamic behavior of these devices are becoming increasingly important to reduce the design time and cost while optimizing performance.

This thesis focuses on developing new modeling and experimental characterization techniques for torsional microscanners that are energized using an array of parallel-plate electrostatic actuators called *comb-actuators*. Models developed in the thesis are then applied to design a novel Fourier Transform Spectrometer (FTS) based on a tunable rectangular diffraction grating, which is formed using an out-of-plane comb-actuator.

Major accomplishments of this research include (a) development of numerical models for analysis of hysteretic frequency response, parametric and subharmonic resonances, damping effects, and stability regions of comb-driven microscanners; (b) development of analytical models for predicting nonlinear system characteristics listed in (a) under small harmonic excitation condition; (c) development of experimental setups for microscanner characterization and validation of numerical and analytical models.

Keywords: Microscanner, comb actuator, parametric resonance, numerical modeling, analytical modeling

ÖZET

MEMS teknolojisi ile üretilen mikro-tarayıcılar ışığın standart üretim teknikleri ile üretilen yapıların ulaşabileceğinin çok ötesindeki boyut, hassasiyet ve hızlarda yönlendirilebilmesini sağlamaktadır. Tek boyutlu, iki boyutlu ve hatta üç boyutlu tarama yapabilen mikro-tarayıcılar giderek daha çok ilgi çekmekte ve başta görüntü alma, görüntü oluşturma ve haberleşme olmak üzere bir çok yeni uygulama alanı bulmaktadır. Bu yapıların dinamik davranışlarının deneysel olarak tanımlanması ve doğru bir şekilde modellenmesi, mikro-tarayıcı temelli sistemlerin tasarım süre ve maliyetlerinin azaltılıp performanslarının olabildiğince artırılması açısından giderek daha fazla önem kazanmaktadır.

Bu tez, taraklı erişim düzeneği (comb actuator) adı verilen bir dizi paralel-levha elektrostatik erişim düzeneği (electrostatic actuator) vasıtasıyla harekete geçirilen burulma-modu (torsional mode) mikro-tarayıcıları için yeni modelleme ve deneysel karakterize etme yöntemleri üzerine yoğunlaşmaktadır. Tez kapsamında geliştirilen modelleme teknikleri düzlem-dışı moda çalışan taraklı erişim düzeneklerini ayarlanabilir dağılıma ızgarası (diffraction grating) olarak kullanan yeni bir Fourier Dönüşümü Tayfölçeri tasarımı için kullanılmıştır.

Bu araştırmanın önemli bilimsel sonuçları şöyle sıralanabilir: (a) tarak-tahrikli (comb-actuated) mikro-tarayıcıların histerik frekans davranışları, parametrik ve alt-harmonik rezonansları, sönümlenme etkileri ve kararlılıkları için sayısal modellerin geliştirilmesi; (b) ilk şıkta bahsi geçen doğrusal olmayan sistem özelliklerinin düşük genlikli harmonik tahrik koşulu altında analitik olarak modellenmesi; (c) mikro-tarayıcıların test ve karakterize edilmesi ve sayısal-analitik modellerin doğrulanması amaçlı deney düzeneklerinin kurulması.

Anahtar kelimeler: Mikrotarayıcı, taraklı erişim düzeneği, parametrik rezonans, sayısal modelleme, analitik modelleme.

ACKNOWLEDGEMENTS

I would like to express my sincere gratitude to my thesis advisor Dr. Hakan Ürey for his extensive support and encouragement throughout the past two years. It has been an invaluable experience to take part in the foundation and growth of the –almighty- Optical Microsystems Laboratory. As project partners, I would like to thank Dr. Alexander Wolter and Dr. Harald Schenk from Fraunhofer IPMS for allowing me to spend a summer in their institute, and for sharing their vast experience on microscanners with me during our helpful discussions. Our other collaborator in this project was Microvision, Inc. They provided some of the test and measurement equipment that were vital for the experimental part of this work. I thank them for their support. I also appreciate SPIE and Koc University College of Engineering for supporting me through travel grants that enabled me to participate some international conferences. I also would like to thank to Dr. Alphan Sennaroğlu, Dr. Alper Demir, and Dr. İpek Başdoğan and Dr. Harald Schenk for taking part in my thesis committee. As my colleagues, many thanks go to Arda, Olgaç, Hamdi, and Özgür for making those long hours spent in the lab as enjoyable as they were.

The Fellowship: Topçu, RuNe, Boru and CS... Even though you were not around as much, it was good to know that you were somewhere out there.

As a veteran and devoted metalhead, I have to express my appreciation to all those great metal bands for their incredible music that makes life more bearable.

Last, but definitely not least, many thanks go to my mom, dad and my brother. None of these would be possible without them.

TABLE OF CONTENTS

List of Tables	xi
List of Figures	xii
Chapter 1: Introduction	1
1.1. Applications of Microscanners.....	1
1.2. Actuation of Microscanners.....	5
1.2.1 Electrostatic Actuation.....	5
1.2.2 Electromagnetic Actuation.....	6
1.2.3 Thermal Actuation.....	7
1.2.4 Piezoelectric Actuation.....	8
1.3. Main Contributions and Thesis Outline.....	8
Chapter 2: Operational and Structural Properties of Comb-Driven Microscanners	11
2.1. Introduction.....	11
2.2. Device Structure.....	11
2.3. Device Operation.....	13
2.4. Microfabrication.....	14
2.5. Natural Vibration Modes.....	16
2.6. Actuation Mechanism.....	18
2.6.1 Characteristics of Comb Actuator.....	18
2.6.2 DC Pull-In.....	22
2.7. Damping Mechanism.....	24

Chapter 3:	Dynamic Behavior: Experimental Results and Numerical Simulations	27
3.1.	Introduction.....	27
3.2.	Numerical Modeling Basics.....	28
3.3.	Frequency Domain Characteristics.....	30
3.3.1	Harmonic Excitation.....	30
3.3.2	Square-wave Excitation.....	32
3.4.	Time Domain Characteristics.....	33
3.4.1	Transient Response.....	34
3.4.2	Steady-State Response.....	35
3.5.	Voltage Domain Characteristics.....	36
3.6.	Conclusions.....	37
Chapter 4:	Dynamic Behavior: Analytical Modeling	38
4.1.	Introduction.....	38
4.2.	Steady-State Behavior.....	39
4.3.	Stability Curves.....	44
4.4.	Effect of Cubic Nonlinearity.....	47
4.5.	Conclusions.....	47
Chapter 5:	Conclusions	48
Appendix A:	Experimental Setups	49
A.1.	Dynamic Mirror Characterization Setup.....	49
A.1.1	Layout and Operation.....	49
A.1.2	Frequency Response Measurements.....	52
A.1.3	Stability Measurements.....	52
A.1.4	Voltage Domain Measurements.....	52
A.1.5	Damping Measurements.....	53
A.2.	Transient Response Measurement Setup.....	53
A.2.1	Layout and Operation.....	53
A.2.2	Damping Measurements.....	55
A.3.	Out-of-plane Mode Frequency Measurement Setup.....	55

Appendix B: Mode Frequency Formulas for Microscanners	58
References	61
Publications	66



LIST OF TABLES

2.1	Dimensions of the E201 microscanner.....	13
2.2	Mode Frequencies of E201: Comparison of analytical, experimental and FEA results.....	17
2.3	Mode Frequencies of SL28 – Comparison of analytical, experimental and FEA results.....	17
2.4	Measured quality factors of different microscanners.....	25
3.1	Coefficients of equation of motion of E201 at two different ambient pressure levels.....	29
B.1	Natural frequency for five fundamental oscillation modes for torsional scanners.....	59
B.2	Mass and mass moment of inertia for different mirror (M_m is the mass of the mirror and M_f is the mass of one flexure) shapes.	60

LIST OF FIGURES

1.1-1	The Texas Instruments DLP: Mirror arrays and pixel structure.....	2
1.1-2	Retinal Scanning Display Technology of Microvision, Inc uses a 2D MEMS microscanner.....	3
1.1-3	Hand-held barcode readers are potential applications of MEMS microscanners.....	3
1.1-4	A stand alone two-axis microscanner for optical switching applications.....	4
1.1-5	Two common structures for N-to-N OXC. (a) An N ² -to-N OXC with N ² mirrors. (b) An N-to-N OXC with 2N mirrors.....	4
1.2-1	Simplest capacitive actuator: Parallel plate actuator.....	5
1.2-2	Comb drive capacitive actuators on a silicon micromirror. Comb drives increase the force produced by electrostatic actuators by increasing the effective electrostatic interaction area.....	6
1.2-3	A one dimensional electromagnetic microscanner.....	7
1.2-4	Cross section of a thermally actuated microscanner. The cantilever beam holding the silicon mirror is bimorph consisting of two materials with different thermal expansion coefficients. Heating and cooling of the device bends the cantilever beam and actuates the mirror.....	8
2.2-1	General layout for (a) 1D, (b) 2D comb-driven.....	11
2.2-2	Structure of the isolation trenches. The zigzag structure of the trenches enhances mechanical stability.....	12
2.2-3	Photograph of the electrode combs.....	12
2.2-4	Dimensional parameters of a box-shaped microscanner.....	12
2.3-1	Driving schemes for (a) 1D, (b) 2D microscanners.....	13
2.3-2	Oscillation and excitation waveform. The solid line represents the deflection angle θ of the mirror plate and the dashed line represents the square-wave excitation waveform.....	14

2.4-1:	Schematic view of the 2D scanner device defining the cross-section C-D for the fabrication sequence of. The line starts at C, passes the open isolation trench defining the anchor of the movable frame, the electrode gap of the mirror plate, the filled isolation trench defining the anchor of the mirror plate, the electrode gap of the movable frame and ends at D.....	15
2.4-2	Process flow for the microfabrication of a 2D microscanner along the cross section of Fig. 2.4.1.....	15
2.5-1	Five fundamental vibration modes of a box shaped microscanner.....	16
2.6-1	Capacitance-deflection and capacitance-change—deflection characteristics of a torsional mode comb-drive actuator.....	19
2.6-2	FEA results of Capacitance-deflection analysis of horizontal sliding mode.....	21
2.6-3	Capacitance-deflection and capacitance-change—deflection characteristics of a horizontal rocking mode comb-drive actuator.....	22
2.6-4	Capacitance-deflection and capacitance-change—deflection characteristics of a vertical sliding mode comb-drive actuator.....	22
2.6-5	Capacitance-deflection and capacitance-change—deflection characteristics of an in-plane mode comb-drive actuator.....	23
2.6-7	Electrostatic forces acting on a comb finger moving in in-plane lateral mode.....	23
2.6-8	Mechanical and electrostatic forces in a in-plane lateral mode comb actuator at three different voltage levels.....	24
2.7-1	Decay rate of free oscillations vs. Deflection angle for various IPMS scanners.....	26
3.2-1	Capacitance vs. deflection and capacitance change vs. deflection plots of a torsional comb-driven microscanner.....	29
3.2 2	Typical hysterical frequency response curve of a torsional microscanner.....	30
3.3-1	Experimental frequency response data at (a) atmospheric pressure (760 Torr), (b) at 30 mTorr. Excitation signal is a square-rooted sine with 20 Vp-p for both plots.....	31
3.3-2	Comparison of simulation (dashed line) and experimental (solid line) results for the 1st order parametric resonance in atmospheric pressure.....	32

3.3-3	Experimental frequency response data at 760 Torr (1 Atm) and with 20 Vp-p square wave excitation. Number of observable parametric resonances is 8, due to the higher harmonics in the square wave excitation.....	33
3.4-1	Transient response of the device, when $f_{ext} > f_2$ (stable region). (a) Experimental data (b) Simulation result.....	34
3.4-2	Transient response of the device, when $f_{ext} \approx f_2$ (boundary of the stability curve). (a) Experimental data (b) Simulation result.....	34
3.4-3	Excitation and device response (a) in the first order resonance; (b) in the second order resonance.....	35
3.4-5	Alternating oscillation phenomenon at higher order resonances with 590Hz square wave excitation. (a) Experimental result; (b) Simulation results.....	35
3.5-1	Maximum scan angle vs. excitation amplitude with square-wave, sinusoidal and square-root sine excitation. Experimental results belong to E201.....	36
3.5 2	Voltage domain characteristics of IPMS scanners. (a) Effect of excitation voltage on frequency response. (b) Maximum scan angle vs. excitation amplitude characteristics of different IPMS scanners. Both results are taken from.....	37
4.4-1	Stability tongues for E201 at atmospheric pressure. Up to 25V only two parametric resonances were observable, due to high damping.....	46
4.4-2	Stability tongues for E201 at 30 mTorr, and analytical approximations. Due to much lower damping, 5 parametric resonances could be observed..	
A.1-1	Sketch of the dynamic micromirror characterization setup.....	50
A.1-2	Schematic of the electronic circuitry in Figure A.1.....	50
A.1-3	Timing convention used in the scan angle derivation.....	51
A.1-4	Photos of the experimental setup.....	51
A.1-6	Sample quality factor measurement data taken with DMCS.....	52
A.2-1	Sketch of the Transient Response Measurement Setup.....	54
A.2-2	Sample transient response measurement data.....	55
A.4-1	Sketch of the LDV measurement setup.....	56

4-2	LDV measurement points for out-of-plane mode characterization.....	56
B-1	(a) Torsional resonant scan mirror suspended with two flexure beams that are fixed at the ends, figure inset shows flexure rectangular cross-section and coordinate axis; (b) five fundamental vibration modes for the torsional scanner, which are rotation around x-axis (torsional), translation in z-axis (out-of-plane translation), translation in y-axis (in-plane sliding), rotation around y-axis (out-of-plane rocking), and rotation around z-axis (in-plane rocking).....	58



Chapter 1

INTRODUCTION

Integration of optics with Micro-Electro-Mechanical Systems (MEMS) gave birth to a new engineering discipline called Micro-Opto-Electro-Mechanical Systems (MOEMS), which gave engineers many new opportunities for light manipulation using precisely machined micromechanical devices. Recent improvements in the microfabrication technologies, together with the cheaper and faster opto-electronic devices, capabilities of MOEMS significantly increased. Today, with increasing interest and investments from industry and research foundations, MOEMS are becoming an established engineering field, whose major impact is soon to be seen in many fields, like telecommunications, display and imaging systems, medicine, optical lithography, spectroscopy and etc.

This thesis mainly deals with resonant MOEMS microscanners developed for display and imaging applications that use comb-drive actuation. Main contributions of this thesis are in modeling of the actuator dynamics, development of a number of MEMS metrology tools for microscanner experimental characterization and design of a novel MOEMS spectrometer. To give a general overview of the microscanners as an active field of research and development, Section 1.1 describes various microscanner applications and Section 1.2 describes different microscanner actuation mechanisms. The outline of this thesis is discussed in Section 1.3.

1.1 Applications of Microscanners

Micromirror and Microscanner technologies are a major part of the MOEMS discipline today. A *microscanner* is a tiny movable mirror that can scan or steer a laser beam in 1D, 2D or 3D. Due to their promising mechanical, optical and electrical properties, there has been a significant amount of research and development efforts on microscanner and micromirror technologies. As a result, microscanners have been one of the first MOEMS devices that are used in commercial products. Today, these systems offer effective solutions for problems from different engineering professions. Some of the major application areas of micromirror and microscanner technologies are given below.

Display and Imaging: The fundamental application field of MEMS microscanners is the display and imaging systems. Fast scanning speeds and high scan angles achieved by the microscanner technologies make them a good candidate for this type of applications. There are a wide variety of display applications that utilize MEMS micromirrors and microscanners. Some of those technologies even led to very successful commercial products.

Texas Instruments' Digital Light Processor[®] (DLP) technology is the most famous and successful commercial MOEMS product aimed at projection display market. DLP is a MEMS chip with an array of about 1 million movable micromirrors that operate digitally (ON-OFF), instead of continuous scanning [1]. There are many projection displays in the market that uses the DLP as the main display unit.

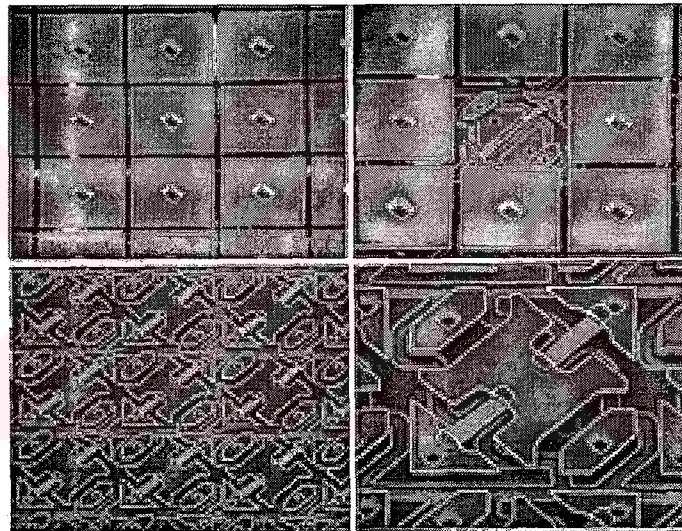


Figure 1.1-1: The Texas Instruments DLP[®]: Mirror arrays and pixel structure (Photo courtesy of Texas Instruments)

A second MOEMS display product example is the Retinal Scanning Display (RSD). This is a head mounted micro-display developed by Microvision, Inc. The device utilizes a single two-dimensional MEMS microscanner for scanning video data onto the retina of the user [2]. It is a see-through display that augments the displayed image onto what is actually seen by the user. Performance constraints for a microscanner based high-resolution display system like RSD require a very careful design of the microscanner. The trade-offs and critical issues of microscanner design for display systems are challenging, and have been the subject of several articles [3-4].

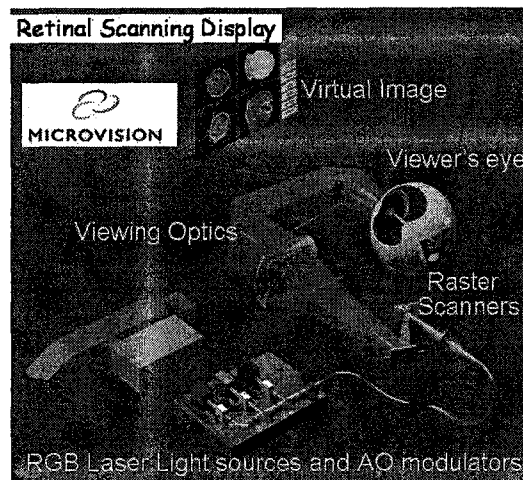


Figure 1.1-2: Retinal Scanning Display Technology of Microvision, Inc uses a 2D MEMS microscanner. (Photo courtesy of Microvision, Inc)

In addition to the mentioned display applications, microscanner technologies are also utilized in imaging systems. Barcode reading is maybe the most important imaging application of today's microscanner technologies. They offer effective solutions for reading both regular 1D and new 2D barcodes. Higher scanning frequency and lower power consumption of microscanners compared to conventional technologies make microscanners an attractive choice for compact, hand-held barcode readers [5].

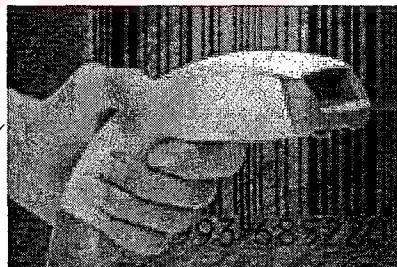


Figure 1.1-3: Hand-held barcode readers are potential applications of MEMS microscanners

One major issue about barcode scanners may be the mechanical reliability, since a hand-held device may experience high shocks due to dropping, hitting, etc.

In addition to the mentioned devices, there are various other technologies that use microscanners for display and imaging applications [6-10].

Optical Switching: Another major application field of optical MEMS is the telecommunications industry. There has been an enormous interest and investment on fiber-

optic switching technologies during the exceptional growth of telecommunications market in the late 90's. However, market conditions since 2000 slowed down the progress in this area. Despite this drawback, optical MEMS are still very attractive and promising technology for the telecommunications infrastructure of the future.

As a good tool for manipulating the direction of propagation of light, microscanners play an important role in optical switching of fiber-optic data lines. Optical switching is significantly advantageous, since it allows optical routing of signals at nodes, without having to convert the signal into electrical than back into optical signal, thereby maintaining high data bandwidths during transmission. Typical switching times for optical switches are in the order of few msec. There are many different applications that employ a stand-alone or an array of MEMS microscanners. Single mirrors are generally used for routing for one-to-N fiber coupling, while array of mirrors are very suitable for optical cross connects (OXC). Figure 1.1-4 shows a stand alone microscanner designed for optical switching; Figure 1.1-5 describes two popular architectures for N-to-N fiber OXC using micromirror arrays.



Figure 1.1-4: A stand alone two-axis microscanner for optical switching applications (photo courtesy of Lucent Technologies, Inc.)

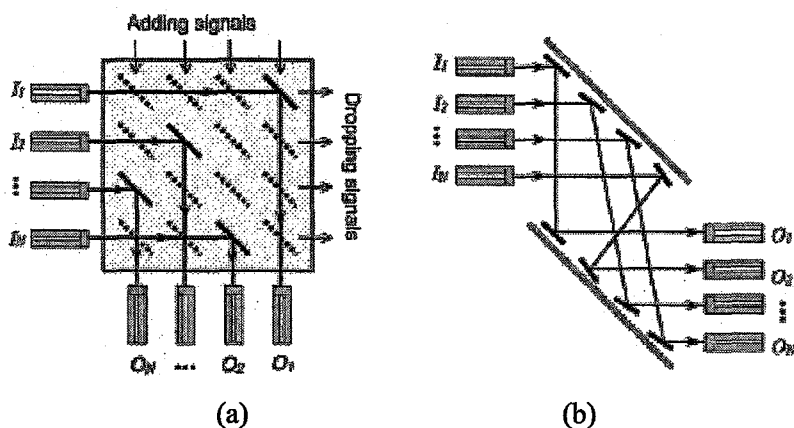


Figure 1.1-5: Two common structures for N-to-N OXC. (a) An N-to-N OXC with N^2 mirrors. (b) An N-to-N OXC with $2N$ mirrors (picture taken from [11]).

There has been an enormous amount of research going on to develop fast, reliable and high capacity optical switching MEMS devices. A list of publications reporting some of the most successful devices for telecommunications applications can be found in the references section [11-14].

Diversity of MOEMS and microscanner applications is increasing day-by-day. Some other crucial applications of MEMS microscanners and micromirrors that were not mentioned here include endoscopic optical coherence tomography [15], optical storage [16], adaptive optics [17], and interferometry [18].

1.2 Actuation of Microscanners

Microscanners are generally categorized based on their actuation mechanism, which is the energy conversion mechanism used to convert a certain form of energy into mechanical motion. There are many different actuators that exploit different physical principles. A good actuator should have a high efficiency in this energy conversion, in order to induce enough amount of mechanical motion. A number of common actuation mechanisms utilized in MEMS microscanners are overviewed here. More detailed information on the design and operation principles of these actuators can be found in the corresponding references.

1.2.1 Electrostatic Actuation

This type of actuation is also known as *capacitive actuation*, since the operation principle depends on the capacitance variation in a microsystem. Figure 1.2-1 is a sketch of a capacitive actuator in its simplest form.

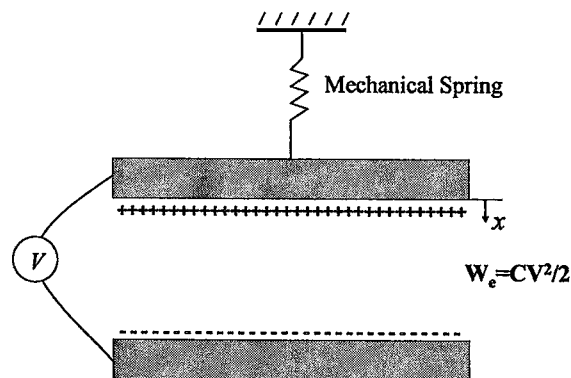


Figure 1.2-1: Simplest capacitive actuator: Parallel plate actuator

Total stored energy in a capacitive actuator of any geometry is given as

$$W_e = \frac{1}{2} CV(t)^2 \quad (1.1)$$

where, C is the total capacitance and $V(t)$ is the time varying potential on the actuator. Then, the actuation force produced by a capacitive actuator can be written as

$$F = \frac{\delta W_e}{\delta x} = \frac{1}{2} \frac{dC}{dx} V(t)^2 \quad (1.2)$$

where x is the displacement of the actuator along the fundamental degree-of-freedom. (1.2) implies that for maximizing the produced force, the total capacitance of the actuator should be very high. Comb-drive capacitive actuators are a good solution for increasing the effective capacitance between complementary surfaces. Figure 1.2-2 shows a typical comb drive actuator. The microscanners investigated throughout this thesis are actuated with this type of structures.

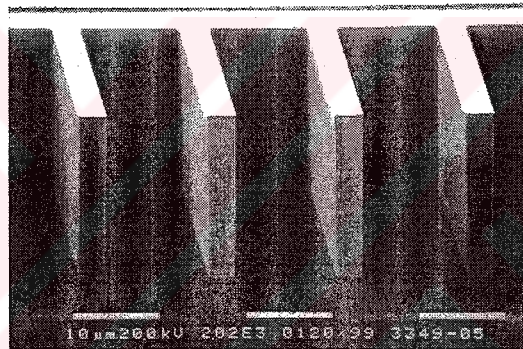


Figure 1.2-2: Comb drive capacitive actuators on a silicon micromirror. Comb drives increase the force produced by electrostatic actuators by increasing the effective electrostatic interaction area (photo courtesy of Fraunhofer, IPMS).

Electrostatic actuation is the most popular actuation mechanism for microscanners, since it allows the designer to integrate the actuator to the actual device in a compact manner. There are microscanners actuated with parallel plate [19-20] or comb-drive [21-22] capacitive actuators.

1.2.2 Electromagnetic Actuation

A certain amount of force is exerted on a current carrying conductor placed in a magnetic field (Lorentz Force). This force is proportional to the magnetic field intensity, the current passing through the conductor and the length of the conductor inside the magnetic field. There are various microscanners reported in the literature that uses this electromagnetic principle for device actuation [23-24].

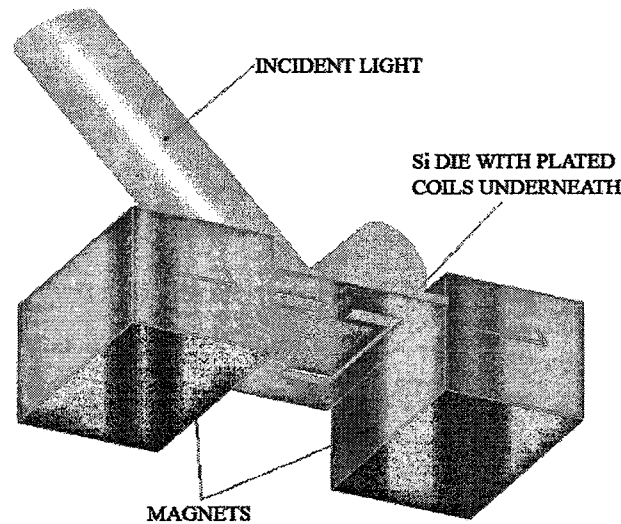


Figure 1.2-3: A one dimensional electromagnetic microscanner

Figure 1.2-3 shows the layout of a typical electromagnetic microscanner. The permanent magnets on the sides create a constant magnetic field. When a current is passed through the coils on the moving plate, an in-plane electromagnetic force is exerted on the mirror, which leads to torsional deflection. High current density on the mirror and powerful magnets are required for torque maximization. There are also other electromagnetic actuation techniques which are not as popular, such as moving permanent magnet actuators [25], and permalloy actuators [26-27].

1.2.3 Thermal Actuation

When two materials of different thermal expansion coefficients are put together as a bimorph structure – cantilever or a plate-, a change in the temperature will bend this structure. This is the same principle that is used in thermostats. There are numerous applications that utilize this principle for a microscanner actuation [28-29]. Most important design challenge for such a structure is to maximize the thermal coefficient mismatch between the two materials of the bimorph structure. This requires a good material selection in the design phase. Two major drawbacks of thermal actuators are the high response times, and the sensitivity to thermal noise. Figure 1.2-4 shows a typical thermally actuated microscanner.

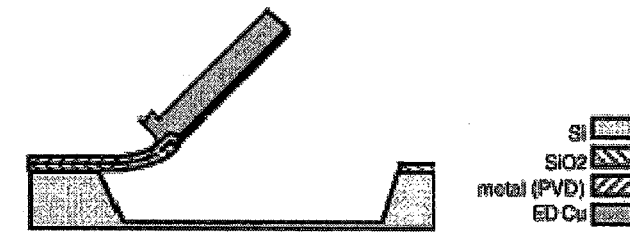


Figure 1.2-4: Cross section of a thermally actuated microscanner. The cantilever beam holding the silicon mirror is bimorph consisting of two materials with different thermal expansion coefficients [28]. Heating and cooling of the device bends the cantilever beam and actuates the mirror.

1.2.4 Piezoelectric Actuation

“Crystals which acquire a charge when compressed, twisted or distorted are said to be piezoelectric. This provides a convenient transducer effect between electrical and mechanical oscillations [30]”. With proper mechanical design this transducer effect can be utilized for microscanner design [31]. Piezoelectric actuators provide high precision motion, however they require very high potentials for small deflection amounts. There are examples of microscanners that use deposited PZT piezoelectric films and take advantage of high mechanical gain in resonant scanners to obtain good performance [32].

1.3 Main Contributions and Thesis Outline

This thesis focuses on the dynamic characterization of electrostatic comb-driven torsional microscanners. The project was carried out as a collaboration of Koc University-Optical Microsystems Laboratory, Fraunhofer Institute for Photonic Microsystems (IPMS), Germany, and Microvision, Inc., USA. Fraunhofer IPMS developed the comb-drive actuated torsional microscanners and shared their know-how on experimental test and characterization of microscanners. Microvision, Inc. provided some of the test and measurement equipment used in the experimental characterization works. The work in this thesis resulted in one journal article (submitted to Journal of Microelectromechanical Systems) and three conference articles. Full articles are included in Appendix D.

Main contributions of the thesis can be summarized as:

- An analytical and a numerical model for predicting the dynamic behavior of torsional comb-driven microscanners is built for the first time
- Various optical measurement methods for full characterization of MOEMS microscanners are presented

In Chapter 2, structural and operational properties of the microscanners fabricated by Fraunhofer IPMS are investigated. IPMS scanners are comb-drive actuated devices and they are designed to operate in the torsional mode. However, comb actuators are multi degree-of-freedom structures, and they can induce motion in different orientations. Actuation mode of the comb-drives is determined by the excitation scheme and modal frequencies of the device. Chapter 2 focuses on the finite element and analytical modal analyses of microscanners to determine the natural frequencies of oscillations in different orientations. The driving characteristics of the comb actuators in different modes are also investigated using FEA, numerical and analytical analysis methods. This chapter also explores other microscanner properties such as damping, electrical isolation, microfabrication, etc.

The investigation of the dynamic behavior of comb-driven microscanners in torsional mode is given in Chapter 3. This chapter also presents the numerical model, which is based on the device characteristics examined in Chapter 2. Frequency-domain, time-domain and voltage-domain responses of the device are explored separately. For behavior in each domain, numerical and experimental characterization results are given together for model validation.

In Chapter 4, an analytical treatment of the dynamic behavior of IPMS scanners is presented. In 4.2, the solution for the simplest case –no damping, no nonlinearity- is encountered. Following sections introduce those omitted effects into the solution and comments on the impact of those effects on the dynamic behavior. The model built with this treatment is utilized to predict the stability characteristics of the microscanners.

Chapter 2

OPERATIONAL AND STRUCTURAL PROPERTIES OF COMB-DRIVEN MICROSCANNERS

2.1 Introduction

Analytical, numerical, and experimental studies in this thesis explore the characteristics of microscanners fabricated by Fraunhofer Institute for Photonic Microsystems (IPMS), Dresden-Germany [33-35]. IPMS microscanners are promising candidates for various display and imaging applications, since they can reach very high deflection angles with relatively low voltages. Moreover, the electrostatic actuation principle of these devices provides very low power consumption, which is a crucial issue in hand-held portable device applications, such as barcode readers.

In this chapter a detailed insight on the structural and electrical properties of these devices is presented. Section 2.2 explains the general structure and design variations of microscanners. Basics of the operation principle are given in 2.3. In 2.4, the microfabrication process is summarized. Although IPMS microscanners are designed to be operated in torsional mode, with proper excitation schemes, other mechanical modes of the devices can be excited. The natural frequencies of these modes are of great importance, since a poor modal separation may lead to malfunctioning devices. Section 2.5 explores the modal characteristics of microscanners. Finite Element Analysis (FEA) results and analytical mode frequency estimations are presented in this section. Damping mechanism in the microscanners is an important issue that strongly affects the dynamic behavior. Section 2.7 presents an investigation of the damping characteristics of the device.

2.2 Device Structure

All IPMS microscanners have a single-crystalline silicon structure. Flexure beams, comb fingers, and isolation trenches are defined on a silicon wafer using silicon etching techniques. Figure 2.2-1 show the general layout for one and two dimensional microscanners.

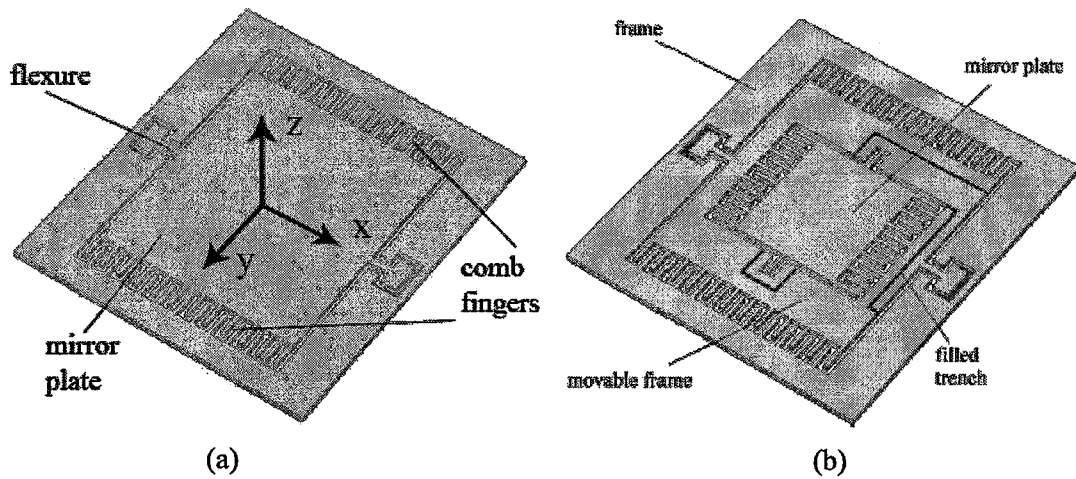


Figure 2.2-1: General layout for (a) 1D, (b) 2D comb-driven microscanners (Figure 2.2-1b taken from [33]). The axis convention in (a) will be addressed frequently in the following sections.

The key structural elements of one-dimensional (1D) microscanners are the aluminum-coated, movable, reflective mirror, the fixed and movable comb-fingers, and the torsional flexure beams that suspend the moving mirror to the outer fixed frame. In two-dimensional (2D) devices, another gimbal-mounted frame is built around the moving mirror to provide another axis of rotation. The movable mirror is coated with aluminum to enhance optical reflectivity. Size and shape of the mirror may vary for different device design. IPMS have fabricated many microscanners that are square, round or elliptical in shape, and range from $300\ \mu\text{m} \times 300\ \mu\text{m}$ to $2\ \text{mm} \times 2\ \text{mm}$ in size.

Capacitance change due to rotation of the comb-fingers generates the necessary torque for actuation of the reflective mirror around the flexure axis. In order to produce torque (or force, depending on the mechanical operation mode) out of the actuators, complementary comb fingers should be of different electrostatic potential. It is the isolation trenches that provide electrical isolation between different areas of the device. The shape of these trenches is shown in Figure 2.2-2. Since these devices operate in relatively high frequencies and deflect significantly from their rest positions, high inertial forces are exerted on them during operation. In order to enhance the mechanical stability of the 2D microscanners, and prevent a possible breakdown during operation, the isolation trenches of this type of devices are designed in a zigzag shape.

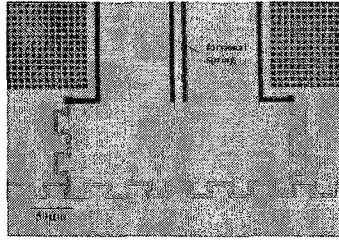


Figure 2.2-2: Structure of the isolation trenches of 2D microscanners. The zigzag structure of the trenches enhances mechanical stability (picture taken from [33]).

One of the main advantages of IPMS microscanners is the integrated compact actuators that can produce high torque. Figure 2.2-3 shows the structure of these comb fingers. The fingers of the driving electrode have a width of $3.6 \mu\text{m}$, the fingers of the mirror plate are $2 \mu\text{m}$ wide. The bright area is a part of the Al-coated silicon mirror plate. On the right hand side of the mirror plate the silicon layer is perforated to reduce the damping by the surrounding gas.

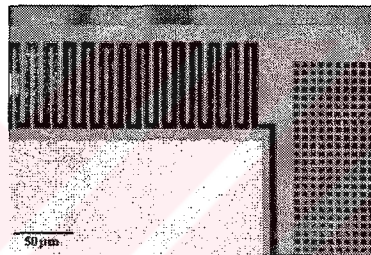


Figure 2.2-3: Photograph of the electrode combs [34].

Modeling efforts in this thesis are valid for all comb-driven microscanners. However, for the sake of brevity, modeling results of only one specific scanner will be presented in the following chapters, which is a boxed shape microscanner with a code number E201. Figure 2.2-4 defines the dimensional parameters of a box-shaped microscanner. Table 2-1 lists of dimensional parameter values for E201.

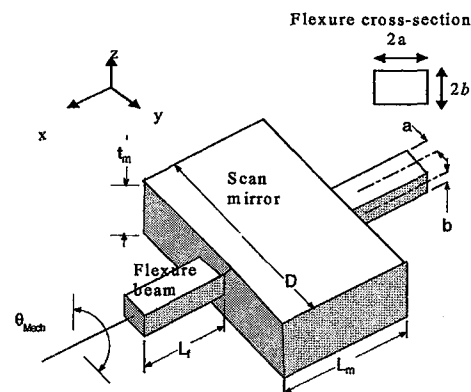


Figure 2.2-4: Dimensional parameters of a box-shaped microscanner.

Table 2-1: Dimensions of E201 microscanner

Parameter	Symbol	Value
Mirror Length	L_m	2.00E-03
Mirror Width	D_m	2.00E-03
Thickness	t_m	3.00E-05
Flexure Half Width	a	7.30E-06
Flexure Half Thickness	b	1.50E-05
Flexure Length	L_f	5.89E-04
Comb Finger Length	L_c	6.57E-05
Comb Thickness	W_c	2.20E-06
Gap Between Fingers	g	2.20E-06

2.3 Device Operation

In the fundamental mode (torsional mode), the mirror plate of 1D scanners rotate around the axis passing through the flexure beams (horizontal scanning). In 2D devices, in addition to the movable mirror plate, the mirror frame is also suspended to another fixed frame via two-flexure beams directed perpendicular to the mirror flexures. This movable frame also has comb actuators, and can be rotated along the axis passing through its own flexures (vertical scanning). The natural frequencies of vertical and horizontal scans are chosen to be sufficiently away from each other; therefore mechanical coupling between two axes is prevented. This is a critical issue for imaging and display applications, where independent 2D scanning of different horizontal and vertical frequencies is necessary.

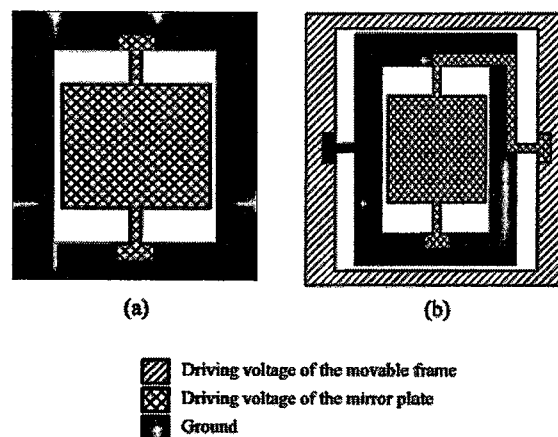


Figure 2.3-1: Driving schemes for (a) 1D, (b) 2D microscanners.

Figure 2.3-1 shows the driving schemes for both 1D and 2D scanners. Different areas of the devices that are of different electrical potential are isolated from each other by isolation

trenches. These trenches are fabricated by first etching a $1\mu\text{m}$ thick channel on the silicon structural layer using ASETM process, then covering the side walls of the channel by 90 nm thick insulating oxide, and at last filling the channel with LPCVD-polysilicon. Due to the low thickness of these trenches, maximum allowed driving potential is about 40 V. Potentials beyond this limit permanently damages the trench structure and the device ceases to operate.

The actuation principle is based on the capacitance change in the comb-drives; therefore a slight difference between the mechanical and electrical rest positions is required to start the oscillations from stationary position. Required asymmetry is so slight that even process variations in microfabrication is enough to start the oscillations. Figure 2.3-2 illustrates the mirror rotation and the driving signal at fundamental resonance. Electrostatic torque in the system is present only if the driving voltage is in the ON state, and it pulls the device towards rest position together with the spring force. In the fundamental resonance, mirror oscillation frequency is half the excitation frequency and oscillations in this regime are called *subharmonic oscillations*, which are discussed in detail in subsequent chapters.

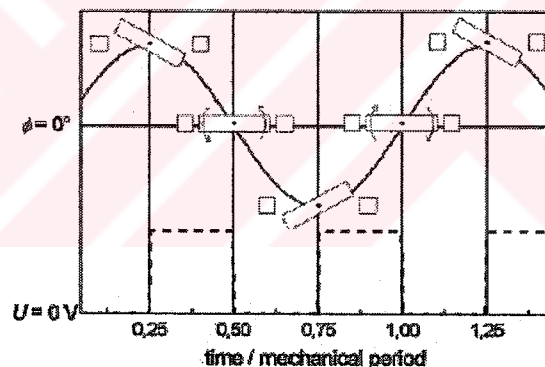


Figure 2.3-2: Oscillation and excitation waveform. The solid line represents the deflection angle θ of the mirror plate and the dashed line represents the square-wave excitation waveform.

2.4 Microfabrication

Both 1D and 2D scanning-micromirrors are fabricated in a CMOS compatible process starting with a (100)-SOI-wafer with a top layer thickness of $30\mu\text{m}$. The buried oxide layer serves as an etch stop. Therefore, the thickness of the mechanical elements is well defined. The fabrication sequence is detailed in Figure 2.4-2 for a cross-section along C-D as shown in Figure 2.4-1. For the generation of the filled isolation trenches in the mechanical active areas, $1\mu\text{m}$ wide trenches with almost perpendicular sidewalls are etched in the $30\mu\text{m}$ thick top layer using the ASETM-process. Due to the selectivity of the process etching stops at the buried oxide

layer (Figure 2.4-2a). The sidewalls of the trenches are wet-oxidized at a temperature of 960 °C resulting in a 90 nm thick isolation layer. After that the trenches are filled with LPCVD (Low pressure Chemical Vapor Deposition) -polysilicon. The 900 nm thick polysilicon layer on the wafer surface is removed by chemical mechanical polishing (CMP). The 90 nm-oxide is etched back in a HF-solution (Figure 2.4-24b). As a consequence of this sequence the polysilicon filling is 90 nm embossed on the wafer surface (not shown in Figure 2.4-2). An oxide and a metal layer are deposited for the formation of the wiring (not shown in Figure 2.4-2). On the backside of the wafer, a hard mask consisting of an oxide and a nitride layer is patterned for the anisotropic etch later in the process. Further, a 50 nm thick layer of aluminum is deposited on the silicon mirror plate to enhance the reflectivity (Figure Figure 2.4-2c). The substrate underneath the mechanical elements is removed in a TMAH-solution at a temperature of 75°C (Figure 2.4-2d). After that the buried oxide is etched in a HF solution. Finally, the mechanical elements, the electrode comb and the anchors of the movable frame are defined by a deep silicon etch (ASE™) process [33].

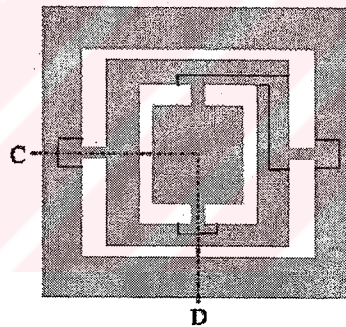


Figure 2.4-1: Schematic view of the 2D scanner device defining the cross-section C-D for the fabrication sequence of Fig. 4. The line starts at C, passes the open isolation trench defining the anchor of the movable frame, the electrode gap of the mirror plate, the filled isolation trench defining the anchor of the mirror plate, the electrode gap of the movable frame and ends at D [33]

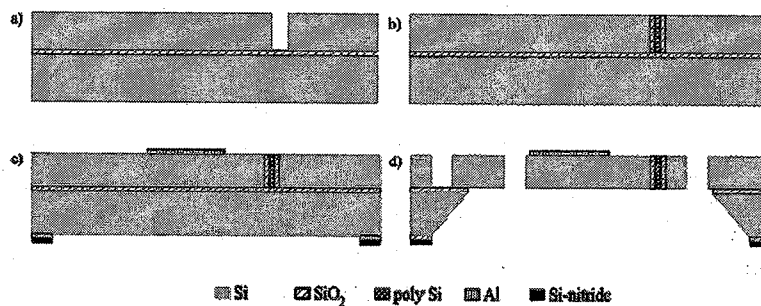


Figure 2.4-2: Process flow for the microfabrication of a 2D microscanner along the cross section of Fig. 2.4.1. [34]

2.5 Natural Vibration Modes

Basic one-axis torsional scanner geometry and the first five fundamental vibration modes are illustrated in Figure 2.5-1. The figure presents the FEA (ANSYS[®]) modal analysis results for the 1D E201 scanner. Two-axis scanners can be obtained by cascading two scan frames, one inside the other. Mirror vibration frequency requirements determine the flexure beam dimensions that suspend the mirror. Thus, predicting the frequencies for the torsion and other fundamental vibration modes is critical. If torsion is the desired mode, which is the case for microscanners, other modes are often undesired and should be well separated from the torsional mode frequency and its harmonics.

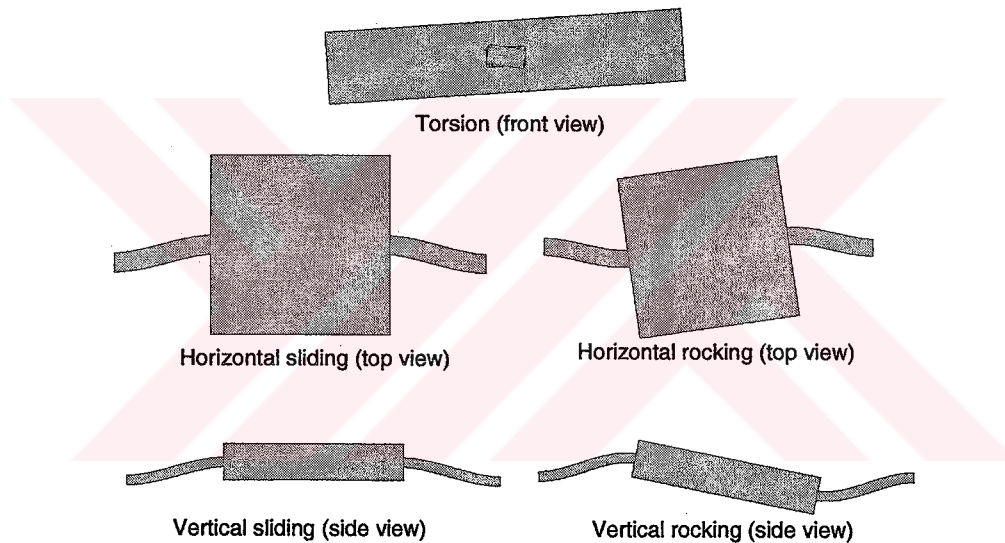


Figure 2.5-1: Five fundamental vibration modes of a box shaped microscanner.

One can calculate the natural frequencies of each vibration mode by using appropriate displacement or rotation angle variable, spring constant, and effective mass or effective mass moment of inertia terms [36]. As an example, the natural frequency for the out-of-plane torsional mode with angular frequency ($\omega=2\pi f$) can be calculated by:

$$\frac{d^2\theta}{dt^2} + \omega^2\theta = 0 \quad (2.1)$$

$$\omega = 2\pi f = \sqrt{K_s / I_m} \quad (2.2)$$

where K_s is the spring constant for the mode and I_m is the total mass moment of inertia of the scan mirror for the particular vibration mode. A set of analytical expressions for the spring

stiffness, effective mass/mass moment of inertia and natural frequency of the first five natural modes of a box and elliptical shaped micromirrors are given in Appendix B. Those expressions give a powerful way to perform quite accurate modal analysis without time consuming FEA simulations. Table 2-2 presents a comparison of mode frequency calculations for E201 scanner.

Table 2-2: Mode Frequencies of E201 – Comparison of analytical, experimental and FEA results.

Mode	Analytical	FEA	Experimental
Torsional	1049	1266	1069
Horizontal Sliding	3746	3723	-
Horizontal Rocking	7698	6610	-
Vertical Sliding	5986	5908	-
Vertical Rocking	17509	15525	-

A setup was built in the laboratory to experimentally measure the higher mechanical modes of the microscanner. Detailed information on the layout and operation of the setup is given in Appendix A.3. The heart of the setup is a Polytec PDV100 Laser Doppler Vibrometer. The maximum frequency measurable with PDV100 was 22 KHz. Although this range was enough to measure first five modes of E201, the scanner was broken by the time the setup was built. Another microscanner (code number: SL28), which is a 1D device with round mirror, was used in measurements. Table 2-3 gives the measurement results of SL28 together with the analytical and FEA simulation data.

Table 2-3: Mode Frequencies of SL28 – Comparison of analytical, experimental and FEA results

Mode	Analytical	FEA	Experimental
Torsional	203	240	270
Horizontal Sliding	1237	1345	-
Horizontal Rocking	1976	1934	-
Vertical Sliding	20613	16580	16420
Vertical Rocking	46807	39876	-

The microscanners are designed to be operated in the torsional mode. However, due to multiple degrees of freedom of the comb-drive actuators, they can also be excited in other modes. Next section discusses the details of comb-drive actuation.

2.6 Actuation Mechanism

2.6.1 Characteristics of Comb-Drive Actuators

Electrostatic actuation has always been an attractive choice for microsystems. Simple operation principle of this type of actuators enabled engineers to employ integrated and compact actuation structures in microsystems. However, electrostatic actuators had a major drawback. Due to the very small size of the microsystems, effective capacitances between the surfaces to be actuated were very small. Therefore, very high operation voltages were required to get sufficient displacement. Comb-drive actuators are a good solution for this problem. The large number of comb-like fingers in this type of actuators significantly increases the mutual capacitance within a small area, which leads to a drastic decrease in the operation voltages. For many occasions, the use of comb-drives pulled operation voltages down to standard CMOS compatible range, which is an extremely important advantage in the sense of design flexibility and cost. Today comb-driven electrostatic actuation is commonly used in different microelectromechanical systems, such as tunable capacitors [37], mechanical filters [38-40], and optical switches [41].

As in all electrostatic actuators, the total force (torque) produced by a set of comb actuators is given by the following formulas:

$$F(x) = 2N \frac{1}{2} \frac{dC}{dx} V(t)^2$$

$$M(\theta) = 2N \frac{1}{2} \frac{dC}{d\theta} V(t)^2$$
(2.3)

where x is the displacement in sliding modes, θ is the angular displacement in torsional modes, $dC/dx(d\theta)$ is the rate of change of capacitance with respect to the displacement variable, N is the total number of comb fingers and $V(t)^2$ is the periodic driving signal. The characteristic of actuator's force (torque) function is the fundamental factor that determines the dynamic behavior of the comb-driven device; therefore capacitance-displacement characteristics of the actuator at different oscillation modes should be accurately determined for successful modeling. For the first four mechanical modes of E201, capacitance-displacement and capacitance-change—displacement plots are given below. An additional mode, which is not within the first five modes of microscanners is also investigated. This mode corresponds to translation along x - axis, and may lead to lateral pull-in. We have run Finite Element Analysis simulations using FEMLAB[®] to obtain capacitance-deflection characteristics. To obtain the

displacement derivative of capacitances, first a high order polynomial was fitted to the capacitance data, and then this fitting polynomial is differentiated using MATLAB. Simulations were run for a single comb finger, for the sake of computational efficiency. For a set of fingers, the curves should be multiplied by the number of fingers.

Torsional Mode (rotation around y -axis): This is the fundamental operation mode of microscanners. FEMLAB simulation results for this mode are given in Figure 2.6-1. Capacitance is the highest in the rest position, and begins to drop quickly as tilt angle increases. This fast decrease in the capacitance slows down after the fingers disengage from each other. Beyond disengagement, capacitance is only due to the fringing fields. Capacitance change rate in this mode depends heavily on the angular displacement; therefore the force is also displacement dependant. This dependence has a significant effect on the dynamic behavior of torsional comb-driven devices, which will be explored in details in the following chapters.

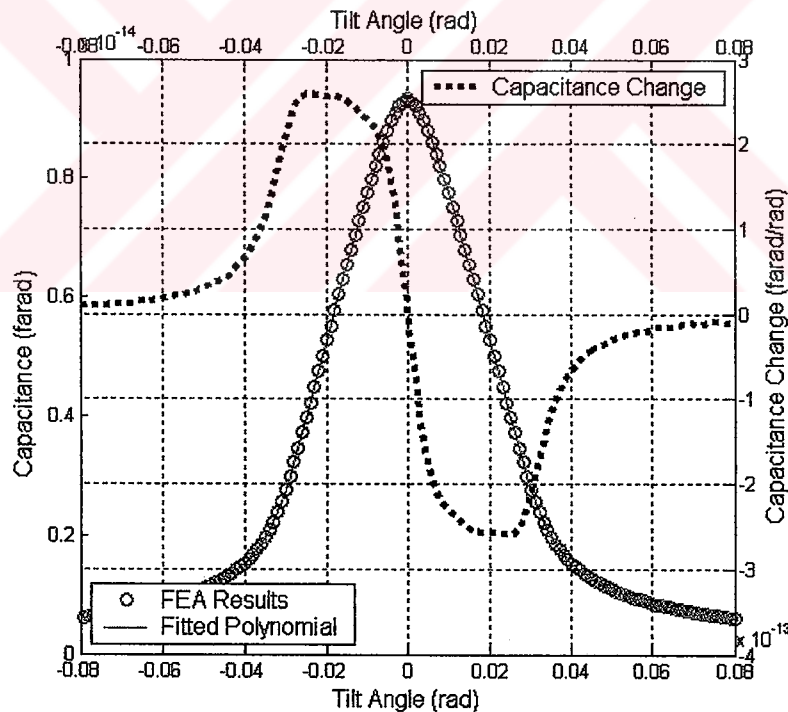


Figure 2.6-1: Capacitance-deflection and capacitance-change—deflection characteristics of a torsional mode comb-drive actuator.

Horizontal Sliding Mode (translation along $-y$ axis): Simulation results for this mode are presented in Figure 2.6-2. There are two capacitive effects that determine the shape of the

capacitance-deflection curve of this mode. When the fingers are almost completely engaged (left-hand-side of the plot), the capacitance between the tip of the finger and the frame is dominant, due to very low gap. As fingers disengage, this capacitance shrinks exponentially and becomes negligible when compared to the side-wall capacitances. Beyond that point, the decrease in the capacitance is linear with the displacement. This means that, except a short range where fingers are almost completely engaged, the rate of change of capacitance is independent of displacement. When comb actuators are designed to be operated in this region, the associated device exhibit simple harmonic oscillatory behavior. Hence, comb actuators in this mode are very appropriate for applications like tunable capacitors, mechanical filters or resonators, where linearity is a desired property.

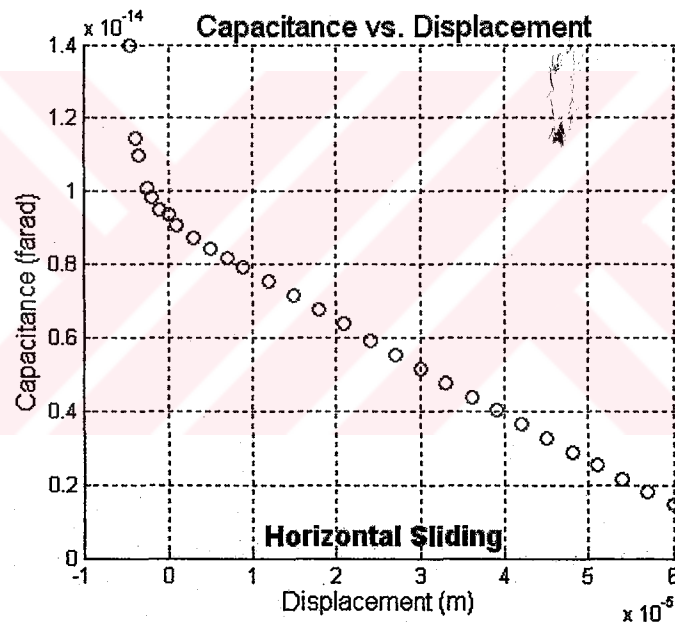


Figure 2.6-2: FEA results of Capacitance-deflection analysis of horizontal sliding mode

Horizontal Rocking Mode (rotation around z- axis): Figure 2.6-3 gives the FEA results for horizontal rocking mode. Capacitance-deflection curve for this mode is an even function. Due to the exponential increase in the capacitance change with increasing deflection, motion in this mode may cause pull-in, which means the sticking of the complementary fingers. Details of this phenomenon are discussed at the end of this section.

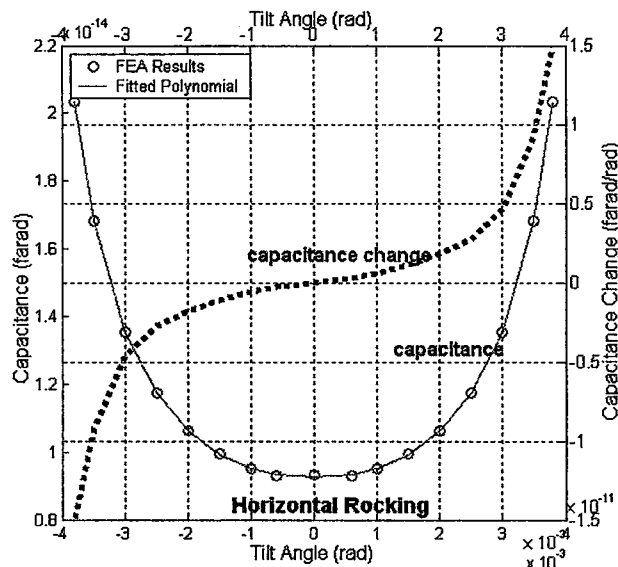


Figure 2.6-3: Capacitance-deflection and capacitance-change—deflection characteristics of a horizontal rocking mode comb-drive actuator.

Vertical Sliding Mode (translation along $-z$ axis): This mode is also called out-of-plane translation mode. As Figure 2.6-4 reveals, characteristics of this mode is very similar to the torsional mode. Due to this similarity, dynamic behaviors of these two modes are very alike.

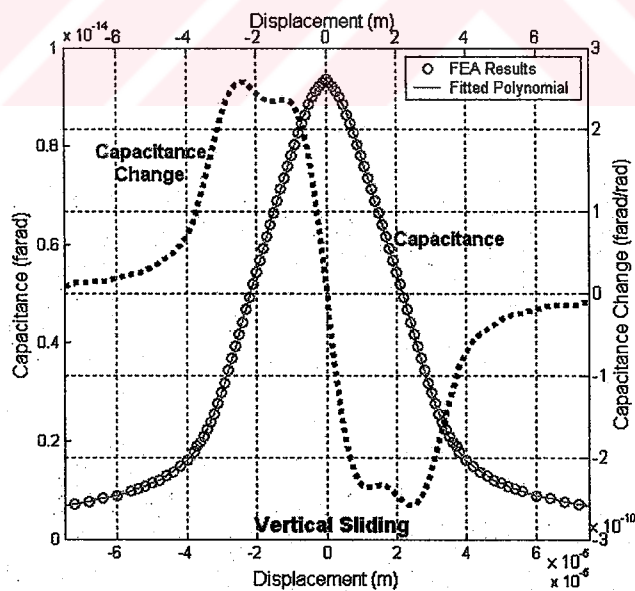


Figure 2.6-4: Capacitance-deflection and capacitance-change—deflection characteristics of a vertical sliding mode comb-drive actuator.

In-plane Lateral Mode (translation along x-axis): This mode is difficult to excite in IPMS microscanners, since the flexures have very high stiffness in longitudinal direction. However, some other comb-driven MEMS devices may easily be excited in this mode. Capacitance-deflection characteristic in this mode is plotted in Figure 2.6-5.

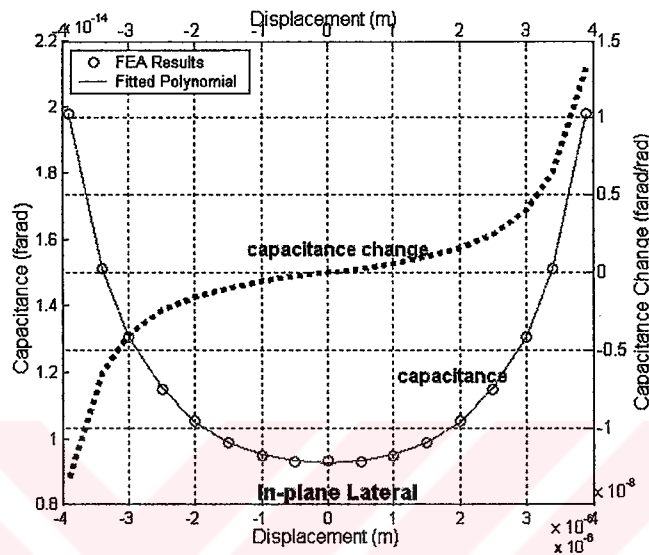


Figure 2.6-5 Capacitance-deflection and capacitance-change—deflection characteristics of an in-plane lateral mode comb-drive actuator.

Comparison of Figure 2.6-3 and Figure 2.6-5 shows that, characteristics of the horizontal rocking and in-plane lateral mode comb actuators are similar. In both modes, electrostatic force increases unboundedly with increasing displacement. This leads to a problem called *lateral DC pull-in*. When lateral pull-in occurs, complementary comb fingers stick together and create a short circuit, which causes device breakdown. In a good microscanner design, the spring stiffness along these modes of motion should be as high as possible, so that no pull-in occurs at moderate operation voltages. Next, the lateral DC pull-in phenomenon is discussed.

2.6.2 DC Pull-In Instability:

Pull-in is a crucial issue in electrostatic actuation. Especially, for gap-closing parallel-plate capacitive actuators, pull-in is the limiting factor of travel range. There have been extensive studies on understanding and suppressing this drawback of electrostatic actuators [42-43]. Generally, comb actuated devices do not suffer from pull-in, since the fundamental degree-of-freedom is not in gap closing direction. However, for some comb-driven devices with suitable spring structures, lateral pull-in may also occur. Figure 2.6-6 shows the forces acting on a

laterally moving comb finger. When fringing effects are neglected, the net electrostatic force on a single comb finger is given by

$$F_e = (F_{e1} - F_{e2}) = \frac{\epsilon AV}{2} \left[\frac{1}{(g-x)^2} - \frac{1}{(g+x)^2} \right] \quad (2.4)$$

where ϵ is the permittivity of air, A is the total overlap area between the fingers, V is the DC potential between the complementary fingers, g is the initial gap between the fingers, and x is the lateral displacement. This lateral displacement produces a restoring force due to the springs, which is given by the expression

$$F_m = K_s x \quad (2.5)$$

where K_s is the spring stiffness along the displacement. Figure 2.6-7 plots these functions for two different DC drive signals.

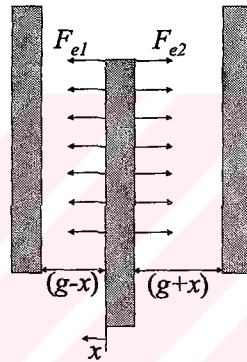


Figure 2.6-6: Electrostatic forces acting on a comb finger moving in in-plane lateral mode.

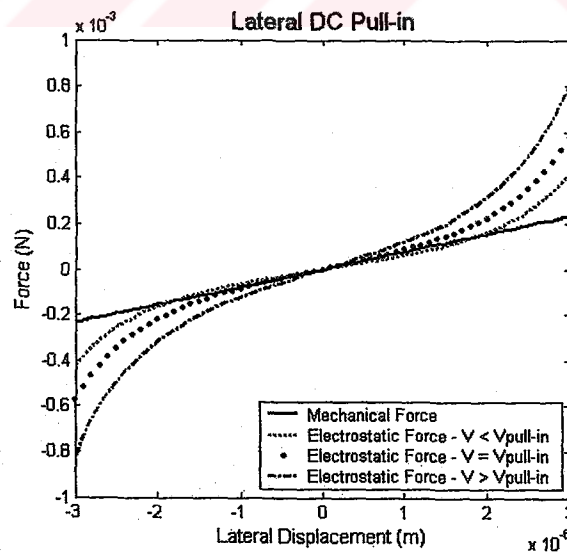


Figure 2.6-7: Mechanical and electrostatic forces in a in-plane lateral mode mode comb actuator at three different voltage levels.

For relatively low voltages, electrostatic and mechanical forces have three equilibrium points, one of which is the rest position ($x=0$), as expected. When the system is at rest, a small change in the position (due to fabrication tolerances, shock or electrical noise) will disturb the equilibrium state. Since in the neighborhood of this equilibrium point mechanical force is stronger than electrostatic attraction, the system will again reach equilibrium. Therefore, the rest position is a stable equilibrium point. The situation is different when the system is at other two equilibrium states, since a small increase in the displacement will increase the electrostatic force more than the mechanical restoring force, and lead to pull-in. Thus, those states are unstable equilibriums. As the DC potential between the fingers is increased, unstable equilibriums come closer to the rest position. At a critical voltage, which is called pull-in voltage (V_{PI}), the rest position becomes the single equilibrium, which is unstable. At $V=V_{PI}$ slope of the electrostatic force at $x=0$ is equal to the slope of the mechanical force; in other words, two curves are tangent to each other. Beyond the pull in voltage, the system is always unstable. Figure 2.6-7 illustrates the graphical relation between the mechanical and electrostatic forces for three different voltages.

2.7 Damping Mechanism

Alike all MEMS devices, dynamic behavior of a microscanner is significantly affected by the amount of damping. Thus, it is a critical issue to accurately determine the amount and characteristics of the damping mechanism in a microscanner. Damping is the dominant factor that limits the oscillation amplitude of a comb-driven microscanner. The air between the comb fingers and beneath the moving mirror plate exerts an opposite force to the moving device. This resistive force grows together with increasing mirror velocity, and limits the maximum mirror displacement. In vacuum environments, the amount of damping is very low and the microscanner can reach very high scan angles; however, due to difficult manufacturing processes and low reliability, it is not desirable to operate microscanners in vacuum.

A widely used figure of merit for the amount of damping present in a microsystem is the *quality factor* (Q). The relation between the quality factor and the damping constant in the equation of motion is given by

$$b = \frac{I_m \omega_0}{Q} \quad (2.6)$$

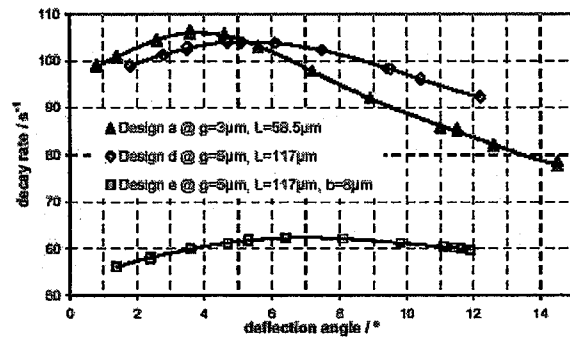
(2.6) implies that the higher the quality factor is, the lower is the damping. Two different experimental techniques were utilized to measure the damping in microscanners. The details of these techniques are given in Appendices A.1 and A.2. Measured quality factor values of the microscanners that were available are given in the following table:

Table 2-4: Measured quality factors of different microscanners. All devices mentioned in the table are comb-driven microscanners manufactured by Fraunhofer IPMS. They possess the 2D microscanner structure mentioned earlier in this chapter. All devices, except E201, have circular mirrors of radius 1.5mm.

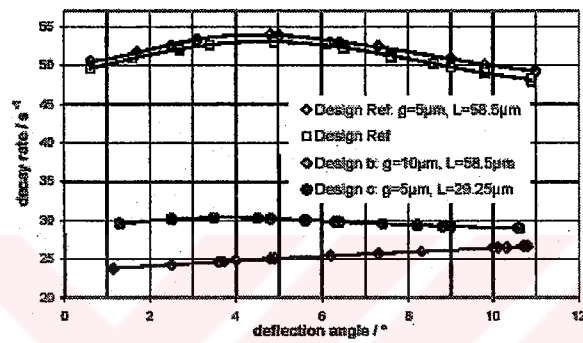
Scanner Code	Quality Factor	Natural Frequency
E201	22	2140 Hz
CB02 (2D) Horizontal	30	3426 Hz
DA63 (1D)	6	805 Hz
DA63 (2D)-Vertical	25	2615 Hz

For comb-driven microscanners, the fundamental contribution to the damping is from the comb fingers. Due to the thin gaps between the fingers, a significant viscous damping is present there. However, since the gap between the fingers is different when the fingers are completely engaged or disengaged during torsional operation, the damping is not constant throughout the entire oscillation range. The constant quality factor measured in the experiments is a value that averages out the damping mechanism. A recent work by Fraunhofer IPMS gives a model for the damping in comb driven microscanners. Figure 2.7-1 shows the dependence of the damping to the deflection angle of the mirror.

Figure 2.7-1 shows that damping changes with deflection angle, however this dependence is not drastic. Therefore, the constant damping approximation is a good way to incorporate the effects of damping into a numerical or analytical model, without introducing further complexity.



(a)



(b)

Figure 2.7-1: Decay rate of free oscillations vs. Deflection angle for various IPMS scanners (figures taken from [44])

Chapter 3

DYNAMIC BEHAVIOR: EXPERIMENTAL RESULTS AND NUMERICAL SIMULATIONS**3.1 Introduction**

Dynamic behavior of a MEMS device refers to the characteristics of system response to excitations of various time and frequency domain characteristics. Regardless of the type of specific application, design of a microscanner based system always requires good understanding and modeling of the dynamic behavior. Device models that are capable of predicting the device response within sufficient accuracy provide a powerful intuition that saves significant amount of design and engineering effort. For instance a 2D microscanner that is to be employed in a display application should have a very high θD (maximum scan angle \times scanner size) product and definite horizontal and vertical scanning frequency for high performance operation. A good model for a microscanner would tell the designer how promising a specific device design is in satisfying the demands of such an application.

It was shown in the previous chapter, that the nature of the force (torque) produced by the comb-drive actuators depends on the operation mode of the device. In in-plane sliding mode, the force induced by the actuator is independent of the displacement of the combs, and the actuator exhibits a simple harmonic oscillatory (SHO) behavior. As all other second order harmonic oscillators, in-plane mode comb actuators have their fundamental resonance at the mechanical natural frequency of the system. Detailed study of this type of comb-driven devices is available in the literature [45-49]. Due to the displacement dependent torque, time and frequency domain behavior of a torsional comb-driven microscanner is significantly different from the dynamics of a linear resonant oscillator. In this chapter, a numerical model for torsional, comb-driven microscanners is presented. This model is utilized to predict different frequency and time domain characteristics of a 2mm x 2mm square-mirror IPMS microscanner (IPMS code: E201). Numerical results in this chapter are given together with experimental measurement results for model validation. Various experimental setups were built as a part of

this thesis work for microscanner characterization. Appendix A gives comprehensive information on the schematics and operation principles of those setups.

The organization of this chapter is as follows: Section 3.1 explores the basics of the numerical model, and how to perform simulations with it. Following section deals with the frequency-domain characteristics of the device. Experimental and simulation data on the response of the device to various excitation schemes is presented. Transient and steady-state responses are explored in 2.4. In section 2.5, the relation between the angular displacement and driving voltage amplitude is investigated. The last section of this chapter deals with the stability characteristics.

3.2 Numerical Modeling Basics

First step of numerical modeling is forming the equation of motion. The equation of motion for the torsional microscanner was given in Chapter II, and is also repeated here.

$$I_m \frac{d^2\theta}{dt^2} + b \frac{d\theta}{dt} + K_f \theta = M(\theta) \quad (3.1)$$

where, I_m is mass moment of inertia, b is the damping constant, K_f is the torsional stiffness of the springs, and $M(t, \theta)$ is the time and displacement dependant torque function. Although this equation is written specifically for the torsional mode of the microscanner, equations of motion for the other modes are also in the same form. However, this single degree-of-freedom model requires that the natural frequencies for the mechanical modes are sufficiently away from each other. Modal analysis results presented in the previous chapter showed that this condition is satisfied for the microscanner of interest.

Numerical simulations are performed by numerically solving the equation of motion using MATLAB[®] ODE solvers. In order to be able to obtain accurate numerical results, values of the parameters in (3.1) should be computed accurately. For determining the mass moment of inertia and spring stiffness of different modes, some analytical expressions are available. The numerical analyses in this thesis utilize those expressions, which are listed in Appendix B. Another way to determine the stiffness and moment of inertia is to run Finite Element (FEA) simulations. This technique may give more accurate results than analytical expressions; however, FEA simulations are very time-consuming. Analysis of damping mechanism in microscanners is done in Chapter II. Although the damping in these devices is not constant, but depends on the angular displacement, an average resultant damping term can be experimentally determined. Details of the experimental damping measurement procedure are given in

Appendix A.1 and A.2. Last feature to be determined in (3.1) is the torque function. Force or torque produced by the comb actuators in various modes of operation were also investigated in the preceding chapter. A twentieth order polynomial fitted to the capacitance—tilt-angle function in order to obtain close form expression of torque function. Figure 3.2-1 plots the capacitance-change—deflection function once more as a reminder.

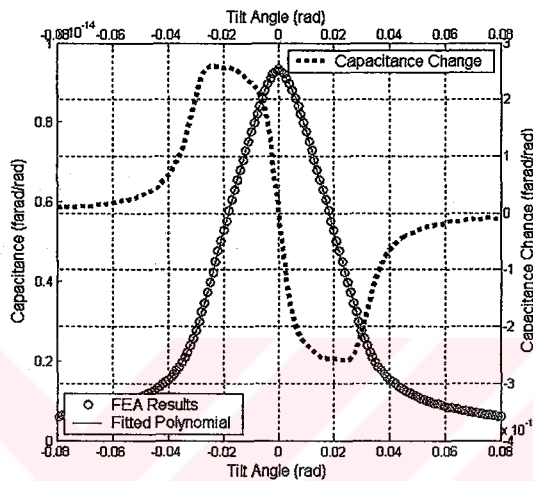


Figure 3.2-1: Capacitance vs. deflection and capacitance change vs. deflection plots of a torsional comb-driven microscanner

Table 3-1 lists the equation of motion parameters computed in two different ambient pressures.

Table 3-1: Coefficients of equation of motion of E201 at two different ambient pressure levels. Moment of inertia and spring stiffness are calculated using analytical expressions given in Appendix B; damping constant and the quality factor are determined experimentally.

Pressure(Torr)	I_m (kg.m)	b (N.s/m)	K_f (N/m)	Q
760 Torr	9.32E-14	4.21E-13	4.28E-06	22
30 mTorr	9.32E-14	2.87E-11	4.28E-06	1250

For numerical methods, the choice of initial conditions of the system parameters is of great importance. For nonlinear systems, this dependence on the initial conditions may be drastic. Therefore, the numerical simulations should have appropriate initial conditions. Figure 3.2-2 shows that the behavior of a typical torsional microscanner when the input frequency is steadily increased or decreased is significantly different. Between two jump frequencies, there exist two stable solutions of the system, and it is the initial conditions that determine which one is the actual solution that the oscillations will converge to. An initial For decreasing sweep

simulations, the initial condition is larger than the maximum scan angle, and the simulation converged to the solution with larger oscillation amplitude.

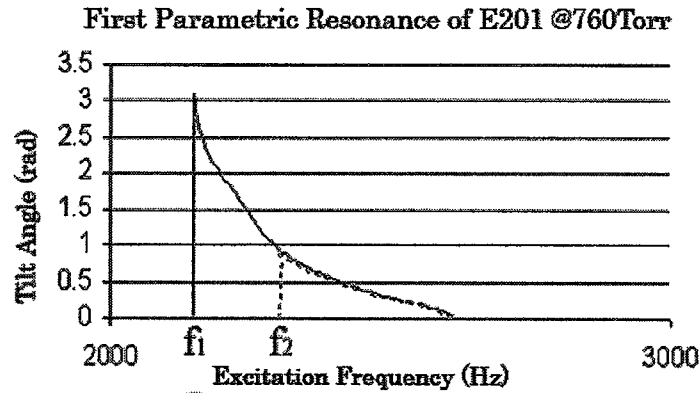


Figure 3.2-2: Typical hysterical frequency response curve for a torsional microscanner.

3.3 Frequency Domain Characteristics

Experimental results presented in this section are obtained by using the *Dynamic Microscanner Characterization Setup*. Detailed information on the design and operation of this setup is given in Appendix A.1.

3.3.1 Excitation with a Rooted- Sinusoid

The square dependence of torque to excitation implies that when the microscanner is driven by a sinusoidal potential of period T , the equation of motion would have periodic coefficients of periods T and $2T$. Therefore, in order to remove the second harmonic terms from the equation of motion, the excitation signal should be a square-rooted sinusoid ($V = A\sqrt{\cos(\omega t) + 1}$). During experiments, an arbitrary signal generator (Agilent 33250A) was used to obtain the square-rooted sinusoidal signal.

Due to the nonlinear parametric nature of the microscanners, the amount of deflection at a certain frequency depends on the initial conditions. Therefore, the frequency of the excitation has been increased or decreased quasi-statically to scan the appropriate part of the spectrum. Figure 3.3-1a and Figure 3.3-1b show the frequency response curves for rooted-sine excitation at atmospheric pressure (760 Torr), and at 30 mTorr, respectively. Figure 3.2-1 focuses into the first parametric resonance of Figure 3.3-1 and plots the numerical simulations results on top of the experimental data. The curves are significantly different from the frequency response of a

typical harmonic oscillator, which has a single resonance near the natural frequency of the system. Most remarkable feature of the frequency response of the microscanners is the *hysterical behavior*. The path traced on the tilt-angle (θ)—drive-frequency (f) curve when frequency is increased quasi-statically from a lower frequency is different than the case, in which the frequency is swept down from a higher frequency. The interval between the two jump frequencies f_1 and f_2 is called the *unstable region* of the response curve, since the oscillations in this region can be triggered if and only if the frequency is swept down from a higher frequency, but not from rest position. In other words, if the device is somehow stopped within this region, the oscillations can not be restored. Jump in the oscillation amplitude at the boundaries of the unstable region (f_1 and f_2) is extremely abrupt; sharper than 10^{-3} Hz, which was the measurement resolution.

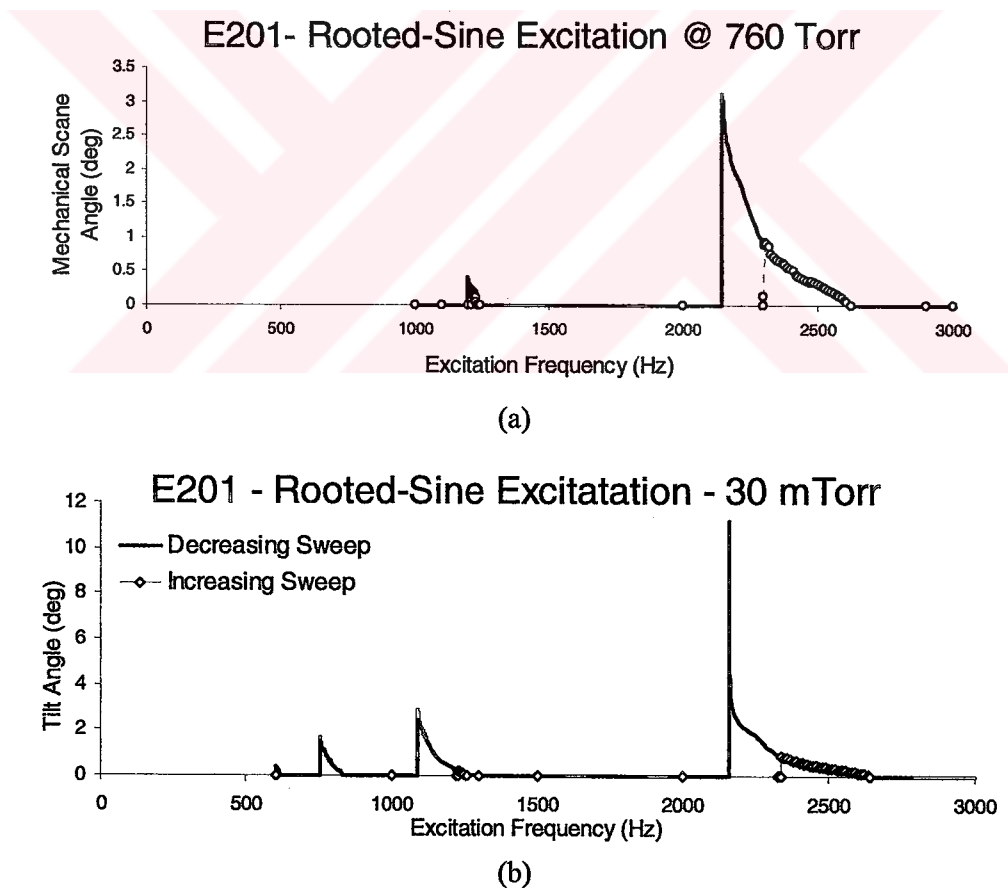


Figure 3.3-1: Experimental frequency response data at (a) atmospheric pressure (760 Torr), (b) at 30 mTorr. Excitation signal is a square-rooted sine with 20 V_{p-p} for both plots

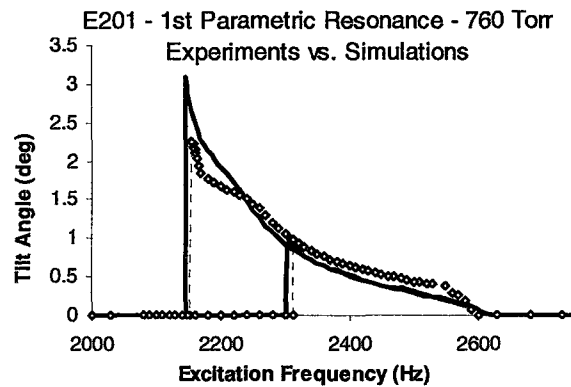


Figure 3.3-2 Comparison of simulation (dashed line) and experimental (solid line) results for the 1st order parametric resonance in atmospheric pressure.

Figure 3.3-1a indicates that in atmospheric pressure, the device has two separate resonances, of which the fundamental one is located around twice the mechanical resonance frequency (f_r). At 30 mTorr, the number of observed resonances is increased to five. Moreover, the maximum oscillation amplitude is also increased by four times. The reason behind the change in the frequency response at lower pressures is the decrease in the viscous air damping. The effect of damping on the dynamic behavior of the torsional microscanners will be investigated extensively in the next chapter. Despite the change in the frequency and amount of deflections, all orders of resonances exhibit hysterical characteristics. The locations of these resonances are not random. They are located around $2f_r/n$, $n=1, 2, 3, \dots$. However, oscillation frequency of the device is always close to f_r , regardless of the order of the resonance. In the first resonance region, which is called the *primary* resonance, the oscillation frequency is half the excitation frequency. Thus oscillations in this resonance are called *subharmonic oscillations*. Within the second resonance range, oscillation frequency follows the excitation frequency, as it is in the simple harmonic oscillator case.

3.3.2 Square-wave Excitation

Figure 3.3-3 is the frequency response curve of the device for square wave excitation. Number of observable parametric resonances is more than the square-root excitation case. Figure 3.3-3 shows 8 parametric resonances at atmospheric pressure. However, monotonous decrease in the maximum oscillation amplitude as the order of resonances grows is also not present with square-wave excitation. This reveals that wider harmonic content of the square-wave signal gives rise to some other resonances. Hysteresis in the response curve is also

present for all 8 resonances, but the jump frequencies are different than the harmonic excitation case.

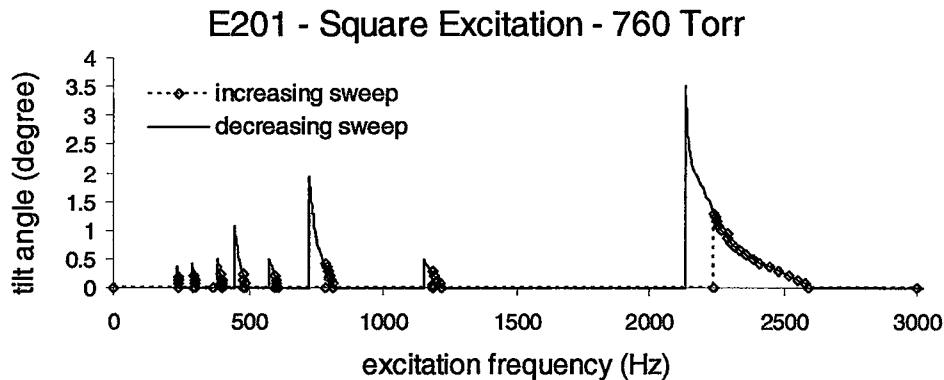


Figure 3.3-3: Experimental frequency response data at 760 Torr (1 Atm) and with 20 V_{p-p} square wave excitation. Number of observable parametric resonances is 8, due to the higher harmonics in the square wave excitation.

Although the amplitude of the excitation remained intact (20 V_{p-p}), maximum oscillation amplitude of the microscanner is higher when the system is driven by a square waveform. This is due to the higher amount of energy that is coupled to the oscillator.

In rooted-sinusoid excitation case, as the resonance order is increased, the maximum oscillation amplitude shrinks. However, this is not the case in square-wave excitation. Especially the third and fifth orders have very higher peak values compared to the second and fourth orders, respectively.

Alike the frequency domain characteristics, time domain behavior of the torsional microscanners also exhibits interesting and uncommon properties. In the next subsection, we present experimental and numerical data on time-domain behavior of the device.

3.4 Time Domain Characteristics

For time-domain characterization of the microscanners, a two-dimensional Position Sensing Device (PSD) based optical characterization setup was implemented. The details on the experimental setup are given in Appendix A.2.

3.4.1 Transient Response

Figure 3.4-1 and Figure 3.4-2 show the behavior of the output amplitude until the system reaches steady state. Excitation signal is a square-rooted sinusoid for both Figure 3.4-1 and

Figure 3.4-2, but the drive-frequencies are different. Figure 3.4-1 shows the transient response of the device, when it is driven with a frequency f greater than f_2 . Unlike linear systems, oscillation amplitude grows with in a positive exponential manner, until it reaches a maximum value. However, the oscillations do not settle immediately, but show a damped oscillatory behavior. If the drive frequency is very close to the boundary between the stable and unstable regions ($f \approx f_2$) damped oscillatory behavior in the output amplitude diminishes, and the device reaches steady-state immediately after the exponential growth.

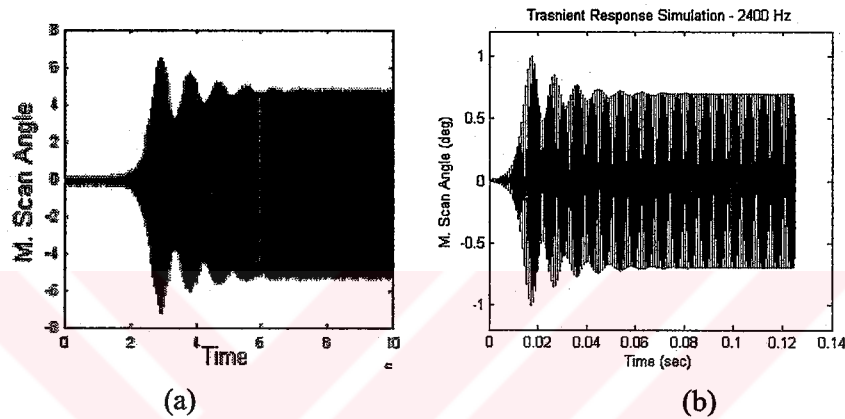


Figure 3.4-1: Transient response of the device, when $f_{\text{ext}} > f_2$ (stable region). (a) Experimental data (b) Simulation result.

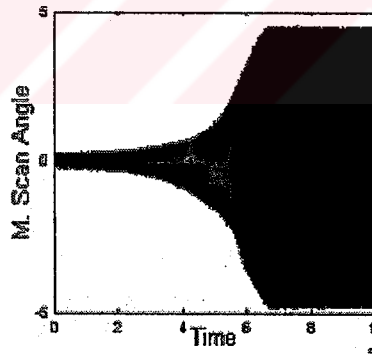


Figure 3.4-2: Experimental transient response of the device, when $f_{\text{ext}} \approx f_2$ (boundary of the stability curve).

3.4.2 Steady State Response

In steady-state, there is not a linear relationship between the drive signal and oscillation amplitude. The relation between the frequencies of drive and output depends on the order of resonance in which the device is operated. Oscillations in the 1st parametric resonance are called *subharmonic oscillations*, since the drive frequency is twice the oscillation frequency. For the 2nd order resonance, the device oscillations follow the drive signal frequency-wise. For

all other resonance orders, drive signal has a lower frequency than the actual oscillations. Figure 3.4-3 shows the input-output relations for the first two orders of resonances.

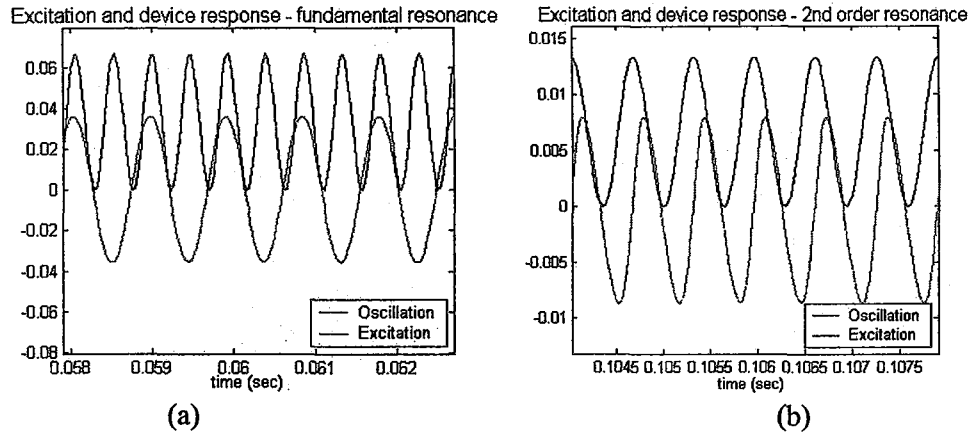


Figure 3.4-3: Excitation and device response (a) in the first order resonance; (b) in the second order resonance

When driven by a square waveform, the frequency relation between input and output for the first two orders of resonances is similar to those given in Figure 3.4-3. However, at higher order resonances, the response is not a pure sinusoid. Scan wave shows an unusual behavior and changes oscillation frequency and amplitude at each half cycle of the square wave. When excitation is in the OFF state (meaning that no torque is present in the system), the system makes free oscillation at its natural resonant frequency, when the excitation is in the ON state, the mirror oscillates at a higher frequency, which can be calculated using the excitation and natural frequencies. This phenomenon is called *alternating oscillation frequency*. In Figure 3.4-4 simulated waveforms for alternating frequency behavior can be seen together with the experimental data.

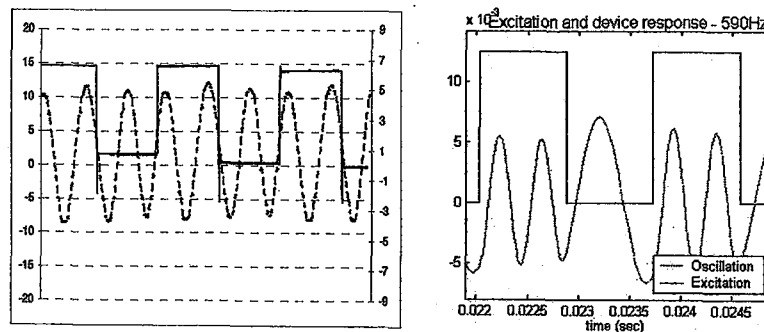


Figure 3.4-4: Alternating oscillation phenomenon at higher order resonances with 590Hz square wave excitation. (a) Experimental result; (b) Simulation results

3.5 Voltage Domain Characteristics

Voltage domain behavior refers to the response of the device to changes in the excitation amplitude. The dynamic mirror characterization setup that is used for frequency domain measurements can also be used for voltage domain characterizations of the microscanners.

Figure 3.5-1 is the plot that shows the relationship between the maximum mechanical deflection angle and the excitation amplitude. The deflection values are measured at the peak of the first order resonance of the microscanner. Regardless of the waveform of the excitation, maximum deflection angle grows linearly with the increasing excitation amplitude.

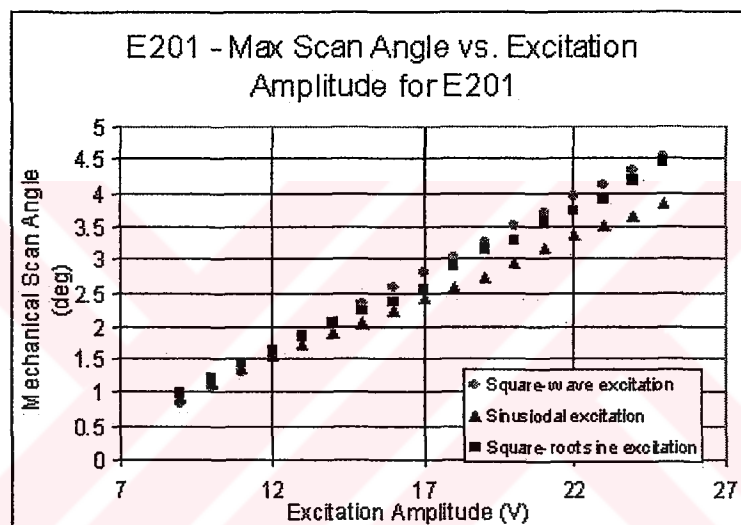


Figure 3.5-1: Maximum scan angle vs. excitation amplitude with square-wave, sinusoidal and square-root sine excitation. Experimental results belong to E201.

Similar experimental results on voltage domain behavior of IPMS microscanners are also given in some publications of Fraunhofer IPMS for microscanners of various size and shape. Figure 3.5-2 gives the experimental data on voltage domain behavior of different various round microscanners. Figure 3.5-2a shows how the frequency response of the device is changed with different excitation amplitudes. Figure 3.5-2b, on the other hand, compares voltage domain behavior of round microscanners with different comb finger orientations. All devices has a linear mechanical deflection—excitation amplitude characteristics, and validate the numerical and experimental results obtained in our laboratory.

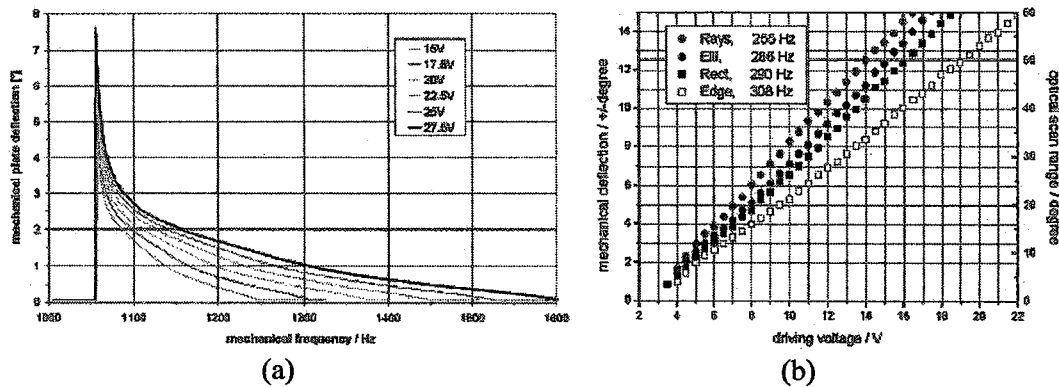


Figure 3.5-2: Voltage domain characteristics of IPMS scanners. (a) Effect of excitation voltage on frequency response. (b) Maximum scan angle vs. excitation amplitude characteristics of different IPMS scanners. Both results are taken from IPMS papers. [44]

3.6 Conclusions

Frequency response of a torsional comb-driven microscanner deviates significantly from linear system behavior. With rooted-sine excitation, up to five different orders of resonances were observed in vacuum measurements. When the devices excited with a square waveform, eight resonance orders were seen in atmospheric pressure. Each of those resonances show hysterical behavior, and abrupt changes in the output, when excitation frequency is swept downwards or upwards. All of the mentioned behaviors are typical for *parametric systems*, which have time varying coefficients in their equation of motion. As pointed out before, the equation of motion of a torsional microscanner has time varying coefficient, therefore the device is actually a parametric oscillator. In the next section, nature of parametric systems will be explored in detail.

Multiple parametric resonances and very sharp hysteresis jumps in the frequency response curves make this device a potential candidate for various applications. Due to higher order resonances, the device may be excited with frequencies far from the natural frequency. This is an important advantage, since this phenomenon can be exploited in some electrical applications to isolate electrical signals from input and output ports. A more promising aspect of the frequency response is the very abrupt jump in the output amplitude at some points. For instance, if such a system is biased at its resonance peak, a very slight change in the environmental conditions will lead to a collapse in the oscillations. This phenomenon is used for parametric amplification [50-51], mass sensor [52-53], impact detectors, etc.

Chapter 4

DYNAMIC BEHAVIOR: ANALYTICAL MODELING**4.1 Introduction**

Experimental and numerical investigation of dynamic behavior of torsional comb-driven microscanners in the Chapters 2 and 3 revealed the non-trivial dynamic nature of these devices. Multiple resonances, hysterical frequency response, subharmonic and superharmonic oscillations and frequency switching behavior of these devices set them apart from the simple 2nd order harmonic oscillators. A torsional comb-driven microscanner is a “*Parametrically Excited System*”. An analytical insight on this type of oscillators is given in this chapter.

A parametrically excited system is governed by a 2nd order differential equation, in which the time-dependent excitations appear as coefficients (parameters) of the equation. In simple harmonic systems, a small excitation cannot create a large response unless the excitation frequency is close to the resonance frequency of the system (primary resonance). However, a small parametric excitation can produce a large response when frequency of the excitation is close to twice the natural frequency (f_r) of the system (principal parametric resonance) [54]. Moreover, a parametric system may also produce relatively large response, if the excitation frequency is close to an integer fraction of twice the natural frequency. The resonance around $2f_r/n$ is called the n th order parametric resonance. The response to excitations of same amplitude shrinks as n grows. Generally, for macroscopic structures, only the principal parametric resonance is observable in the atmospheric pressure, due to high air damping. The first scientist to observe and report the parametric resonance phenomenon is Faraday. He reported that the surface waves in a fluid-filled cylinder under vertical excitation exhibited twice the period of the excitation itself. This phenomenon is now called *subharmonic oscillation*, and is a characteristic property of parametric systems. It was Strutt who provided a theoretical basis for understanding the observations of Faraday, Melde, etc. A detailed history on the improvements in the study of parametric systems and an extensive list of references on the subject is given in [54]. Today, parametric resonance phenomenon is frequently observed in different areas of science and engineering, such as photonic crystals [55], optical cavities [56], plate vibrations [57], and nano-scale devices [58].

In this chapter, a detailed analytical treatment of the parametric resonances in torsional comb-driven microscanners is presented. Since the mechanical mode of interest is only the torsional mode, and the modal separation and quality factor of the devices are sufficiently high, the system will be treated as a single-degree-of-freedom system. A global solution for the equation of motion valid at all damping and drive-schemes is impossible to achieve, hence, certain assumptions on damping and excitation are made at different analysis steps. In 4.2, the steady state behavior of torsional comb-driven microscanners is investigated without the effect of damping and cubic nonlinearities. 4.3 and 4.4 deal with the effects of damping and cubic nonlinearities on the steady-state behavior of the devices, respectively. Experimental and numerical verification of the results of the analytical treatments are presented when necessary.

4.2 Steady-State Behavior

In Chapter 2, the equation of motion for the torsional microscanner was given as,

$$I_m \frac{d^2 \theta}{dt^2} + b \frac{d\theta}{dt} + K_f \theta = M(t, \theta) \quad (4.1)$$

where, I_m is mass moment of inertia, b is the damping constant, K_f is the torsional stiffness, and $M(t, \theta)$ is the time and displacement dependant torque function. Damping term b is determined experimentally; the remaining parameters are calculated using analytical formulas or numerical simulations as given in Chapter 2. The torque induced by the comb actuators is given by,

$$M(t, \theta) = 2N \frac{1}{2} \frac{dC}{d\theta} V(t)^2 \quad (4.2)$$

where, N is the number of comb fingers, $dC/d\theta$ is the rate of change of capacitance with respect to the deflection angle, and $V(t)$ is the periodic drive signal. In order to be able to achieve a close form solution to 4.1, a set of assumptions need to be made. Figure 2.6-1 illustrates a plot of the $dC/d\theta$ term. For small deflections, this derivative function may be approximated by a third order polynomial. Since $dC/d\theta$ is an odd function, the fitting polynomial has only the linear and cubic terms. The torque is proportional to the square of the excitation; therefore, in order to obtain a harmonic excitation, the drive signal is chosen as a square-rooted sinusoid ($V(t) = A\sqrt{\cos(\omega t) + 1}$, where A is the excitation amplitude). The resulting simplified torque expression is given by,

$$M(t, \theta) = -(r_3 \theta^3 + r_1 \theta) A^2 (\cos(\omega t) + 1) \quad (4.3)$$

where, r_1 and r_3 are the coefficients of the first and third order terms of approximate $dC/d\theta$ expression, respectively. This simplified form of the torque reveals the reason behind the parametric characteristics of the device. Due to the multiplication of $dC/d\theta$ and the periodic excitation, terms with parametric coefficients arise in the equation of motion. Apart from the parametric effect, the torque also introduces a cubic nonlinearity into the system, which has a significant effect on the stability of the steady state solutions. In this subsection, the effect of this cubic nonlinearity and damping will be omitted, but the following two subsections will explore these two effects in detail. Substituting (4.3) into (4.1) and rewriting the equation with new parameters leads to a more comprehensive form of the equation of motion:

$$\frac{d^2\theta}{d\tau^2} + 2\alpha\frac{d\theta}{d\tau} + (\beta + 2\delta_1 \cos(2\tau))\theta + (\delta_3 + \delta_3 \cos(2\tau))\theta^3 = 0 \quad (4.4)$$

where the new parameters are defined as,

$$\tau = \frac{wt}{2}, \quad \alpha = \frac{b}{wI_m}, \quad \beta = 4\frac{(r_1A^2 + K_f)}{w^2I_m}, \quad \delta_1 = \frac{2r_1A^2}{w^2I_m}, \quad \delta_3 = \frac{4r_3A^2}{w^2I_m}$$

Neglecting the nonlinear term in (4.4) simplifies the analysis for the analytical treatment that follows; the effect of cubic nonlinearity will be discussed later

$$\frac{d^2\theta}{d\tau^2} + 2\alpha\frac{d\theta}{d\tau} + (\beta + 2\delta_1 \cos(2\tau))\theta = 0 \quad (4.5)$$

Introducing the change of variable $\phi(\tau) = \theta(\tau)\exp(\alpha\tau)$ into (4.5) simplifies the differential equation significantly. This transformation is proven in Appendix C, and yields to

$$\frac{d^2\phi}{d\tau^2} + p(\tau)\phi = 0 \quad (4.6)$$

where $p(\tau) = \xi + 2\delta_1 \cos(2\tau)$, and $\xi = (\beta - \alpha^2)$. This linear and homogeneous differential equation is first studied by Mathieu [53] in connection with the problem of vibrations of an elliptic membrane, and is called *Mathieu's equation*. There is couple of different methods of determining the steady-state solutions of the Mathieu Equation. The analysis in this work will follow the Floquet Theory analysis of (4.6) in [54].

Equation (4.6) is a linear, second-order homogeneous differential equation; therefore there exist two linearly independent solutions $u_1(t)$ and $u_2(t)$, and all other solutions $u(t)$ may be written as a linear combination of $u_i(t)$. Mathematically,

$$u(\tau) = c_1u_1(\tau) + c_2u_2(\tau) \quad (4.7)$$

where, c_1, c_2 are arbitrary constants. Since the coefficients of (4.5) are periodic with π , we can write that;

$$\ddot{u}(\tau + \pi) + p(\tau)u(\tau + \pi) = 0 \quad (4.8)$$

It follows from (4.8) that if $u_i(t)$ is a fundamental set of solutions for (4.6), so are $u_i(t + \pi)$, since they satisfy the same equation. Therefore

$$\begin{aligned} u_1(\tau + \pi) &= a_{11}u_1(\tau) + a_{12}u_2(\tau) \\ u_2(\tau + \pi) &= a_{21}u_1(\tau) + a_{22}u_2(\tau) \end{aligned} \Rightarrow \begin{bmatrix} u_1(\tau + \pi) \\ u_2(\tau + \pi) \end{bmatrix} = [A] \begin{bmatrix} u_1(\tau) \\ u_2(\tau) \end{bmatrix}, \quad [A] = \begin{bmatrix} a_{11} & a_{12} \\ a_{21} & a_{22} \end{bmatrix} \quad (4.9)$$

Relation 4.9 in hand, we have to prove the existence of the fundamental set of solutions of following property:

$$\begin{aligned} v_1(\tau + \pi) &= \lambda_1 v_1(\tau) \\ v_2(\tau + \pi) &= \lambda_2 v_2(\tau) \end{aligned} \quad (4.10)$$

To prove this, it should be noted that any other fundamental set of solutions $v_i(t)$ is related to the fundamental set of solutions $u_i(t)$ through a nonsingular 2×2 matrix $[P]$, such as

$$\begin{bmatrix} v_1(\tau) \\ v_2(\tau) \end{bmatrix} = [P] \begin{bmatrix} u_1(\tau) \\ u_2(\tau) \end{bmatrix} \quad (4.11)$$

Since $[P]$ is nonsingular, we can written that

$$\bar{v}(\tau) = [P]^{-1} \bar{u}(\tau) \quad (4.12)$$

Thus, we can write that

$$\bar{v}(\tau + \pi) = [P]^{-1} \bar{u}(\tau + \pi) \quad (4.13)$$

Substituting (4.9) into (4.13) yields

$$\bar{v}(\tau + \pi) = [P]^{-1} [A] \bar{u}(\tau) \quad (4.14)$$

Substitution of (4.11) into (4.14) lead to

$$\begin{bmatrix} v_1(\tau + \pi) \\ v_2(\tau + \pi) \end{bmatrix} = [B] \begin{bmatrix} v_1(\tau) \\ v_2(\tau) \end{bmatrix}, \quad [B] = [P]^{-1} [A] [P] \quad (4.15)$$

Since the $[P]$ is an arbitrary matrix, it can be chosen such that $[B]$ has the *Jordan canonical form*. In such a case $[B]$ will have the eigenvalues of $[A]$ on its diagonal. Let's say the eigenvalues of $[A]$ are $\lambda_i, i=1,2$. Then we can write following relation

$$\begin{bmatrix} v_1(\tau + \pi) \\ v_2(\tau + \pi) \end{bmatrix} = \begin{bmatrix} \lambda_1 & 0 \\ 0 & \lambda_2 \end{bmatrix} \begin{bmatrix} v_1(\tau) \\ v_2(\tau) \end{bmatrix} \quad (4.16)$$

which is essentially (4.10) written in matrix form. It follows from (4.10) that

$$v_i(\tau + n\pi) = \lambda_i^n v_i(\tau) \quad (4.17)$$

where n is an integer. Consequently as $t \rightarrow \infty$,

$$v_i(\tau) \rightarrow \begin{cases} 0 & \text{if } |\lambda_i| < 1 \\ \infty & \text{if } |\lambda_i| > 1 \end{cases}$$

It can be seen from (4.17) that, when $\lambda_i = 1$, v_i is π periodic, and, when $\lambda_i = -1$, v_i is periodic with the period 2π .

Multiplying both sides of (4.17) with $\exp[-\gamma_i(t+\pi)]$ for $n=1$ leads to

$$\exp[-\gamma_i(\tau + \pi)]v_i(\tau + \pi) = \lambda_i \exp(-\gamma_i\pi) \exp(-\gamma_i\tau)v_i(\tau) \quad (4.18)$$

If γ_i is chosen, such that $\lambda_i = \exp(\gamma_i\pi)$, we have

$$\exp[-\gamma_i(\tau + \pi)]v_i(\tau + \pi) = \exp(-\gamma_i\tau)v_i(\tau) \quad (4.19)$$

It follows from (4.19) that $\phi_i(t) = \exp(-\gamma_i t)v_i(t)$ is a π periodic function. Therefore, the fundamental set of solutions $v_i(t)$ can be written in the following form:

$$\begin{aligned} v_1(\tau) &= \exp(\gamma_1\tau)\phi_1(\tau) \\ v_2(\tau) &= \exp(\gamma_2\tau)\phi_2(\tau) \end{aligned} \quad (4.20)$$

If the matrix $[A]$ of (4.12) has repeated eigenvalues ($\lambda_1 = \lambda_2$), the matrix $[B]$ is either

$$[B] = \begin{bmatrix} \lambda & 0 \\ 0 & \lambda \end{bmatrix} \quad (4.21)$$

or

$$[B] = \begin{bmatrix} \lambda & 0 \\ 1 & \lambda \end{bmatrix} \quad (4.22)$$

The fundamental set of solutions corresponding to (4.21) is exactly the same as (4.20). However, for (4.22) the fundamental solution set is slightly different [54].

$$\begin{aligned} v_1(\tau) &= \exp(\gamma\tau)\phi_1(\tau) \\ v_2(\tau) &= \exp(\gamma\tau) \left[\phi_2(\tau) + \frac{\tau}{\lambda\pi} \phi_1(\tau) \right] \end{aligned} \quad (4.23)$$

Equations (4.20) and (4.21) show that the stability of the solution depends on the sign of the real parts of γ_i ; therefore, they are called the *characteristic exponents* of the system. They are given by:

$$\gamma_i = \frac{1}{T} \ln(\lambda_i) \quad (4.24)$$

The characteristic exponents of (4.6) is determined as follows: Let us choose $u_1(t)$ and $u_2(t)$ to be the fundamental set of solutions satisfying the initial conditions

$$\begin{aligned} u_1(0) &= 1, \quad \dot{u}_1(0) = 0 \\ u_2(0) &= 0, \quad \dot{u}_2(0) = 1 \end{aligned} \quad (4.25)$$

The entries of the matrix $[A]$ can be determined by using (4.9) and the derivative of it together with (4.17). The values of these parameters are found as

$$\begin{aligned} a_{11} &= u_1(\pi), \quad a_{12} = \dot{u}_1(\pi) \\ a_{21} &= \dot{u}_2(\pi), \quad a_{22} = u_2(\pi) \end{aligned} \quad (4.26)$$

It is previously stated that λ_i are the eigenvalues of $[A]$. This follows from the linear algebra that

$$\lambda^2 - 2\sigma\lambda + \Delta = 0 \quad (4.27)$$

where

$$\sigma = \frac{1}{2} [u_1(t) + \dot{u}_2(t)] \quad \Delta = u_1(\pi)\dot{u}_2(\pi) - \dot{u}_1(\pi)u_2(\pi) \quad (4.28)$$

The parameter Δ is called the *Wronskian determinant* and it is equal to unity for Mathieu Equation [59]. Therefore, for a Mathieu equation, eigenvalues of the matrix $[A]$ are given by

$$\lambda_{1,2} = \xi \pm \sqrt{\xi^2 - 1}, \quad \lambda_1\lambda_2 = 1 \quad (4.29)$$

In order to obtain the entries of the matrix $[A]$ in (4.26), two linear independent solutions of (4.6) should be numerically integrated during the first period of oscillation and values and first derivatives of these solutions should be determined at the end of one period. When the eigenvalues of $[A]$ are found through (4.27), the characteristic exponents may be determined by using the relation 4.20. The stability of the steady-state solutions of 4.6 can be examined through 4.29. If $|\zeta| > 1$, the system is in the unstable regime and the solution amplitude grows unboundedly (in real-time systems, the unstable solutions is limited by the nonlinearities in the system, which will be examined in the following subsections). In order to obtain a stable solution, absolute value of ζ should be less than unity. The ζ - δ values that correspond to $|\zeta| = 1$ determine the boundaries between the stable and unstable regions, and the solutions are π or 2π periodic. Distribution of these boundaries can be determined by numerically evaluating the ζ - δ values that correspond to $|\lambda| = 1$. This is a rather complicated process and there exist numerous analytical approximations to determine the boundaries separating stability from instability. Next subsection deals with the problem of determination of stability curves.

4.3 Stability Curves

There exist several methods of stability analysis for the Mathieu Equation. Some of these methods are the method of multiple scales [60], Hill's infinite determinant [61], and the method of strained parameters [54]. The latter method uses the results of steady-state analysis by Floquet Theory, and provides more accurate results for the solution at the boundaries of the stability curves. Following analysis will be based on this method.

According to the Floquet theory, the solutions of (4.6) on the stability transition curves have periods of π or 2π , and these curves correspond to the positive or negative unity eigenvectors of the characteristic matrix. These stability curves form a tongue-like shape in the drive-voltage – drive-frequency space, and therefore called “stability tongues”. Due to the time scaling of (4.4), a solution which is of period π in the new time scale corresponds to an oscillation of period T in the actual time. Similarly, the 2π periodic solution of (4.6) is actually an oscillation of period $2T$. This $2T$ periodic solution is half the frequency of the drive signal and corresponds to the subharmonic oscillation in the 1st order parametric resonance. Based on the result of Floquet theory that on boundaries of the stability tongues the solution of (4.6) is either π or 2π periodic, we utilized the method of strained parameters, in order to find analytical expressions for determining these tongues. In this method the characteristic exponents are chosen so that the periods of the possible solutions of (4.6) are π or 2π . Then, the required parameters are determined in such a way that this assumption holds. The method of strained parameters uses the following perturbation expansions, in order to obtain the stability transition curves in the form $\xi = \xi(\delta_1)$:

$$u(\tau) = u_0(\tau) + \delta_1 u_1(\tau) + \delta_1^2 u_2(\tau) + \dots \quad (4.30)$$

$$\xi = \xi_0 + \delta_1 \xi_1 + \delta_1^2 \xi_2 + \dots \quad (4.31)$$

Substituting (4.30) and (4.31) into (4.6) and equating the coefficients of same powers δ gives

$$\ddot{u}_0 + \xi_0 u_0 = 0 \quad (4.32)$$

$$\ddot{u}_1 + \xi_0 u_1 = -\xi_1 u_0 - 2\xi_0 \cos(2\tau) \quad (4.33)$$

$$\ddot{u}_2 + \xi_0 u_2 = -\xi_2 u_0 - \xi_1 u_1 - 2u_1 \cos(2\tau) \quad (4.34)$$

π and 2π periodic solutions of (4.32) are given by

$$u_0 = a \cos 2n\tau + b \sin 2n\tau, \quad n = 0, 1, 2, \dots \quad (4.35)$$

$$u_0 = a \cos(2n-1)\tau + b \sin(2n-1)\tau, \quad n = 1, 2, 3, \dots \quad (4.36)$$

Equation (4.32) also implies that ζ_0 can only be equal to n^2 . Each specific n value corresponds to a different stability tongue. The boundaries of these tongues can be determined by substituting (4.35) and (4.36) into (4.32), (4.33) and (4.34) and solving these system of equations iteratively. Here, this solution process is applied only for the first stability tongue that corresponds to $\zeta_0=1$. Higher order tongue equations can be determined using the same procedure.

When $\zeta_0=1$, (4.32) becomes

$$u_0 = a \cos \tau + b \sin \tau \quad (4.37)$$

Substituting this expression into (4.33) yields

$$\ddot{u}_1 + u_1 = -a(\xi_1 + 1) \cos \tau - b(\xi_1 - 1) \sin \tau - a \cos 3\tau - b \sin 3\tau \quad (4.38)$$

In order that u_1 to be periodic, coefficients of 2π periodic terms in (4.38) must vanish. This leads to

$$a(\xi_1 + 1) = 0 \quad (4.39)$$

$$b(\xi_1 - 1) = 0 \quad (4.40)$$

There are two nontrivial solutions satisfying both (4.39) and (4.40). When $\zeta_1 = -1$ and $b=0$, the particular solution of (4.33) is

$$u_1 = \frac{1}{8} a \cos 3t \quad (4.41)$$

Substitution into (4.34) gives

$$\ddot{u}_2 + u_2 = -a\left(\beta_2 + \frac{1}{8}\right) \cos \tau + \frac{1}{8} a \cos 3\tau - \frac{1}{8} a \cos 5\tau \quad (4.42)$$

Again, the periodicity of the solution requires 2π periodic terms to diminish. Hence

$$\xi_2 = -\frac{1}{8} \quad (4.43)$$

Therefore, the first transition curve of the first stability tongue is given by

$$\beta = 1 - \delta_1 - \frac{1}{8} \delta_1^2 + \alpha^2 + O(\delta^3) \quad (4.44)$$

When same procedure is used for the other nontrivial solution of (4.39) and (4.40), which corresponds to $\beta_1 = 1$ and $a=0$, the other transition curve is obtained as

$$\beta = 1 + \delta_1 + \frac{1}{8} \delta_1^2 + \alpha^2 + O(\delta^3) \quad (4.45)$$

Equations (4.44) and (4.45) forms the boundaries for the first stability tongue, when there is no damping in the system. For the second stability tongue, boundary equations are given by

$$\beta = 4 + \frac{5}{12}\delta^2 + \alpha^2 + O(\delta^3) \quad (4.46)$$

$$\beta = 4 - \frac{5}{12}\delta^2 + \alpha^2 + O(\delta^3) \quad (4.47)$$

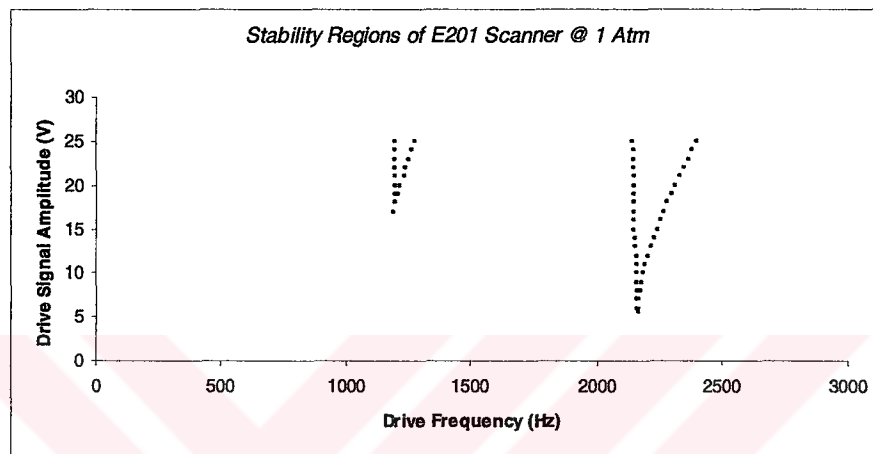


Figure 4.3-1: Stability tongues for E201 at atmospheric pressure. Up to 25V only two parametric resonances were observable, due to high damping

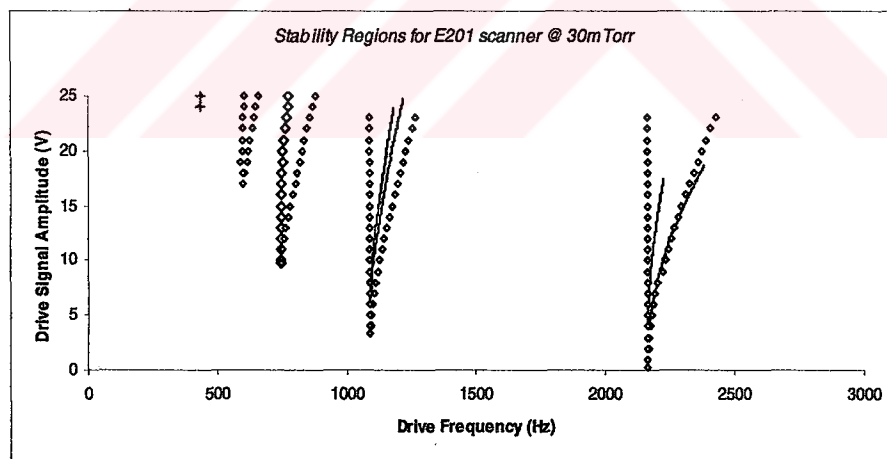


Figure 4.3-2: Stability tongues for E201 at 30 mTorr, and analytical approximations. Due to much lower damping, 5 parametric resonances could be observed.

Figure 4.3-1 shows the stability tongues of the microscanner in the atmospheric pressure. There is a significant viscous air damping between the comb fingers in the atmospheric pressure (we have measured a Q factor of 22), so that there are only two observable parametric resonances within the operation voltage of the device. Additional orders or resonances would

be observed with higher drive voltages, but we avoided such high voltages in order to prevent device failure. The stability tongues of the microscanner in 30 mTorr ambient pressure can be seen in Figure 4.3-2. Voltage and frequency span of the two plots are identical. In low pressure, air damping is much less and therefore the device has a much higher quality factor (~ 1250). As seen in the Figure 4.3-2 there are 5 observable parametric resonances and the width of the stability tongues are increased, and their tips came much closer to the $V=0$ axis. In Figure 4.3-2, solid lines represent the results of the analytical expressions of the stability tongues. The analytical results are in good agreement with the experimental data. However, as the input voltage increases, the deviation of the analytical approximation from the experiments increases. This is due to the fact that for higher voltages, the small driving signal and small tilt angle approximations are becoming invalid and therefore our perturbation analysis ceases to be accurate. Another reason of the difference between the experimental and analytical results is the cubic nonlinearity in (4.3). As the driving voltage increases, this cubic nonlinearity term also grows and it prevents the left hand of the stability curve to bend rightward.

4.4 Effect of Cubic Nonlinearity

Floquet analysis showed that within the unstable region, oscillation amplitude of the device should grow unboundedly, even if damping is present. However, real devices do not have such behavior. This difference is due to the effect of the nonlinearity term neglected before. The effects of nonlinearity can be explained as follows: as the resonance causes the amplitude of the motion to increase, the relation between period and amplitude (which is a characteristic effect of nonlinearity) causes the resonance to detune, decreasing its tendency to produce large motions.

4.5 Conclusions

An analytical model for a torsional comb-driven microscanner is presented. The model gives a small-signal solution for the nonlinear system around the single DC operating point, which is the rest position. Stability analysis based on the analytical model successfully predicted the locations and characteristics of the stability tongues, especially for small excitation amplitudes, which ensures that small signal assumption holds.

Chapter 5

CONCLUSIONS

In this research, comb-driven torsional microscanners are studied. First a numerical and an analytical model are developed, then the results are successfully verified in the laboratory using a number of experimental setups we developed for scanner characterization.

Torsional microscanners studied in this research show interesting hysteretic frequency behavior, parametric resonances and subharmonic oscillations, alternating frequency behavior for square wave excitation, and nonlinear transient response. The numerical model gives a powerful tool to predict the nonlinear device response to any kind of excitation. The analytical model is based on Floquet Theory and analytical stability curve predictions follow method of strained parameters. The analytical solution is only possible when damping effects are ignored and small deflections are assumed. The expressions obtained for dynamic behavior and stability behavior of the device gives a good understanding of the mathematical meaning of different device properties, such as damping, natural frequency, actuation force (torque), etc. Numerical simulation and analytical treatment results were compared with experimental results for model verification. This comparison showed that both models successfully predict frequency response and stability regions of the scanners.

A number of experimental setups are developed and implemented during this research. The setups facilitate accurate and automatic characterization of microscanners. All measurement techniques used in this research employ optical methods, and they enable accurate characterization of transient and steady-state response to various excitations, amplitude of the hysteretic frequency response, stability characteristics, mode frequencies and dynamic deformation, and damping mechanism of comb driven microscanners.

As a future work, numerical tools developed can be used to improve the scanner control algorithms. Another configuration to be analyzed is the microscanners that employ different comb-finger electrode configurations for beam pointing such as those used for telecom applications.

Appendix A

EXPERIMENTAL SETUPS

Dynamic characterization of microscanner devices is concerned with the measurement of device response to driving signals of different amplitude, frequency, waveform, etc. The response to be measured is the mechanical deflection angle, and it can be monitored in different ways for different devices. Some microscanner devices employ some built-in feedback mechanisms in order to enable real-time monitoring of device motion (such as piezoresistive or capacitive feedback loops that were mentioned in Chapter I). IPMS scanners do not have such a feedback capability. Optical characterization is a powerful way to measure dynamic responses of such microscanners without a position feedback utility. We have implemented several optical microscanner characterization setups in our laboratory.

A.1 Dynamic Microscanner Characterization Setup (DMCS)

A.1.1 Layout and Operation

Figure A.1-1 is the sketch of the dynamic microscanner test setup that was used in the stability and frequency response measurements presented in this thesis work. Details on how each of those measurement were done also given below.

The fundamental measurement device is a single photodetector, which is placed very close to the center of the scan line. During device operation, output of the detector is a periodic train of non-uniformly spaced impulses. This impulse train is used to form a square wave, whose duty cycle and frequency gives direct information on the oscillation frequency and amplitude of the microscanner. Figure A.1-2 shows the diagram of the simple circuit to form the desired square waveform from the impulses of the photodetector. The circuit is composed of three stages: an inverting amplifier to amplify the detector output, an inverter and a D-type positive-edge-triggered flip flop. The gain of the inverting amplifier in the first stage can be adjusted via the variable resistor. Even if the amplifier output signal level is not TTL compatible, regenerative property of the inverter solves this problem. The inverter also maintains signal integrity. A

proper zener ensures that the voltage level of the inverter input does not exceed a certain level. Output of the inverter is fed into the clock input of the flip-flop. Complementary output of the flip-flop is fed back to its input; therefore at every impulse from the photodetector flip-flop output switches state and forms the desired square waveform. This signal is then captured by a data acquisition card and transferred into LABView, where it is processed.

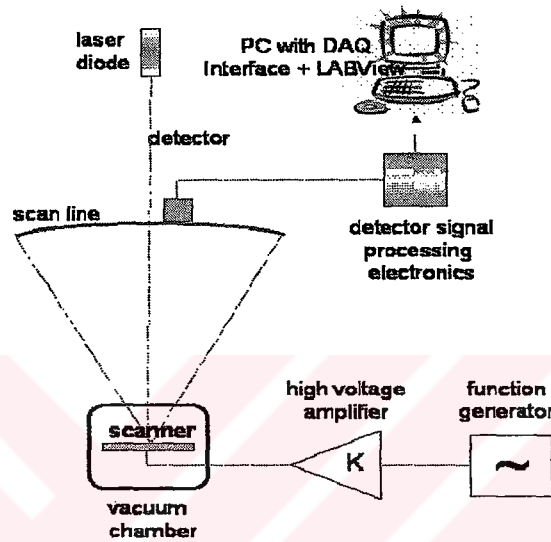


Figure A.1-1: Sketch of the dynamic micromirror characterization setup

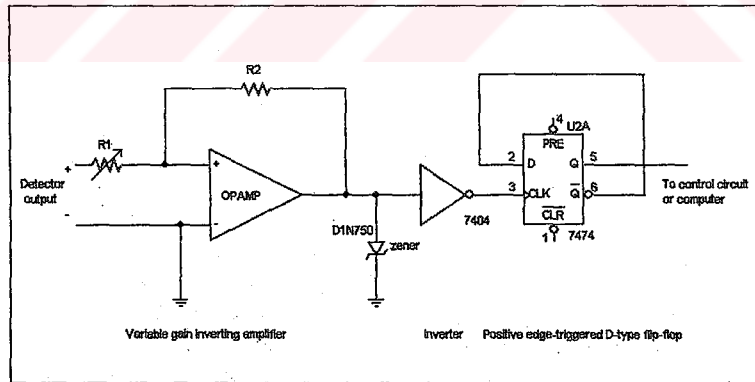


Figure A.1-2: Schematic of the electronic circuitry in Figure A.1-1

A series of simple evaluations in LABView is sufficient to extract the valuable information in the above mentioned square waveform. In order to be able to make precise measurements, the angle in which the detector placed (θ_0) should be known exactly. Oscillation frequency (therefore the period) is exactly the frequency of the square wave from the flip-flop. From this

point on, derivation of the scan angle is very simple, and is given below. Timing convention used in the derivation is shown in Figure A.1-3.

$$t_0 = |dc - 0.5| * T$$

$$\frac{\theta_0}{\theta_{max}} = \frac{\sin\left(\frac{2\pi}{T}t_0\right)}{\sin\left(\frac{2\pi}{T}\frac{T}{4}\right)} = \frac{\sin\left(\frac{2\pi}{T}t_0\right)}{\sin\left(\frac{\pi}{2}\right)} = \sin\left(\frac{2\pi}{T}t_0\right)$$

$$\Rightarrow \theta_{max} = \frac{\theta_0}{\sin\left(\frac{2\pi}{T}t_0\right)}$$

where dc is the duty cycle and T is the period of the square waveform. However, θ_{max} is the optical scan angle and it should be halved in order to get the mechanical scan angle.

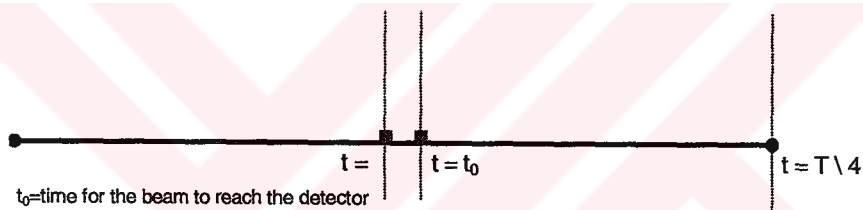
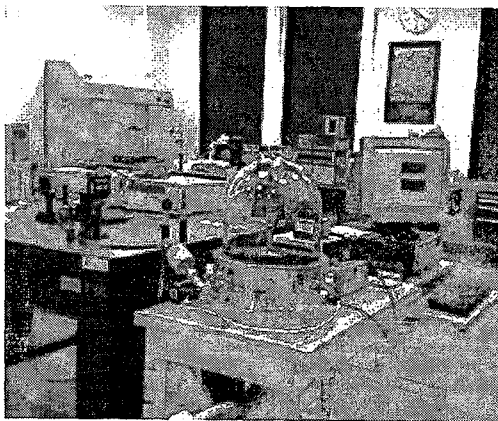
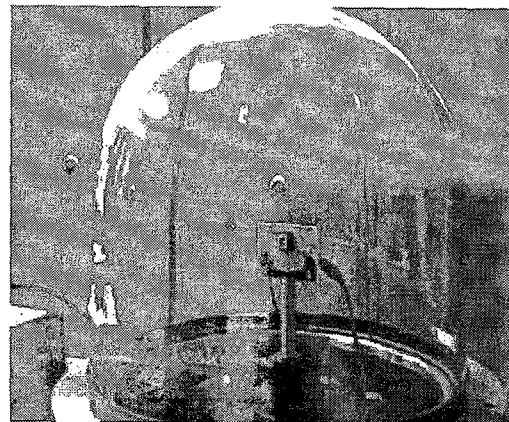


Figure A.1-3: Timing convention used in the scan angle derivation

Following two figures give the photographs of the setup and a screenshot of the LABView program written for this measurement setup.



(a)



(b)

Figure A.1-4: Photos of the experimental setup

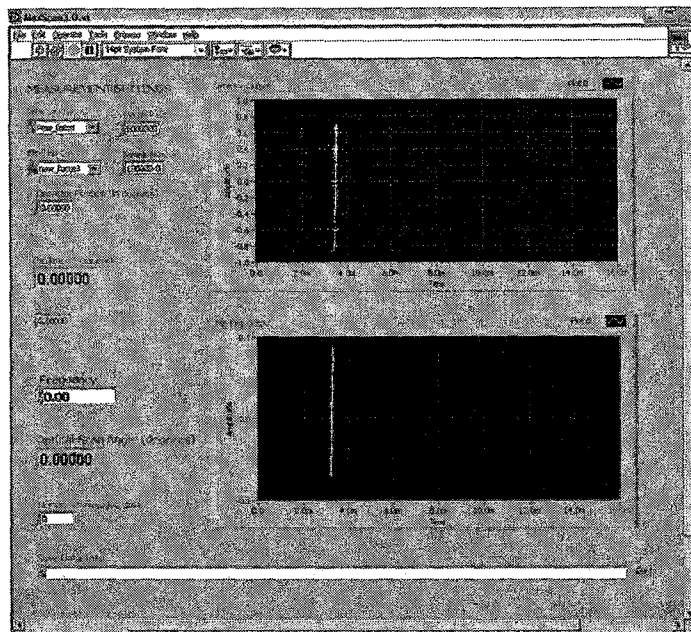


Figure A.1-5: LABView control program for the DMCS

A.1.2 Frequency Response Measurements

Frequency response characterization is done by sweeping the frequency of the driving signal upwards or downwards with constant amplitude and recording the deflection angle. Currently the frequency adjustments are done manually. With a suitable GPIB interface, the signal generator in the setup can properly be controlled and synchronized through the computer and full automatic data acquisition can be possible.

A.1.3 Stability Measurements

Stability analysis requires to do measurements in the drive-voltage—drive-frequency plane. In other words, both drive voltage and frequency should be adjusted and oscillation amplitude should be recorded. Stability measurements in this thesis were done by scanning the frequency axis at constant drive-voltage levels.

A.1.4 Voltage Domain Measurements

This type of characterization is done to figure out the maximum deflection angle at certain drive signal amplitude. This measurement requires manual intervention, since the maximum deflection frequency shifts as the driving signal amplitude is changed.

A.1.5 Damping Measurements

A slight modification in DMCS leads to a simple yet precise quality factor measurement for microscanners. This measurement technique exploits the fact that oscillation amplitude of a free oscillating 2nd order systems shrinks to $1/e$ of the initial amplitude after Q cycles of oscillations, due to damping. The photodetector in Figure A.1-1 is placed exactly at $1/e$ of the scan line. After the drive signal is turned off, the oscillation amplitude starts to shorten and amplitude of the detector peaks grows, due to the longer integration time on the detector. As the length of the scan line becomes smaller than $1/e$ of the initial amplitude, no more peaks are observed in the detector output. Figure A.1-6 shows an example recorded detector output during this sequence.

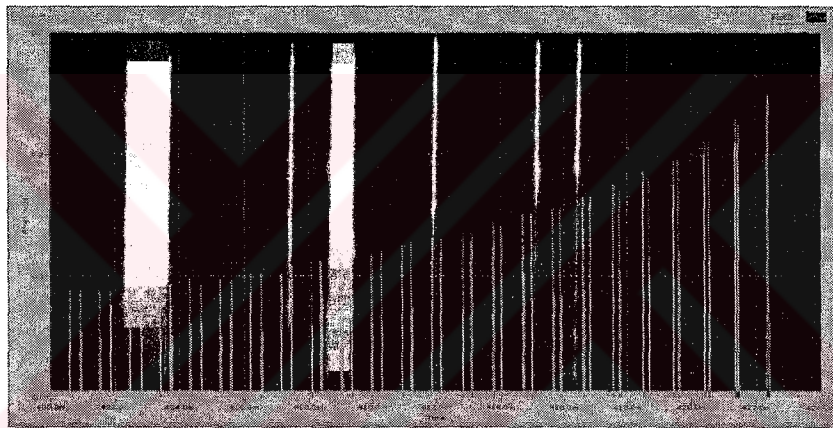


Figure A.1-6: Sample quality factor measurement data taken with DMCS

Number of the detector peaks in the interval between the point where peak amplitudes begin to grow and the peaks disappear gives the quality factor of the device. Quality factor for the scanner in Figure A.1-6 is 21. Since the count is always an integer, a certain error is introduced in this measurement technique. For instance, maximum error of 5% is possible if Q factor is 20. This accuracy is enough for many applications. A more precise damping measurement technique is presented in Appendix B.

A.2 Transient Response Measurement Setup (TRMS)

A.2.1 Layout and Operation

Transient response of a microscanner device until it reaches steady-state when it is excited by a certain signal is an important merit to characterize the device behavior. This type of

measurements require the recording the motion of the device for the entire time interval of interest. This is not possible with the setup introduced in Appendix A. Another optical characterization setup was built to accomplish transient response measurements. This setup was also used for damping (Q factor) measurements of microscanners. Figure A.2-1 is a sketch of the aforementioned setup.

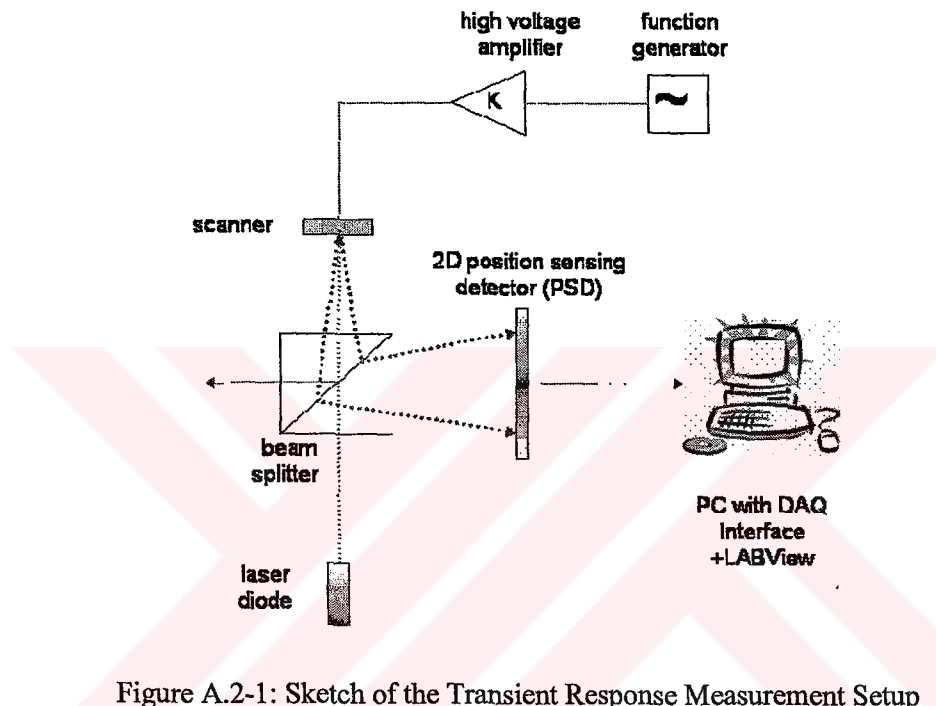


Figure A.2-1: Sketch of the Transient Response Measurement Setup

The heart of the setup is a custom-made, high-speed 2D position sensing device (PSD). A PSD is a device that enables us to determine the exact position of a laser beam on its active area. Our PSD has an active area of $1 \times 1 \text{ in}^2$, and four output pins for real time differential position monitoring in $-x$ and $-y$ axis. It is with a driving circuit that converts current output of the pins into voltage and computes the exact position from the outputs. Laser beam from the diode and scan line from the moving microscanner pass through a beam splitter and shined on the microscanner and PSD, respectively. PSD output is fed into the driving circuit and the position information from the circuit is recorded via a DAQ card and LABVIEW. Maximum measurable scan amplitude was limited by the size of the active area of PSD. In our setup, this maximum value was $\sim 1^\circ$ mechanical. Some optical modifications in the setup would lead to higher maximum measurable scan angles; however current values were sufficiently large for

measurements of interest. Figure A.2-2 shows an exemplary transient response measurement for a comb-driven torsional microscanner. The plot shows the device initially at rest. The input is turned on after 1.6 seconds and the device reaches steady state after 7th second. The transient behavior is successfully modeled.

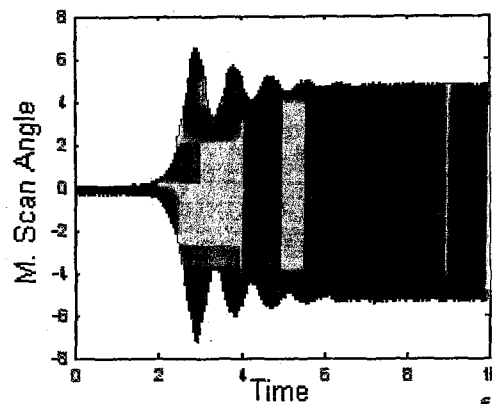


Figure A.2-2: Sample transient response measurement data

A.2.2 Damping Measurements

A simple technique to measure the quality factor of a microscanner is given in Appendix **Error! Reference source not found.** Although it is simple and fast, sensitivity of the measurements may not be sufficient for in some cases where high accuracy is required. A more formal and precise damping measurement may be accomplished by using TRMS. In this technique, die-out oscillations of a microscanner are recorded using the PSD and a proper function describing the die-out oscillatory behavior (exponential decay of a sinusoid) is fitted to the acquired data using the curve fitting toolbox of MATLAB.

A.3 Out-of-plane Mode Frequencies Measurement Setup

Laser Doppler Vibrometry is an effective way to measure the velocity and displacement of a microstructure oscillating in an out-of plane mode. We have utilized a Polytec PDV100 portable laser Doppler vibrometer to characterize the modal characteristics of various microscanners. PDV100 was capable of measuring velocities between 2 $\mu\text{m}/\text{sec}$ and 500 mm/sec . Maximum measurable frequency was 20 KHZ. This was a limiting factor, since higher mode natural frequencies of most of the available scanners were higher than this limit. Figure A.3-1 shows the measurement setup, which is capable of measuring all types of out-of-plane vibrations of a microscanner.

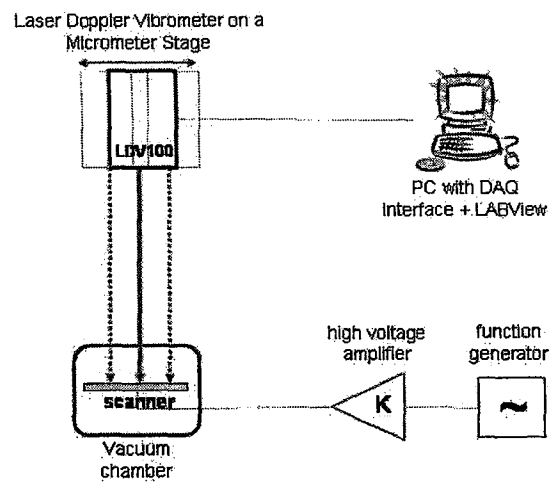


Figure A.3-1: Sketch of the LDV measurement setup.

Laser Doppler Vibrometry is a single point measurement technique; therefore a certain out-of-plane vibration can be completely characterized by comparing the amount of displacement and phase of the vibrations on different points on the mirror. For instance, in out-of-plane translational mode, all points on the mirror surface vibrate identically, however, in out-of-plane torsional mode; points on the rotation axis have zero velocity, whereas points on the mirror edge vibrate with maximum velocity. Figure A.3-2 shows the nine measurement points on the scanner mirror for mode characterization.

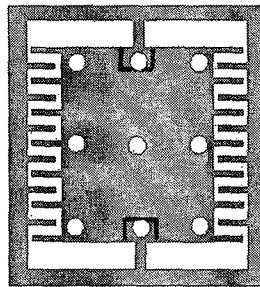


Figure A.3-2: LDV measurement points for out-of-plane mode characterization.

The vibrometer of our setup was only capable of measuring the velocity of the vibrating body, therefore a simple LABView interface was written to convert the velocity information into displacement data. Details of this conversion are given below.

$$x(t) = a \cos(\omega t)$$

$$v(t) = \dot{x}(t) = a\omega \sin(\omega t)$$

$$\Rightarrow |x(t)| = \frac{|v(t)|}{\omega}$$

where, $x(t)$ is the displacement, $v(t)$ is the velocity data grabbed by the vibrometer, and a is the oscillation amplitude. This derivation assumes that the vibration of interest a pure sinusoid, which is generally the case. A screenshot of the LABView program that implements the above derivation and displays the results is given in Figure A.3-3.

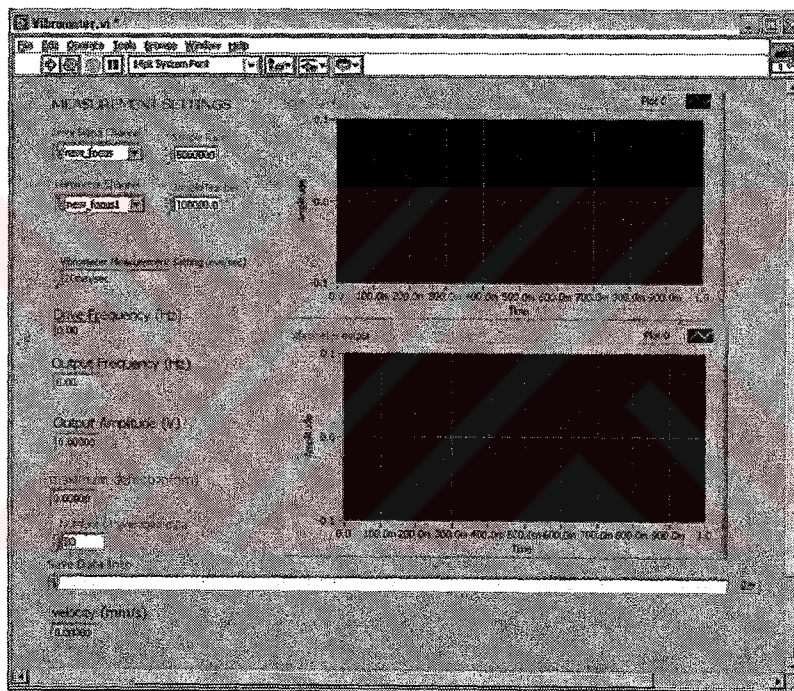


Figure A.3-3: LABVIEW Control program screenshot

Appendix B

MODE FREQUENCY FORMULAS FOR MICROSCANNERS

Basic one-axis torsional scanner geometry and the first five fundamental vibration modes are illustrated in Figure B.1.

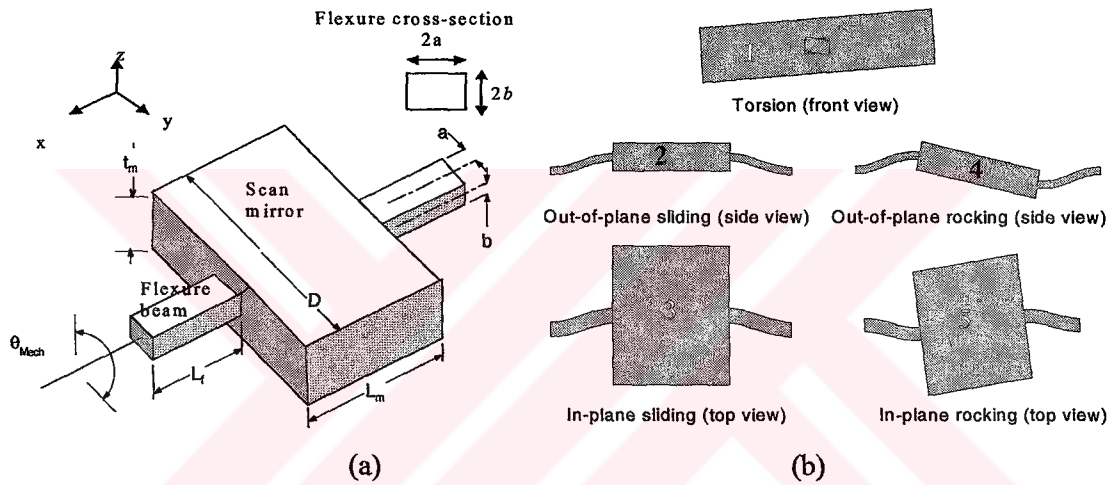


Figure B.1 (a) Torsional resonant scan mirror suspended with two flexure beams that are fixed at the ends, figure inset shows flexure rectangular cross-section and coordinate axis; (b) five fundamental vibration modes for the torsional scanner, which are rotation around x -axis (torsional), translation in z -axis (out-of-plane translation), translation in y -axis (in-plane sliding), rotation around y -axis (out-of-plane rocking), and rotation around z -axis (in-plane rocking).

One can calculate the natural frequencies of each vibration mode by using appropriate displacement or rotation angle variable, spring constant, and effective mass or effective mass moment of inertia terms. As an example, the natural frequency for the vibration mode along y -axis (in-plane sliding) with angular frequency ($\omega=2\pi f$) can be calculated by:

$$\frac{d^2 y}{dt^2} + \omega^2 y = 0 \quad (1)$$

$$\omega = 2\pi f = \sqrt{K_s / M_{eff}} \quad (2)$$

where K_s is the spring constant for the mode and M_{eff} is the effective mass of the scan mirror for the particular vibration mode. Throughout our analysis, the mirror plate is assumed rigid and flexures are assumed fixed on either end. In addition, damping is ignored in (B.1) because of the typically negligible effect on the natural frequency for underdamped systems.

Table B-1 summarizes the spring constant, effective inertia including the flexure-inertia terms for 5 fundamental modes. The formulas for the spring constants are consistent with values given elsewhere in the literature. Table B-2 gives mirror inertia for different mirror shapes. The natural frequency of a mode can be calculated using (B.2).

Table B-1: Natural frequency for five fundamental oscillation modes for torsional scanners

	Effective Mass (M) / Mass Moment of Inertia (J_{eff})	Spring Constant, K_s
1. Torsion	$J_{eff} = J_{m,xx} + (2/3)J_{f,xx}$ $J_{f,xx} = \frac{1}{3}M_f(a^2 + b^2)$ $M_f = 4abL_f$	$K_s = \frac{2GK}{L_f}; \mu = \sqrt{G_x/G_y}$ <p>For $a > b$ use below; for $b > a$, interchange a with b and G_x with G_y</p> $GK = (ab^3G_y) \left(5.33 - 3.36 \frac{b}{a} \frac{1}{\mu} \left(1 - \frac{b^4}{12a^4\mu^4} \right) \right)$
2. Out-of-plane Sliding	$M_{eff} = M_m + \frac{26}{35}M_f$	$K_s = \frac{24E_x I_{yy}}{L_f^3}; I_{yy} = \frac{4}{3}ab^3$
3. In-plane Sliding	$M_{eff} = M_m + \frac{26}{35}M_f$	$K_s = \frac{24E_x I_{zz}}{L_f^3}; I_{zz} = \frac{4}{3}a^3b$
4. Out-of-plane Rocking	$J_{eff} = J_{m,yy} + 2J_f$ $J_f = M_f(0.0095L_f^2 + 0.052L_fL_m + 0.0929L_m^2)$	$K_s = \frac{E_x I_{yy} \left(2 + 6 \left(1 + \frac{L_m}{L_f} \right)^2 \right)}{L_f}$
5. In-plane Rocking	$J_{eff} = J_{m,zz} + 2J_f$	$K_s = \frac{E_x I_{zz} \left(2 + 6 \left(1 + \frac{L_m}{L_f} \right)^2 \right)}{L_f}$

Table B-2: Mass and mass moment of inertia for different mirror (M_m is the mass of the mirror and M_f is the mass of one flexure) shapes.

	M_m	$J_{m,xx}$	$J_{m,yy}$	$J_{m,zz}$
Rectangular Mirror	$\rho L_m D t_m$	$\frac{M_{mirr}}{12} (D^2 + t_m^2)$	$\frac{M_{mirr}}{12} (L_m^2 + t_m^2)$	$\frac{M_{mirr}}{12} (D^2 + L_m^2)$
Elliptical Mirror	$\frac{\pi}{4} \rho L_m D t_m$	$\frac{M_{mirr}}{12} \left(\frac{3}{4} D^2 + t_m^2 \right)$	$\frac{M_{mirr}}{12} \left(\frac{3}{4} L_m^2 + t_m^2 \right)$	$\frac{M_{mirr}}{16} (D^2 + L_m^2)$
Circular Mirror	$\frac{\pi}{4} \rho D^2 t_m$	$\frac{M_{mirr}}{12} \left(\frac{3}{4} D^2 + t_m^2 \right)$	$\frac{M_{mirr}}{12} \left(\frac{3}{4} D^2 + t_m^2 \right)$	$\frac{M_{mirr}}{8} (D^2)$

REFERENCES

- [1] P.F. Van Kessel, L.J. Hornbeck, R.E. Meier, M.R. Douglass, "A MEMS-based projection display," *Proceedings of the IEEE*, vol. 86, is. 8, pp. 1687-1704 Aug. 1998.
- [2] H. Urey, "Retinal Scanning Displays", *Encyc. of Optical Engineering*, Marcel-Dekker, 2003.
- [3] H. Urey, "MEMS Scanners for Display and Imaging Applications," submitted to *Photonics East*, 2004.
- [4] H. Urey, D.W. Wine, J. R. Lewis, "Scanner design and resolution tradeoffs for miniature scanning displays," *SPIE Proc. of Conference on Flat Display Technology and Display Metrology*, vol. 3636, pp.60-68, 1999.
- [5] A. Wolter, H. Schenk, E. Gaumont, H. Lakner, "MEMS microscanning mirror for barcode reading: from development to production," *SPIE Proc. of MOEMS Display and Imaging Systems II*, vol. 5348, pp. 32-39, 2004.
- [6] H. Schenk, U. Dauderstädt, P. Dürr, A. Gehner, A. Wolter, H. Lakner, "Light processing with electrostatically driven micro scanning mirrors and micro mirror arrays," *SPIE Proc. of MOEMS Display and Imaging Systems II*, vol. , pp. , 2004.
- [7] K. Roscher, H. Grätz, H. Schenk, A. Wolter, H. Lakner, "Low cost projection device with a 2D resonant microscanning mirror," *SPIE Proc. of MOEMS Display and Imaging Systems II*, vol. 5348, pp. 22-31, 2004.
- [8] R.A. Conant, P.M. Hagelin, U. Krishnamoorthy, O. Solgaard, K.Y. Lau, R.S. Muller, "A raster-scanning full-motion video display using polysilicon micromachined mirrors", *Proc. of the 1999 Int. Conf. on Solid-State Sensors and Actuators (Transducer '99)*, pp. 376-379, Sendai, Japan, June 7-10, 1999.
- [9] J.H. Lee, Y. C. Ko, D.H. Kong, J.M. Kim, K. B. Lee, D. Y. Jeon, " Design and fabrication of scanning mirror for laser display," *Sensors and Actuators A*, vol. 96, p. 223-230, 2002.
- [10] D.L. Dickensheets, G.S. Kino, "Silicon-micromachined scanning confocal optical microscope," *Journal of Microelectromechanical Systems*, vol. 7, pp. 38-47, 1998.
- [11] A.Q. Liu, X.M. Zhang, V.M. Murukeshan, Q.X. Zhang, Q.B. Zou, S. Uppili, "An optical crossconnect (OXC) using drawbridge micromirrors," *Sensors and Actuators A*, vol. 97-98, p. 227-238, 2002.

- [12] H. Toshiyoshi, H. Fujita, "An electrostatically operated torsion mirror for optical switching device," *Proceedings of the 1995 Int. Conf. on Solid-State Sensors and Actuators (Transducer '99)*, vol. 68-B1, p. 199-200, 1995.
- [13] H. Toshiyoshi, D. Miyauchi, H. Fujita, "Electromagnetic Torsion Mirrors for Self-Aligned Fiber-Optic Crossconnectors by Silicon Micromachining," *IEEE Journal of Selected Topics in Quantum Electronics*, vol. 5, no. 1, p. 10-17, 1999.
- [14] H.R. Shea, A. Gasparyan, "Design for reliability of drift free MEMS microscanners," *SPIE Proc. of MEMS, MOEMS and Micromachining*, vol. 5455, pp. 44-53, 2004.
- [15] H. Xie, Y. Pan, G. K. Fedder, "Endoscopic optical coherence tomography imaging with a CMOS-MEMS micromirror," *Sensors and Actuators A*, vol. 103, p. 237-241, 2003.
- [16] Y. Yee, H.J. Nam, S.H. Lee, J.U. Bu, J.W. Lee. "PZT actuated micromirror for fine-tracking mechanism of high-density optical data storage," *Sensors and Actuators A*, vol. 89, p. 166-173, 2001.
- [17] J. Comtois, A. Michalicek, W. Cowan, J. Butler, "Surface-micromachined polysilicon MOEMS for adaptive optics," *Sensors and Actuators*, vol. 78, p. 54-62, 1999
- [18] F. Zimmer, H. Grueger, A. Heberer, A. Wolter, H. Schenk, "Development of an NIR microspectrometer based on a MOEMS scanning grating," *SPIE Proc. of MEMS, MOEMS and Micromachining*, vol. 5455, pp. 9-18, 2004.
- [19] H.Y. Lin, W. Fang, "A rib-reinforced micro torsional mirror driven by electrostatic torque generators," *Sensors and Actuators A*, vol. 105, pp. 1-9, 2003.
- [20] T.G. Bifano, J. Perreault, R.K. Mali, and M.N. Horenstein, "Microelectromechanical Deformable Mirrors," *IEEE Journal of Selected Topics in Quantum Electronics*, vol. 5, no. 1, pp. 83-89, 1999.
- [21] S. Kwon, V. Milanovic, L.P. Lee, "A High Aspect Ratio 2D Gimbaled Microscanner with Large Static Rotation," *presented in IEEE/LEOS Optical MEMS 2002*, Lugano, Switzerland, Aug. 2002.
- [22] D. Lee, U. Krishnamoorthy, K. Yu, O. Solgaard, "Single-crystalline silicon micromirrors actuated by self-aligned vertical electrostatic combdrives with piston-motion and rotation capability," *Sensors and Actuators A*, to be published.
- [23] L. Houlet, P. Helin, T. Bourouina, G. Reyne, E.D. Gergam, H. Fujita, "Movable vertical mirror arrays for optical microswitch matrixes and their electromagnetic actuation," Presented in Solid-State Sensor, Actuator and Microsystems Workshop Hilton Head Island, South Carolina, June 2-6, 2002.
- [24] J.J. Bernstein, W.P. Taylor, J.D. Brazzle, C.J. Corcoran, G. Kirkos, J.E. Othner, A. Pareek, M. Waelti, M. Zai, "Electromagnetically actuated mirror arrays for use in 3-D

- optical switching applications,” *Journal of Microelectromechanical Systems*, vol. 13, Issue: 3, pp. 526-535, June 2004.
- [25] Y. Okano, Y. Hirabayashi, “Magnetically actuated micromirror and measurement system for motion characteristics using specular reflection” *IEEE Journal on Selected Topics in Quantum Electronics*, vol. 8, no.1, January/February 2002.
- [26] C. Liu, Y.W. Yi, “Micromachined Magnetic Actuators Using Electroplated Permalloy,” *IEEE Trans. on Magnetics*, vol. 35, no. 3, 1999.
- [27] L.K. Lagorce, O. Brand, M. G. Allen, “Magnetic microactuators based on polymer magnets,” *IEEE Journal of Microelectromechanical Systems*, vol. 8, no. 1, 1999.
- [28] S. Schweizer, S. Calmes, M. Laudon, Ph. Renaud, “Thermally actuated optical microscanner with large angle and low consumption”, *Sensors and Actuators*, vol. 76, pp. 470-477, 1999.
- [29] M. Sasaki, T. Yamaguchi, J. H. Song, K. Hane, M. Hara, and K. Hori, “Optical Scanner on a Three-Dimensional Microoptical Bench”, *Journal of Lightwave Technology*, vol. 21, no. 3, pp. 602-608, March 2003.
- [30] *Piezoelectricity*, Available online at <http://hyperphysics.phy-astr.gsu.edu/hbase/solids/piezo.html>
- [31] K.H. Chau, S. Dimitrijevic, “ Two-dimensional microscanner actuated by PZT thin film,” *SPIE Proc. of Device and Process Technologies for MEMS and Microelectronics*, vol. 3892, pp. 133-140, October 1999.
- [32] F. Filhol, E. Defaÿ, C. Divoux, C. Zinck and M-T. Delaye, “Piezoelectric micromirrors for fast optical scanning with large angular deflection,” presented in *IEEE/LEOS International Conference on Optical MEMS and Their Applications*, Kagawa, Japan, 2004.
- [33] H. Schenk, P. Dürr, D. Kunze, H. Lakner, H. Kück, “A resonantly excited 2D micro-scanning-mirror with large deflection,” *Sensors and Actuators A*, vol. 89, pp.104-111 (2001).
- [34] H. Shenk, P. Dürr, T. Haase, D. Kunze, U. Sobe, H. Lakner, H. Kück, “Large deflection micromechanical scanning mirrors for linear scans and pattern generation,” *Journal of Selected Topics in Quantum Electronics*, vol. 6, no. 5, pp.715-722 (2000).
- [35] H. Schenk, A. Wolter, H. Lakner, “Design optimization of an electrostatically driven micro scanning mirror,” *SPIE Proc. of the Conf. on MOEMS and Miniaturized Systems*, vol. 4561, pp.35-44, San Francisco, Calif., USA, 2001.
- [36] H. Urey, C. Kan, W.O. Davis, “Vibration mode frequency formulas for Microscanners,” *IEEE Journal of Microelectromechanical Systems*, submitted for publication.

- [37] Z. Xiaoa, W. Penga, R.F. Wolffenbuttel, K.R. Farmera, "Micromachined variable capacitors with wide tuning range," *Sensors and Actuators A*, vol.104, pp.299-305, 2003.
- [38] C. T. C. Nguyen, "High-Q micromechanical oscillators and filters for communications," *IEEE Proc. of the International Symposium on Circuits and Systems*, pp.2825-2828 1997.
- [39] L-J. Yanga, T-W. Huangb, P-Z. Changb, "CMOS microelectromechanical band-pass filters," *Sensors and Actuators A*, vol. 90, p.148-152, 2001.
- [40] L. Lin, R. T. Howe, A. P. Pisano, "Micromechanical filters for signal processing," *Journal of Microelectromechanical Systems*, vol. 7, no. 3, p.286-294 (1998).
- [41] J. D. Grade, K. Y. Yasumura, H. Jerman, "A DRIE comb-drive actuator with large, stable deflection range for use as an optical shutter," *IEEE/EDS Proc. of International Conference on Solid-State Sensors, Actuators and Microsystems*, Boston, Massachusetts, USA 2003.
- [42] T.D. Kudrle, G.M. Shedd, C.C. Wang, J.C. Hsiao, M.G. Bancu, G.A. Kirkos, N. Yazdi, M. Waelti, H. Sane, C.H. Mastrangelo, "Pull-in suppression and torque magnification in parallel plate electrostatic actuators with side electrodes," *IEEE Proc. of The 12th International Conference on Solid State Sensors, Actuators and Microsystem*, vol. 0-7803-7731-1, pp. 360-363, 2003.
- [43] Y. Nemirovsky, O. Bochobza-Degani, "A methodology and model for the pull-in parameters of electrostatic actuators," *IEEE Journal of Microelectromechanical Systems*, vol. 10, Issue 4, pp. 601-605, Dec. 2001.
- [44] T. Sandner, T. Klose1, A. Wolter, H. Schenk, H. Lakner, W. Davis, "Damping Analysis and Measurement for a Comb-Drive Scanning Mirror," *Proc. of SPIE Photonics Europe Conf.*, vol., pp., 2004.
- [45] W.A. Johnson, L.K. Warne, "Electrophysics of Microelectromechanical Comb Actuators," *IEEE Journal Microelectromechanical Systems*, vol. 4, no. 1, pp. 49-59, March 1995.
- [46] C. Chen, C. Lee, "Design and modeling for comb drive actuator with enlarged static displacement," *Sensors and Actuators A*, vol. 115, pp. 530-539, 2004.
- [47] M. Tilleman, "Analysis of electrostatic comb-driven actuators in linear and nonlinear regions," *International Journal of Solids and Structures*, vol. 41, pp. 4889-4898, 2004.
- [48] W. Huang, G. Lu, "Analysis of lateral instability of in-plane comb drive MEMS actuators based on a two-dimensional model," *Sensors and Actuators A*, vol. 113, pp. 78-85, 2004.
- [49] P. Bruschi, A. Nannini, F. Pieri, G. Raffaa, B. Vigna, S. Zerbini, "Electrostatic analysis of a comb-finger actuator with Schwarz-Christoffel conformal mapping," *Sensors and Actuators A*, vol. 113, pp. 1060

- [50] J.P. Raskin, A.R. Brown, B. Khuri-Yakub, G.M. Rebeiz, "A novel parametric-effect MEMS amplifier," *Journal of Microelectromechanical Systems*, vol. 9, pp. 528–537, 2000.
- [51] A. Olkhovets, D.W. Carr, J.M. Parpia, H.G. Craighead, "Nondegenerate nanomechanical parametric amplifier," *IEEE Proc. of 14th International Conference on Micro Electro Mechanical Systems*, pp. 298-300, Interlaken, Switzerland, 21–25 January 2001.
- [52] K.L. Turner, W. Zhang, "Design and analysis of a dynamic MEM chemical sensor," *Proc. of American Control Conference*, pp. 1214-1218, Arlington, VA, USA, 25–27 June 2001.
- [53] K.L. Turner, S.A. Miller, P.G. Hartwell, N.C. Macdonald, S.H. Strogartz, S.G. Adams, "Five parametric resonances in a microelectromechanical system," *Nature* vol. 396 pp.149–152, 1998.
- [54] A. H. Nayfeh, D. T. Mook, "Nonlinear Vibrations," Jon Wiley and Sons, New York, 1995.
- [55] V. V. Konotop, V. Kuzminak, "Parametric resonance of a defect mode in a 2D photonic crystal," *Physical Review B*, vol. 64, pp.1-7, (2001).
- [56] P. Wegrzyn, "Parametric resonance in a vibrating cavity," *Physics Letters A*, vol.322, pp.263-269, 2004.
- [57] A.A. Popov, "Parametric resonance in cylindrical shells: a case study in the nonlinear vibration of structural shells," *Engineering Structures*, vol.25, pp.789-799 2003.
- [58] M-F. Yu, G. J. Wagner, R. S. Ruoff, M. J. Dyer, "Realization of parametric resonances in a nanowire mechanical system with nanomanipulation inside a scanning electron microscope," *Physical Review B*, vol.66, pp. 2002.
- [59] "Mathieu Function – from Mathworld," Available Online at <http://mathworld.wolfram.com/MathieuFunction.html>
- [60] J.S. Rao, *Advanced Theory of Vibration*, Jon Wiley and Sons, New York, 1992.

VITA

Çağlar Ataman was born in Rize, Turkey, in 1981. He received his B.Sc. degree from Bilkent University, Ankara, in 2002. Same year, he joined Optical Microsystems Laboratory (OML) of Koç University, Department of Electrical Engineering as an M.Sc candidate. Çağlar Ataman is a student member of SPIE.



Dynamic Modeling of Comb Actuated Microscanners

Çaglar Ataman, Hakan Urey, *Member, IEEE*

Abstract— Comb-drive actuation is commonly utilized in today's MEMS devices. Dynamic characteristics of comb-actuated devices are predominantly determined by the nature of the forcing function of the actuators, which depends on the mode of operation (torsion, in-plane or out-of-plane translation mode, etc.). In this work, we investigate a torsional mode comb-actuated microscanner. The device exhibits unusual frequency and transient response characteristics, such as subharmonic oscillations, multiple parametric resonances, and alternating-oscillation-frequency. We present an analytical and a numerical model for the dynamic behavior of the device. Our analytical model, which is based on solution of linear Mathieu equation, is valid for small angular displacements and low air-damping, while the numerical model also remains valid when those restrictions are not satisfied. Both models successfully predict the parametric resonance of the microscanner that leads to the aforementioned characteristics. We present experimental results under various ambient pressures and excitation schemes to validate the modeling results.

Index Terms— Comb-drive actuation, microscanner, subharmonic oscillation, parametric resonance, frequency response, dynamic behavior

I. INTRODUCTION

ELECTROSTATIC comb-drive actuation is a common actuation mechanism in today's microelectromechanical systems (MEMS). Comb-actuated structures are multi degree-of-freedom actuators; they can be actuated in different mechanical modes, such as torsional, in-plane sliding, and out-of-plane sliding modes. The vibration mode of the actuator is the predominant factor that determines the system dynamics. In in-plane sliding mode, the force induced by the actuator is dependent of the displacement of the combs, and the actuator exhibits a simple harmonic oscillatory (SHO) behavior. This type of comb-actuators are studied in detail in the literature [1-3] and utilized in various applications, such as MEMS motors [4], tunable capacitors [6], mechanical resonators [7], optical switches [8], and mechanical filters for RF and other applications, [9]-[9].

In this paper we discuss the torsional mode comb actuators, whose dynamics are more complicated than that of their in-plane counterparts. Torsional actuators are mainly used for laser beam scanning and beam steering for display [10], imaging [11], and optical switching [12] applications. A torsional comb-actuated microscanner is not a SHO and can be classified as a "Parametrically Excited System", which exhibits multiple resonances, hysterical frequency response, subharmonic oscillations and alternating-oscillation-frequency characteristics. Those characteristics are observed both experimentally and in numerical simulations and discussed in detail in subsequent sections.

A parametrically excited system is governed by a 2nd order differential equation, in which the time-dependent excitations appear as coefficients (parameters) of the equation. Such systems frequently arise in different areas of science and engineering, such as photonic crystals [13], optical cavities [14], plate vibrations [15], and nano-scale devices [16]. In simple harmonic systems, a small excitation cannot create a large response unless the excitation frequency is close to the resonance frequency of the system (primary resonance). However, a small parametric excitation can produce a large response when frequency of the excitation is close to twice the natural frequency (f_n) of the system (principal parametric resonance) or an integer fraction of $2f_n$. The resonance around $2f_n/n$ is called the n th order parametric resonance. We have experimentally observed up to 8 parametric resonances with square-wave excitation in atmospheric pressure, which is the largest number of parametric resonance reported for a micromechanical structure. A similar comb-actuated out-of-plane actuator that was reported to be a parametric oscillator is a mass flow sensor [17]. Up to five parametric resonances were observed for this device in vacuum, but the discussion was limited to steady-state response corresponding to a small angle excitation using square-root sine wave as the input waveform. In this paper, we discuss both the transient and the steady-state responses for sinusoidal and square-wave excitations. In addition, we developed a numerical model for accurate prediction of frequency behavior that is valid for both small and large deflections. Proposed analytical and numerical modeling approaches provide a simple yet powerful way to analyze the nonlinear frequency response of comb actuators and simplify the design process for microscanners.

This work was supported in part by Microvision, Inc. USA, and Fraunhofer, IPMS, Germany.

H. Urey is with the Department of the Electrical Engineering of Koc University, Rumeli Feneri Yolu, 34450, Sariyer, Istanbul, Turkey (phone: 90 212 338 17 74; fax: +90 212 338 00 00; e-mail: hurey@ku.edu.tr).

C. Ataman is an Ph.D. student in the same department. (e-mail: ataman@ku.edu.tr).

The organization of the paper is as follows: In section 2, we briefly explain the device layout, fabrication, and principle of operation. In section 3 we present numerical predictions for transient and steady-state behavior and experimental confirmation of the results for small and large deflections at

ous pressure levels. In section 4, we discuss analytical models that work well for small excitation amplitude and damping conditions.

II. THE DEVICE

A. Layout

The device under investigation is a torsional, comb actuated, single-crystalline microscanner fabricated by Fraunhofer Institute for Photonics Microsystems (IPMS) in Dresden, Germany. The microscanner is fabricated on a 30 μm thick Si wafer with a CMOS compatible process [18]. Fig. 1 is a micrograph showing the overall layout of the device. The reflective area in the middle is a 2 mm by 2 mm movable mirror, which is bonded to the fixed outer frame by two flexure beams. Comb fingers are placed on either side of the reflective mirror. For device operation, complementary fingers on the mirror and the frame should be electrically isolated. This isolation is maintained by the filled isolation-trenches that form an insulating channel between the required portions of the device. These trenches are fabricated by first etching a 1 μm thick channel on the silicon structural layer using ASETM process, then covering the side walls of the channel by 90 nm thick insulating oxide, and at last filling the channel with PECVD-polysilicon. Comb fingers, flexure beams and other structural elements are defined by another ASETM process. Fig. 2 is an SEM image of the comb fingers.

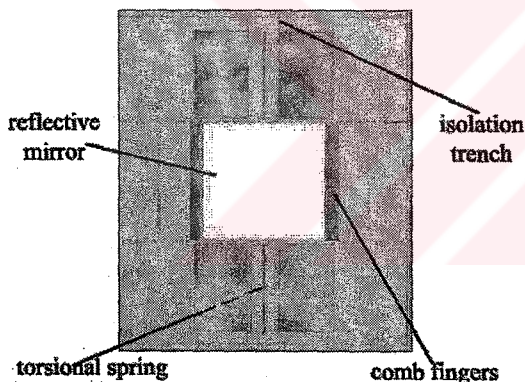


Fig. 1. Sketch of the torsional microscanner. The internal mirror is 2 mm x 2 mm, while entire device is 5 mm x 5 mm, and placed inside a ceramic package



Fig. 2. Micrograph of the electrostatic comb drive actuators of IPMS microscanners (only movable fingers are shown) [18]

B. Torsional Actuators and Equation of Motion

Comb-drive actuators can induce mechanical motion both in out-of-plane and in-plane modes. Which of these modes is the actual oscillation mode is determined by the driving frequency and modal characteristics of the device. For scanning applications, it is critical that the fundamental (1st) mechanical

mode of a microscanner structure is the rotation around the flexure axis, called *the torsional mode*. Regardless of the operation mode, force (or torque) associated with comb actuators is proportional to the rate of change of capacitance with respect to the displacement and the square of the driving voltage. Despite the displacement independent force of in-plane mode comb drives, the torque induced by the torsional mode comb-actuators is strongly dependent on the displacement (tilt angle). The torque can be expressed as;

$$M(\theta) = N \frac{dC}{d\theta} V(t)^2 \quad (1)$$

where N is the total number of comb fingers on single side of the mirror, C is the capacitance of a single finger, θ is the tilt angle and $V(t)$ is the periodic driving signal. The derivative of the total capacitance introduces the θ dependence into the torque function. Fig. 3 shows capacitance-displacement and rate of change of capacitance with respect to displacement curves for a single finger of a torsional comb actuator obtained using FEMLAB[®];

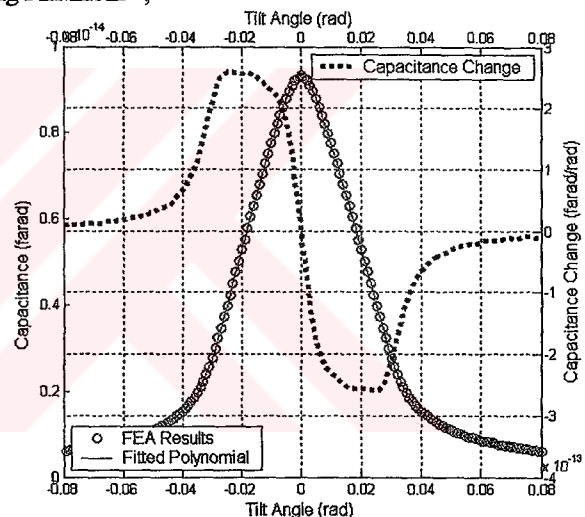


Fig. 3. Capacitance vs. deflection curve and its derivative for a single comb finger. A high order polynomial is fitted to the FEA simulation data of capacitance curve. The fitted polynomial is differentiated to obtain the capacitance change vs. deflection curve.

Dynamic behavior of the microscanner can be modeled by a second order nonlinear differential equation (equation of motion – EoM) with a single degree of freedom (DOF), since the mode separation and quality factor (Q) of the device are sufficiently high to ensure that there is no coupling between different modes. The EoM is given by the expression, [19]

$$I_m \frac{d^2\theta}{dt^2} + b \frac{d\theta}{dt} + K_f \theta = M(\theta) \quad (2)$$

where, I_m is the mass moment of inertia, b is the air damping, K_f is the torsional stiffness of the flexures, and $M(\theta)$ is the net torque given by (1). Analytical expressions for moment of inertia of a box shaped mirror and torsional stiffness of the flexure beams are available in the literature [21]. More

rate values for these parameters can be extracted using a finite Element Analysis (FEA) software. Quality factor, before the damping term in the equation of motion, is measured experimentally. A position sensing device and a PC data acquisition card is utilized to record the free damped oscillations of the device after the excitation is turned off while the device is in operation. The quality factor is then determined from the time constant of the damped oscillations fitting a curve to the recorded data. An analytical model of damping mechanism between the comb fingers is given in [1]. Coefficients in (2) for the device under investigation at different ambient pressures are given in Table I.

TABLE I
DEVICE PARAMETERS AT VARIOUS AMBIENT PRESSURES

Pressure (Torr)	I_m (kg.m)	b (N.s/m)	K_f (N/m)	Q
Atm	9.32E-14	4.21E-13	4.28E-06	22
30 mTorr	9.32E-14	2.87E-11	4.28E-06	1250

Table 1. System parameters measured at different ambient pressures.

Numerical simulations are performed by numerically solving the equation of motion using MATLAB® ODE solvers. The slight asymmetry in the structure, which triggers oscillations, is introduced as a small initial tilt angle. For certain portions of the excitation spectrum, the system has multiple stable solutions, where the choice of initial conditions determines the actual solution.

III. DYNAMIC BEHAVIOR OF THE DEVICE

Due to the displacement dependent torque, time and frequency domain behavior of a torsional comb-actuated microscanner is significantly different than the dynamics of a near resonant oscillator. In this section, we present experimental results on the frequency and time domain characteristics of the device for torsional mode operation. We also give numerical simulation data together with the experimental results.

A. Frequency Domain Characteristics

1) Square-root Sinusoidal Excitation

The torque produced by the comb-actuators is proportional to the square of the input voltage. Therefore, in order to get periodic coefficients of single frequency in the EoM, the driving signal should be a square-root sinusoid $V = A\sqrt{\cos(\omega t) + 1}$ to obtain a harmonic V^2 term in the forcing function expression. Fig. 4 (a) and (b) show the frequency response curves for such an excitation at atmospheric pressure (760 Torr), and at 30 mTorr, respectively. In atmospheric pressure, the device has two parametric resonances, of which the fundamental one is located around twice the mechanical resonance frequency (f_r). At 30 mTorr, the device experiences a much lower air damping, and frequency response is significantly different. Due to the lack of the stabilizing effect of the damping, the number of observable parametric resonances and maximum oscillation amplitude are increased. All orders of resonances are similar in shape, and they are located around excitation

frequencies of $2f_r/n$, $n=1, 2, 3, 4$. Maximum oscillation amplitude scales down as n increases. However, oscillation frequency of the device is always close to f_r , regardless of the order of the resonance.

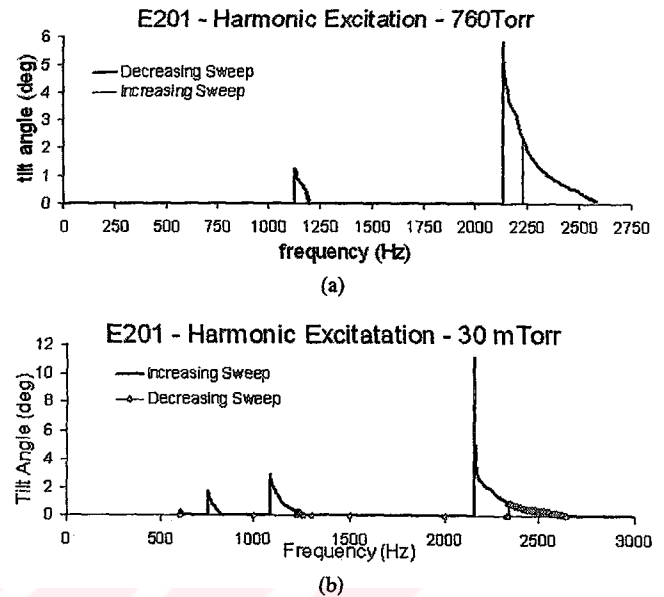


Fig. 4. Experimental frequency response data at (a) atmospheric pressure (760 Torr), (b) at 30 mTorr. Excitation signal is a square-root sine wave with $V_{p-p}=20$ for both plots

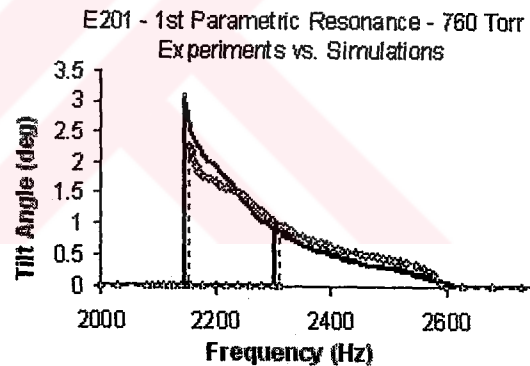


Fig. 5. Comparison of simulation (dashed line) and experimental (solid line) results for the 1st order parametric resonance in atmospheric pressure.

Fig. 5 shows the comparison of numerical and experimental results for the frequency response of the device in the first parametric resonance. Upsweep and downsweep simulations are done with different initial conditions. For the upsweep a small tilt angle is introduced to simulate the asymmetries in the structure, and the oscillations converge to the trivial solution. For downsweep, an initial tilt angle greater than the maximum oscillation amplitude is used, so that the oscillations converge to nontrivial solution.

2) Square-wave Excitation

When the excitation waveform is different than a square-root sinusoid, the torque in the system is no longer a harmonic function. Fig. 6 is the frequency response curve of the device for square wave excitation. Number of observable parametric resonances is more than the square-root sine excitation voltage case. Fig. 6 shows 8 parametric resonances at atmospheric

measure. However, monotonous decrease in the maximum oscillation amplitude as the order of resonances grows is also present with square-wave excitation. This reveals that the higher harmonic content of the square-wave signal gives rise to the other resonances. Hysteresis in the response curve is present for all 8 resonances, but the jump frequencies are different than the square-root sine excitation voltage case.

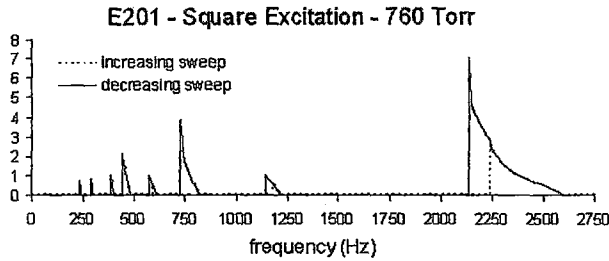


Fig. 6. Experimental frequency response data at 760 Torr (1 Atm) and with 20 V, square wave excitation. Number of observable parametric resonances is 8, due to the higher harmonics in the square wave excitation.

Multiple parametric resonances and very sharp hysteresis jumps in the frequency response curves make this device a potential candidate for various applications, such as parametric amplification, mass resonator, impact detectors, etc.

Time Domain Characteristics

The time domain characteristics of the device are also determined by the parametric nature of the microscanner.

Transient Response

Fig. 7 shows the behavior of the output amplitude until the system reaches steady state. Excitation voltage waveform is a square-root sinusoid for both 7a and 7b, but the frequencies are different. Fig. 7a shows the transient response of the device, when it is driven with a frequency f greater than f_2 . Unlike linear systems, oscillation amplitude grows with a positive exponential manner, until it reaches a maximum value, then it shows an underdamped oscillatory behavior until it settles at a steady-state value. If the drive frequency is very close to the boundary between the stable and unstable regions ($f \approx f_2$), damped oscillatory behavior in the output amplitude diminishes, and the device reaches steady-state immediately after the positive-exponential growth.

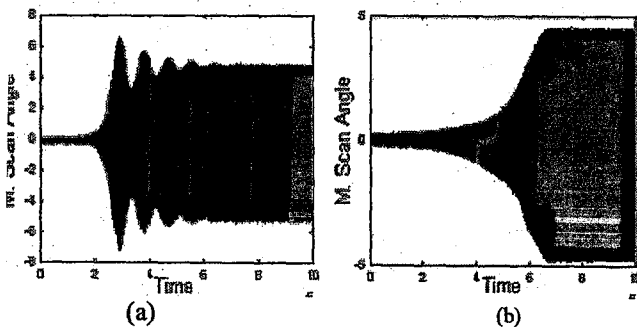


Fig. 7. Transient response of the device. (a) $f_{ex} > f_2$ (stable region); (b) $f_{ex} = f_2$ (boundary of the unstable region).

Steady State Response

In steady-state, there is not a linear relationship between the drive signal and oscillation amplitude. The relation between the frequencies of drive and output depends on the order of resonance in which the device is operated. Oscillations in the

1st parametric resonance are called *subharmonic oscillations*, since the drive frequency is twice the oscillation frequency. For the 2nd order resonance, the oscillations and excitation frequencies are the same. For all other resonance orders, drive signal has a lower frequency than the actual oscillations. Fig. 8 shows the input-output relations for the first two orders of resonances.

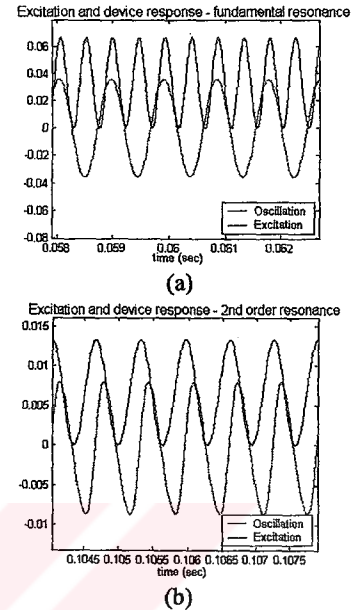


Fig. 8. Excitation and oscillation signals for the first two orders of resonances. (a) Excitation frequency is twice the oscillation frequency (subharmonic oscillation). (b) Excitation and oscillations are of same frequency

For square wave input, the response is not a pure sinusoid for high order resonances. Scan wave shows an unusual behavior and changes oscillation frequency and amplitude at each half cycle of the square wave. When excitation is in the OFF state (meaning that no torque is present in the system), the system makes free oscillation at its natural resonant frequency, when the excitation is in the ON state, the mirror oscillates at a higher frequency, which can be calculated using the excitation and natural frequencies. This phenomenon is called *alternating-oscillation-frequency*. Fig. 9 shows the experimental results illustrating this behavior. Such behavior is observed in higher order resonances when excited with a square-wave. This phenomenon is also predicted in the numerical simulations.

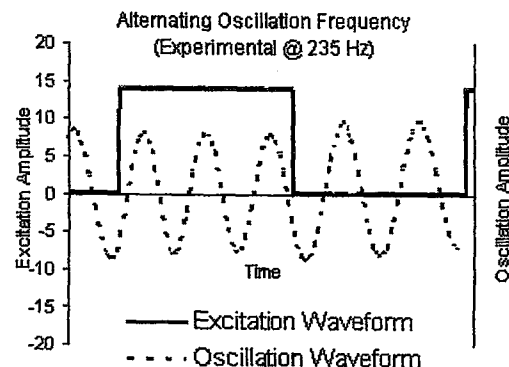


Fig. 9. Alternating oscillation phenomenon at higher order resonances with 380 Hz square wave excitation (Experimental result)

oltage Domain Characteristics

tage domain behavior refers to the response of the device changes in the excitation amplitude. Fig.10 shows the relationship between the maximum mechanical deflection angle and the excitation amplitude. The deflection values are measured at the peak of the first order resonance of the microscanner. Regardless of the waveform of the excitation, maximum deflection angle grows linearly with the increasing excitation amplitude.

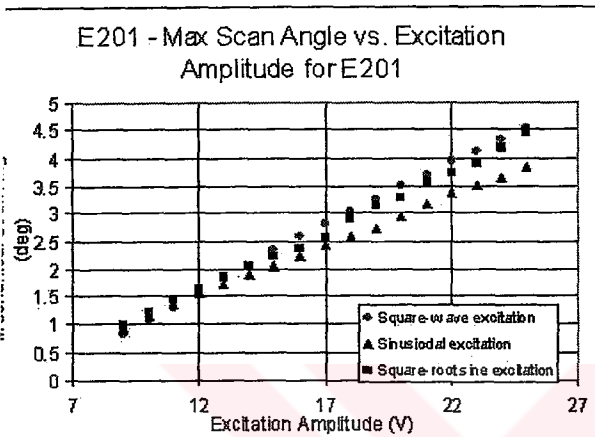


Fig. 10. Maximum scan angle vs. excitation amplitude with square-wave, sinusoidal and square-root sine excitation. Experimental results belong to E201.

IV. ANALYTICAL MODELING

For small angular displacements, the rate of change of total capacitance with angle, illustrated in Figure 3, can be approximated with a third order polynomial. If the excitation signal is chosen to be a squared-root sinusoid ($\gamma(t) = A\sqrt{\cos(\omega t) + 1}$), torque induced by the comb-actuator can then be expressed as;

$$\mathcal{I}(\theta, t) = -(r_3\theta^3 + r_1\theta)A^2(\cos(\omega t) + 1) \quad (3)$$

where r_1 and r_3 are the coefficients of the cubic polynomial fit of the deflection-derivative of capacitance. The simplified equation of motion can be rewritten by substituting (3) into (2):

$$\frac{d^2\theta}{d\tau^2} + 2\alpha\frac{d\theta}{d\tau} + (\beta + 2\delta_1\cos(2\tau))\theta + (\delta_3 + \delta_3\cos(2\tau))\theta^3 = 0 \quad (4)$$

$$\text{where, } \tau = \frac{\omega t}{2}, \alpha = \frac{b}{\omega I_m}, \beta = 4\frac{(r_1A^2 + K_f)}{\omega^2 I_m}, \delta_1 = \frac{2r_1A^2}{\omega^2 I_m}, \delta_3 = \frac{4r_3A^2}{\omega^2 I_m}$$

Neglecting the nonlinear term in (4) simplifies the analysis for the analytical treatment that follows; the effect of cubic nonlinearity will be discussed later:

$$\frac{d^2\theta}{d\tau^2} + 2\alpha\frac{d\theta}{d\tau} + (\beta + 2\delta_1\cos(2\tau))\theta = 0 \quad (5)$$

Introducing the change of variable $\phi(\tau) = \theta(\tau)\exp(\alpha\tau)$ into (5) simplifies the differential equation and leads to [23]

$$\frac{d^2\phi}{d\tau^2} + p(\tau)\phi = 0 \quad (6)$$

where $p(\tau) = \xi + 2\delta_1\cos(2\tau)$, and $\xi = (\beta - \alpha^2)$. This linear and homogeneous differential equation with periodic coefficients is known as the *Mathieu's equation* [24]. There are several methods in the literature to analyze the dynamics of this equation. Our solution follows the *Floquet theory* analysis of (7) detailed in Ref. [24] in order to determine the form of possible solutions. Then we perform a stability analysis based on the results of Floquet theory using the *method of strained parameters*.

A. Transient Behavior

Eq. (6) can be written in state-space representation as follows:

$$\begin{bmatrix} \dot{x}_1 \\ \dot{x}_2 \end{bmatrix} = \begin{bmatrix} 0 & 1 \\ -p(\tau) & 0 \end{bmatrix} \begin{bmatrix} x_1 \\ x_2 \end{bmatrix} \quad (7)$$

where, $x_1 = \theta$ and $p(\tau) = \beta + 2\delta_1\cos(2\tau)$. Since (7) is a linear, second-order homogeneous system of differential equations, it has two linearly independent solutions, which forms a solution space. Floquet theory suggests that there exists a fundamental solution set $v_1(\tau)$ and $v_2(\tau)$, which satisfies the following relation [23]:

$$v_i(\tau + n\pi) = \lambda_i^n v_i(\tau), \quad i = 1, 2 \quad (8)$$

where, $\lambda_{1,2}$ are the eigenvalues of a special matrix called the *characteristic matrix*. If $X(\tau)$ is a fundamental solution matrix, whose columns are the two linearly independent solutions, which satisfy the initial conditions $X(0) = I$, where I is the identity matrix, the characteristic matrix C of (7) can be computed from, [22]

$$C = X(T) = \begin{bmatrix} x_1(T) & \dot{x}_1(T) \\ x_2(T) & \dot{x}_2(T) \end{bmatrix} \quad (9)$$

where, $T = \pi$ is the period of the periodic coefficient $p(\tau)$. Solutions and the stability of (6) can be determined using this characteristic matrix. In order to determine the characteristic matrix, the system should be numerically integrated from $\tau = 0$, for one period of the coefficients, with the initial conditions $X(0) = I$. Once the entries of C are determined, the solutions and stability of the system be extracted. Let $\theta_{1,2}(t)$ denote the solutions of the; then the form of the solutions are given by the relation.

$$\begin{aligned} \theta_1(\tau) &= \exp(\gamma_1\tau)\phi_1(\tau) \\ \theta_2(\tau) &= \exp(\gamma_2\tau)\phi_2(\tau) \end{aligned} \quad (10)$$

re, γ_1 and γ_2 are called the *characteristic exponents*, and i_j are linear combinations of sinusoids of periods π and 2π . The characteristic exponents of (6) are given by

$$= \frac{1}{T} \ln(\lambda_i) \quad (11)$$

10 is the general form of the solutions of the linear thieu equation. Depending on the values of the envectors of the characteristic matrix, stability, transient idy state characteristics of the system can be determined. If se eigenvectors are complex conjugates, they have unity dulus and lie on the unit circle. In this case, the steady state put is bounded and the system is stable, however the output plitude shows damped oscillatory behavior due to (14), ich agrees with the transient behavior illustrated in Figure

When one of the eigenvectors of the characteristic matrix ; amplitude greater than unity, one of the fundamental utions die out in time, however the amplitude of the other ation grows exponentially, and the system is unstable ic nonlinearly that was neglected puts an upper bound on : unstable solution amplitude). When $f_{exc}=f_1$ or $f_{exc}=f_2$, the envectors of the characteristic matrix are -1 or 1, due to 2) the solutions at $f_{exc}=f_1$ and $f_{exc}=f_2$ are 2π or π periodic, spectively. Thereby, the oscillatory behavior in the transient sponse diminishes as illustrated in Figure 7a.

3. Stability Tongues

ability curves for the structure defines the boundaries tween stable and unstable regions. The curves form a ngue-like shape in the drive-voltage – drive-frequency ane, and therefore called “stability tongues”. The method of ained parameters is an efficient way to locate these tongues. his method assumes that $u(\tau)$ and ξ can be written as the llowing perturbation expressions:

$$(\tau) = u_0(\tau) + \delta_1 u_1(\tau) + \delta_1^2 u_2(\tau) + \dots \quad (12)$$

$$\xi = \xi_0 + \delta_1 \xi_1 + \delta_1^2 \xi_2 + \dots \quad (13)$$

ubstituting (12) and (13) into (7) and equating the eefficients of same powers of δ gives

$$i_0 + \xi_0 u_0 = 0 \quad (14)$$

$$i_1 + \xi_0 u_1 = -\xi_1 u_0 - 2\xi_0 \cos(2\tau) \quad (15)$$

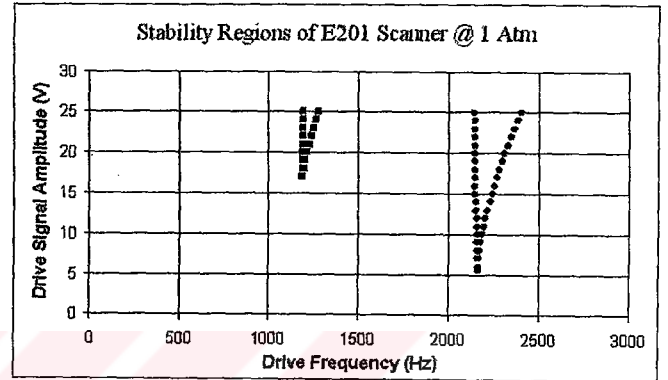
$$i_2 + \xi_0 u_2 = -\xi_2 u_0 - \xi_1 u_1 - 2u_1 \cos(2\tau) \quad (16)$$

qs. (14), (15), and (16) are a set of differential equations, hich can be solved iteratively. Eq. (14) also implies that ξ_0 an only be equal to n^2 due to the second order differential erm. Each specific n value corresponds to a different solution or (14) and different stability tongue. Using this method, the irst two stability tongues for (7) are found as [23]

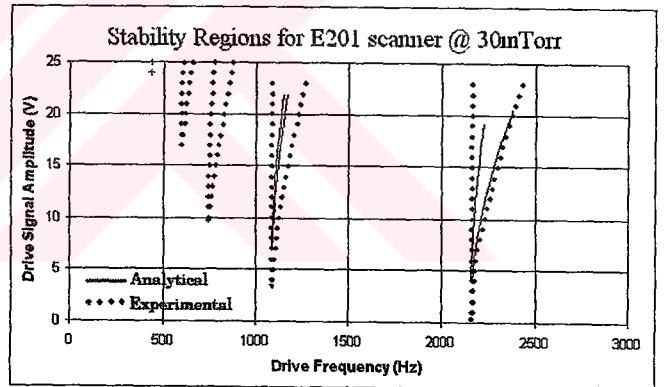
$$\beta = 1 - \delta_1 - \frac{1}{8} \delta_1^2 + \alpha^2 + O(\delta^3) \quad (17)$$

$$\beta = 4 + \frac{5}{12} \delta^2 + \alpha^2 + O(\delta^3) \quad (18)$$

Equations (17) and (18) are given in terms of the parameters introduced in (4). A mapping is required to obtain the stability tongues on the drive-voltage – drive-frequency plane. Fig. 10 shows the experimental results for the stability tongues for the observable parametric resonances at two different ambient pressure levels. Fig. 10b also shows the analytical results for the first two stability tongues mapped onto the drive-voltage – drive-frequency plane.



(a)



(b)

Fig. 11. Stability tongues for the device (a) At atmospheric pressure; (b) At an ambient pressure of 30 mTorr. Dotted lines show experimental results and solid lines in (b) show the stability tongues evaluated using the analytical formulas.

There is a significant viscous air damping between the comb fingers in the atmospheric pressure (measured Q-factor is 22), so that there are only two observable parametric resonances within the operation voltage of the device. Additional orders or resonances would be observed with higher drive voltages, but we avoided such high voltages in order to prevent device failure. The stability tongues of the microscanner in 30 mTorr ambient pressure can be seen in Fig.10b. In low pressure, air damping is much less and therefore the device has a much higher quality factor (Q-factor=1250). As seen in the Fig.10b there are 5 observable parametric resonances and the width of the stability tongues are increased, and their tips came much closer to the $V=0$ axis. In Fig.10b, solid lines represent the results of the analytical expressions of the stability tongues.

small oscillation amplitudes, the analytical results are in good agreement with the experimental data. However, as the driving voltage increases, the deviation of the analytical approximation from the experiments increases. This is due to the fact that for higher voltages, the small driving signal and all tilt angle approximations are becoming invalid and therefore our perturbation analysis ceases to be accurate. Another reason of the difference between the experimental and analytical results is the cubic nonlinearity in (4). As the driving voltage increases, this cubic nonlinearity term also grows and it prevents the left hand of the stability curve to bend rightward.

Quiet analysis showed that within the unstable region, the oscillation amplitude of the device should grow unboundedly, even if damping is present. However, real devices do not have such behavior. This difference is due to the effect of the nonlinearity term neglected before. The effects of nonlinearity can be explained as follows: as the resonance causes the amplitude of the motion to increase, the relation between period and amplitude (which is a characteristic effect of nonlinearity) causes the resonance to detune, decreasing its tendency to produce large motions [26].

V. EXPERIMENTAL SETUP

We developed various optical setups for characterizing the system. Fig. 12 shows a sketch of our setup for frequency, transient response and stability measurements. For the frequency response and stability measurements the actual measurement device is a single photodetector, which is placed very close to the center of the scan line. During device operation, output of the detector is a periodic train of non-pulses. A square wave is formed using the impulse train with the help of a positive edge triggered D-type flip-flop. The complementary output of the flip-flop is connected to the input, therefore at each clock tick (impulse from the detector); the output of the flip-flop switches state, leading to a square wave. From the duty-cycle, phase, and the frequency of this square-wave oscillations of the device can be characterized. This waveform is fed into Lab View via a PC with DAQ interface to evaluate the oscillation frequency, scan angle, and phase to form the complete frequency response of the system. A similar method is used for the damping measurements. For the low-damping experiments, the device is placed inside a vacuum chamber with a transparent bell jar. For transient response measurements, the photodetector is replaced by a fast D-Position Sensing Detector (PSD). Again a laser beam is sent on the microscanner, and the scan waveform of the microscanner is recorded by reflecting the scan-line onto the PSD. Response time of the PSD is much faster than the scan frequency, therefore no deformation of the scan waveform is allowed.

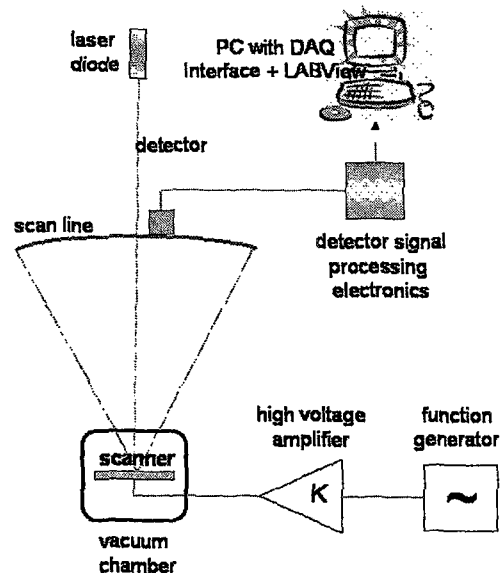


Fig. 12. Schematics of the dynamic micromirror characterization setup

VI. CONCLUSION

In this work, we have presented analytical expressions describing the many fundamental characteristics of comb-actuated microscanners. Having an analytical and numerical tool for predicting microscanner behavior is very valuable. In linear scanners, one avoids having other resonances in the system close to the primary resonance of the scanner and its harmonics. For the nonlinear parametric resonance scanner, one should also pay attention to the subharmonic frequencies in the system. Theory presented here is applied to various science and engineering problems, but to our knowledge, this is the first time that a detailed analysis of the stability, transient and frequency behavior of a parametric resonance device is presented. We developed analytical solution and simulation tools and they confirm our experimental results very well. Our analytical model is valid within small damping and small oscillation angles, but it gives a good understanding of the stability and transient response. On the other hand, our numerical model is valid for both small and large scan angles, providing a very useful tool for scanner design and characterization. The model can also be used for the optimization of both the structure and the drive waveforms.

ACKNOWLEDGMENTS

We'd like to thank Dr. Wyatt Davis (Microvision Inc) and Dr. Alexander Wolter (Fraunhofer IPMS) for helpful discussions

REFERENCES

- [1] C. Chen, C. Lee, "Design and modeling for comb drive actuator with enlarged static displacement," *Sensors and Actuators A*, vol. 115, pp. 530-539, 2004.
- [2] M. Tilleman, "Analysis of electrostatic comb-driven actuators in linear and nonlinear regions," *International Journal of Solids and Structures*, vol. 41, pp. 4889-4898, 2004.
- [3] P. Bruschi, A. Nannini, F. Pieri, G. Raffaa, B. Vigna, S. Zerbini, "Electrostatic analysis of a comb-finger actuator with Schwarz-Christoffel conformal mapping," *Sensors and Actuators A*, vol. 113, pp. 1060

- C. Livermore, A.R. Forte, T. Lyszczarz, S.D. Umans, A.A. Ayon, "High power MEMS electric induction motor," *Journal of Microelectromechanical Systems*, vol. 13, no. 3, pp. 465-471, June 2004.
- Z. Xiaoa, W. Penga, R.F. Wolffenbuttel, K.R. Farmera, "Micromachined variable capacitors with wide tuning range," *Sensors and Actuators A*, Vol.104, p.299-305, 2003.
- C. T. C. Nguyen, "High-Q micromechanical oscillators and filters for communications," *International Symposium on Circuits and Systems, Proc. IEEE*, p.2825-2828, 1997.
- J. D. Grade, K. Y. Yasumura, H. Jerman, "A DRIE comb-drive actuator with large, stable deflection range for use as an optical shutter," *International Conference on Solid-State Sensors, Actuators and Microsystems, Proc. IEEE/EDS*, Boston, Massachusetts, USA, 2003.
- L-J. Yanga, T-W. Huangb, P-Z. Changb, "CMOS microelectromechanical band-pass filters," *Sensors and Actuators A*, Vol. 90, p.148-152, 2001.
- L. Lin, R. T. Howe, A. P. Pisano, "Micromechanical filters for signal processing," *Journal of Microelectromechanical Systems*, Vol. 7, No. 3, p.286-294, 1998.
- 1] Hakan Urey, "High performance resonant MEMS scanners for display and imaging applications (Invited Paper)," in *Optomechatronic micro/nano components, devices, and systems*, Proc. SPIE Vol. 5604, Philadelphia, Pennsylvania, October 2004.
 - 1] H. Schenk, P. Dürr, T. Haase, D. Kunze, U. Sobe, H. Lakner, H. Kück, "Large deflection micromechanical scanning mirrors for linear scans and pattern generation," *Journal of Selected Topics in Quantum Electronics*, Vol. 6, No. 5, p.715-722, 2000.
 - 1] H. Toshiyoshi, D. Hah, S. Huang, H. Nguyen, H. Chang, M. C. Wu, "A low voltage, large scan angle MEMS micromirror array with hidden vertical comb-drive actuators for WDM routers," in *Proc. OFC 2002*, pp. 92-93.
 - 1] V. V. Konotop, V. Kuzminak, "Parametric resonance of a defect mode in a 2D photonic crystal," *Physical Review B*, Vol. 64, p.1-7, 2001.
 - 1] P. Wegrzyn, "Parametric resonance in a vibrating cavity," *Physics Letters A*, Vol.322, p.263-269, 2004.
 - 1] A.A. Popov, "Parametric resonance in cylindrical shells: a case study in the nonlinear vibration of structural shells," *Engineering Structures*, Vol.25, p.789-799, 2003.
 - 1] M-F. Yu, G. J. Wagner, R. S. Ruoff, M. J. Dyer, "Realization of parametric resonances in a nanowire mechanical system with nanomanipulation inside a scanning electron microscope," *Physical Review B*, Vol.66, 2002.
 - 1] K. L. Turner, S. A. Miller, P. G. Hartwell, N. C. MacDonald, S. H. Strogatz, "Five parametric resonances in a microelectromechanical system," *Nature*, Vol. 396, p.149-152, 1998.
 - 1] H. Schenk, P. Dürr, D. Kunze, H. Lakner, H. Kück, "A resonantly excited 2D micro-scanning-mirror with large deflection," *Sensors and Actuators A*, Vol. 89, p.104-111, 2001.
 - 1] H. Urey, C. Kan, W. O. Davis, "Vibration Mode Frequency Formulas for Microscanners," in preparation.
 - 1] J. Chen, S. Kang, "Dynamic macromodeling of MEMS mirror devices," *International Electron Device Meeting, Proc. IEEE*, p.41.5.1-41.5.4, Washington DC, USA, 2001.
 - 1] W. C. Young, R. G. Budynas, *Roark's formulas for stress and strain*, 7th Ed., McGraw Hill, New York, 2002.
 - 1] T. Sandner, T. Klose1, A. Wolter, H. Schenk, H. Lakner, W. Davis, "Damping Analysis and Measurement for a Comb-Drive Scanning Mirror," *Proc. of SPIE Photonics Europe Conf.*, vol., pp., 2004.
 - 1] C. Ataman, "Design, Modeling and Characterization of MEMS microscanners," M.Sc. thesis presented to Koc University, Faculty of Engineering, İstanbul, 2004.
 - 1] A. H. Nayfeh, D. T. Mook, *Nonlinear Vibrations*, Jon Wiley and Sons, New York, 1995.
 - 1] J.S. Rao, *Advanced Theory of Vibration*. Jon Wiles and Sons, New York, 1992.
 - 1] R. H. Rand, *Lecture Notes on Nonlinear Vibrations*. Version 34a, Available online at <http://www.tam.cornell.edu/randdocs>, 2000.



Caglar Ataman received his BS degree in 2002 from Bilkent University, Ankara, Turkey, in electrical engineering. Same year, he joined the Optical Microsystems Laboratory of Koç University, İstanbul, Turkey as a graduate research and teaching assistant and received his MS degree in 2004. He is currently a Ph.D. candidate in the same institute.

Caglar Ataman is a student member of SPIE.



Hakan Urey received the BS degree from Middle East Technical University, Ankara, Turkey in 1992, and MS and Ph.D. degrees from Georgia Institute of Technology, Atlanta, Georgia, USA in 1996 and in 1997, all in electrical engineering.

He is currently an Assistant Professor at Koç University, İstanbul, Turkey. Prior to that he worked for Bilkent University-Ankara and Georgia Tech Research Institute-Atlanta as a graduate research assistant, and Call/Recall Inc.-San Diego, as a co-op student. He joined Microvision Inc.-Seattle in 1998. Since 2002, he has been with Koç

University. He has published more than 40 journal and conference papers, 3 edited books, 2 book chapters, and he has 4 issued and several pending patents. He is the chair of Photonics West MOEMS Display and Imaging Systems Conference and Photonics Europe Symposium MEMS, MOEMS, and Micromachining Conference. His research interests are generally in the area of information optics and microsystems, including micro-optics, optical system design, micro-electro-mechanical systems (MEMS), and display and imaging systems.

Dr. Urey is a member of SPIE and OSA, IEEE-LEOS, and vice-president of the Turkey chapter of IEEE-LEOS.

Nonlinear Frequency Response of Comb-Driven Microscanners

Caglar Ataman, Hakan Urey

Optical Microsystems Laboratory, Department of Electrical Engineering, Koc University
Rumeli Feneri Yolu, 34450, Sariyer, Istanbul, TURKEY
Phone: +90-212-338-1474, E-mail: cataman@ku.edu.tr, hurey@ku.edu.tr

ABSTRACT

Accurate prediction of the dynamic behavior of comb-driven MEMS microscanners is important to optimize the actuator and structure design. In this paper, a numerical and an analytical model for the dynamic analysis of comb-driven microscanners under different excitation schemes are presented. The numerical model is based on a second order nonlinear differential equation. Due to the nature of the torque function, this governing equation of motion is a parametric nonlinear ODE, which exhibits hysteretic frequency domain behavior and subharmonic oscillations. Experimental results and approximate analytical expressions for this nonlinear torque function of the comb-drive are presented. Amplitude and phase relationship between the excitation signal and the resultant oscillations at different excitation frequencies are measured and we show that they are in close agreement with the numerical simulations. Analytical model uses perturbation methods to reach approximate close-form expressions for the dynamic behavior of the device in the first parametric resonance region. It is also utilized to predict the stability regions on the frequency-excitation voltage plane, where the device exhibit hysterical characteristics. Analytical and numerical modeling approaches proposed in this paper provides a simple yet powerful way to analyze the nonlinear frequency response of comb-driven actuators and simplify the design process for a microscanner based system.

Keywords: Comb-drive actuation, microscanner, subharmonic oscillation, parametric resonance

1. INTRODUCTION

Comb-driven electrostatic actuation is widely used in various microstructures. Comb structures greatly enhance the net capacitance variation and therefore, high actuation forces can be reached with relatively low drive voltages¹. Some applications that utilize comb-drive structures include microscanner^{2,3}, mechanical filters^{4,5}, and optical switches^{6,7}.

In-plane motion of a comb drive is governed by a second order constant-coefficient differential equation. The resulting system is a Simple Harmonic Oscillator (SHO). In torsional mode, the motion is out-of-plane. Actuation force is a nonlinear function of angular displacement and time. Therefore, the governing second order differential equation (DE) is no longer a constant coefficient linear DE, but a nonlinear DE with time-varying coefficients. Time varying coefficients in the governing equation lead to time dependant torsional stiffness, and the governing DE defines a parametric system that exhibits hysterical frequency response, generates subharmonic oscillations and has multiple orders of parametric resonances. Parametric oscillation is not a rare phenomenon in engineering, and is investigated in great detail, elsewhere^{8,9}. Turner developed analytical formulas for a comb-driven resonator used for scanning tunneling microscopy^{10,11}, but this is the first time that such an analysis is carried out for a microscanner. We also developed accurate numerical simulations to study the parametric resonances for arbitrary excitation waveforms.

We first discuss the structure and the typical frequency characteristics of the comb-driven microscanners used in this study. The remainder of the paper has three parts where we present our results. In section 3, we propose a numerical model for the device and compare the simulation results with experimental data. In section 4, an analytical solution of the equation of motion near the first parametric resonance is presented. Section 5 presents further experimental data on the frequency response of the device for different excitation waveforms. The last section gives an insight for future work in this area.

2. DEVICE STRUCTURE AND DYNAMIC CHARACTERISTICS

The device that we have investigated in this work is a 1D, single-crystalline silicon comb-actuated microscanner. The structure is consisted of a movable, aluminum covered mirror, a fixed frame and two flexure beams that bind the mirror to the frame. The flexures act as torsional springs that pull the mirror back to its rest position. The mirror is 2mm long, 2mm wide and 30 μ m thick. The flexure dimensions are 550 μ m in length, 10 μ m in width and 30 μ m in thickness. Both the comb fingers and the gap between the comb fingers are 5 μ m wide. Comb fingers are placed on both sides of the mirror. Mirror and the frame are electrostatically isolated with isolation trenches, so that different potentials can be applied to the fixed and movable comb fingers. The device was fabricated by Fraunhofer Institute for Photonic Microsystems (IPMS), in Dresden-Germany. More information on the design and fabrication of the device can be found in the related works by Fraunhofer IPMS^{2,12,13}. Simple sketch of the device and micrograph of the comb fingers are shown below.

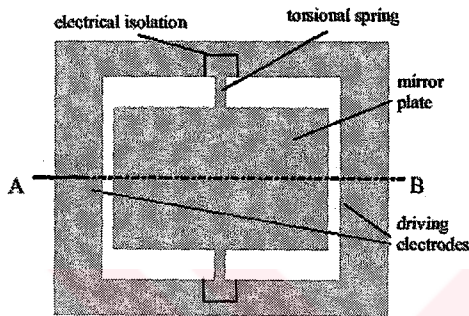


Figure 1: General Device Layout¹²

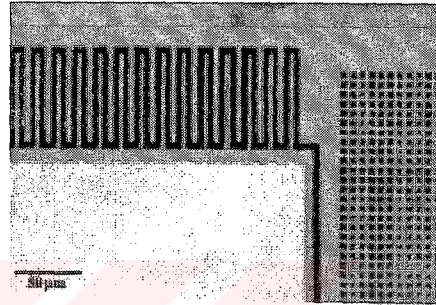


Figure 2: Micrograph of the comb fingers¹²

Biaxial microscanners that produce a 2-D raster pattern with comb-drive actuation are also available. In 2D mirror structure, there is a reflective mirror in the middle, a movable inner frame and a fixed outer frame. Innermost mirror and the movable frame have comb-drives in perpendicular orientation; therefore, the device can manage 2D scanning. Since the actuation mechanism is exactly the same, dynamic characteristics of 1D and 2D scanners are the same. Figure 1 shows the frequency response curves for horizontal and vertical axis of a 2D microscanner. The shape of the response curve is typical for all similar devices. Frequency response is nonlinear and shows hysterical behavior. The path traced on the θ - f curve when frequency is increased quasi-statically from a lower frequency is different than the case, in which the frequency is swept down from a higher frequency.

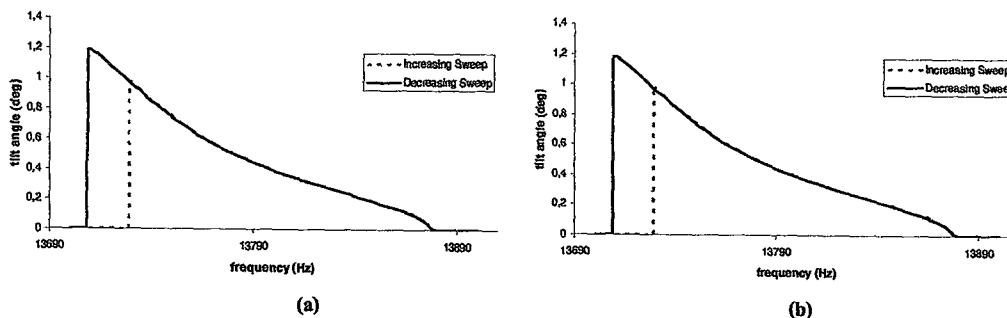


Figure 3: Frequency response of a) vertical, b) horizontal axis of a 2D comb-driven microstructure

3. SYSTEM MODELING AND NUMERICAL ANALYSIS

Comb-actuated micromirror devices exhibit a hysterical behavior and generate subharmonic oscillations. Such phenomena are typical for nonlinear parametric systems. In order to have a parametric equation of motion for our microscanner, electrical or torsional stiffness of the device should be time dependant. It is known that the general equation of motion for a microscanner can be written as follows¹⁴:

$$I_m \frac{d^2\theta}{dt^2} + b \frac{d\theta}{dt} + K_f \theta = M(\theta) \quad (1)$$

where,

I_m : Mass moment of inertia;
 b : Damping constant;
 K_f : Torsional stiffness;
 $M(\theta)$: Torque function.

Amount of torque produced by the comb actuators as a function of the tilt angle is given as:

$$M(\theta) = 2N \frac{1}{2} \frac{dC}{d\theta} V(t)^2 \quad (2)$$

where, N is the number of fingers on one side of the mirror. $M(\theta)$ is proportional to the rate of change of the energy stored in the actuator combs with respect to θ . Change in the stored energy is proportional to the change in the total capacitance of the comb actuators, which is proportional to the overlap area of comb fingers. Overlap area between the finger plates is a piecewise continuous function with three different regions. This also leads, when the fringing effects are ignored, to a piecewise continuous torque function. If the comb fingers on different frames are designed to be coplanar without any vertical offset in between and have the same thickness, the forcing function becomes an even function. If the structure were perfectly symmetrical, oscillations would not start, but there is always some asymmetry due to processing and even small force is sufficient to get the oscillations started. When fringing fields are ignored, the rate of change of total capacitance with tilt angle can be found by expressing the overlap area of the comb fingers as a function of θ . The resultant function is piecewise and can be expressed as:

Case I (when $\theta < \frac{t_m}{\frac{D}{2} + f_l}$)

$$\frac{dC}{d\theta} = -\frac{3\varepsilon}{2g} \left(\frac{D}{2} + f_l \right)^2 \theta^2 + \frac{2\varepsilon}{g} t_m \left(\frac{D}{2} + f_l \right) \theta + \frac{\varepsilon}{g} \left(\frac{x_0^2}{2} - \left(\frac{D}{2} + f_l \right) x_0 - \frac{t_m^2}{2} \right) - \varepsilon \frac{\left(\frac{D}{2} + f_l \right)}{(f_l - x_0)} f_d \quad (3a)$$

Case II (When $\frac{t_m}{\frac{D}{2} + f_l} < \theta < \frac{t_m}{\frac{D}{2} + f_l - x_0}$)

$$\frac{dC}{d\theta} = \frac{\varepsilon}{2g} x_0 \left(\frac{D}{2} + f_l - x_0 \right) - \frac{\varepsilon t_m^2}{2g\theta} \quad (3b)$$

Case III (When $\theta > \frac{t_m}{\frac{D}{2} + f_l - x_0}$)

$$\frac{dC}{d\theta} = 0 \quad (3c)$$

where,

- D : Mirror Width
- f_i : Finger Length
- g : Gap Between Fingers
- t_m : Thickness of the mirror
- x_0 : Initial Overlap of the Fingers
- f_d : Width of the Fingers

When $V(t)$ is a periodic function, such as a sinusoid, the torque turns out to be a function of both time and angular displacement. Therefore, Eq.1 becomes a nonlinear differential equation with time-varying coefficients. This implies that the resultant system is a parametric oscillator and will exhibit parametric resonances, and subharmonic oscillations.

Numerical simulations are performed using the model above and Matlab[®] ODE solvers. Figure 3 shows that the behavior of the device when the input frequency is steadily increased or decreased is significantly different. Between the two jump frequencies, there are two stable solutions, and it is the initial conditions that determine which one is the actual solution that the oscillations will converge to. Therefore, for the regions, in which the nonlinear differential equation has two solutions, the simulation converges to the one with lower oscillation amplitude. For decreasing sweep simulations, the initial condition is larger than the maximum scan angle, and the simulation converged to the solution with larger oscillation amplitude.

Figure 4 illustrates the excitation and scan waveforms. A photodetector is placed at the center of the scan line and produces a short pulse each time the scanner goes through zero deflection angle. The square excitation waveform is at 2234Hz and the zero crossings of the sinusoidal scan waveform are also at the same frequency. Since two peaks of the diode output correspond to one complete oscillation period, the scan waveform frequency is 1117Hz, half of the excitation frequency. Figure 4.b shows the sinusoidal scan waveform and the square wave excitation waveform, illustrating the subharmonic nature of the oscillations.

Figure 5 shows the simulation results for nonlinear frequency response characteristics and compares them with the experimental data. The graph is plotted for downsweep frequency response and three parametric resonances were captured. Numerical method successfully predicts the higher order parametric resonances and their associated jump frequencies. Numerical model is not as accurate in predicting the maximum scan amplitude. This is due to neglecting the fringing fields for the electrostatic torque calculations.

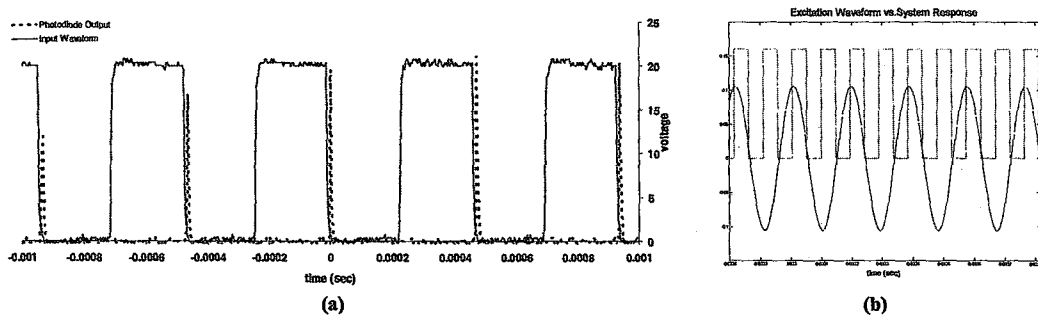


Figure 4: (a) Square wave excitation waveform (solid line) and photodiode output (dashed line) at the center of the scan line; (b) simulation result illustrating the sinusoidal scan waveform and the square excitation waveform

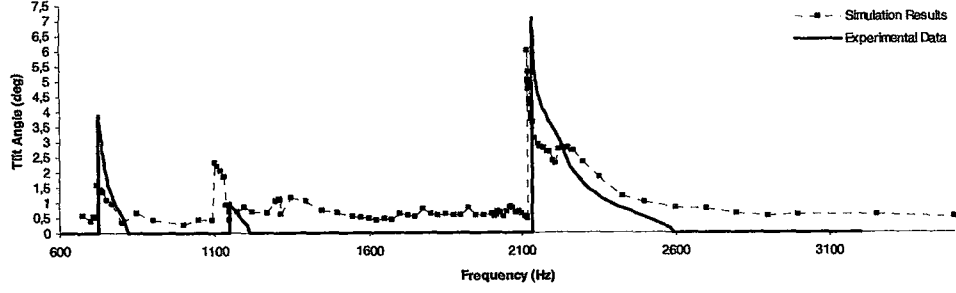


Figure 5: Comparison of the simulation and experimental results for the downsweep frequency response characteristics of the device for 20V square wave excitation (shown in Figure 4.a)

4. ANALYTICAL SOLUTION FOR 1ST ORDER PARAMETRIC RESONANCE

A general solution for the equation of motion of the microscanner is difficult to achieve. On the other hand, some reasonable assumptions can be made, in order to get some analytical expressions that will reveal some crucial characteristics of the solution. Assume that the input voltage waveform is the square root of a biased sinusoid function (this way, we can eliminate higher harmonics in the $V(t)^2$ term in Eq.2). In case of small amplitude oscillations, the torque function in Eq.3 can be simplified as:

$$M(\theta, t) = -(r_3\theta^3 + r_1\theta)A^2(\cos(\omega t) + 1) \quad (4)$$

In the above formula, rate of change of total capacitance is approximated with a third order polynomial. The torque function is odd; therefore no even order terms exist. Near the first parametric resonance, oscillation frequency is half of the drive frequency. Using this fact, and the simplified torque expression of Eq.4, Eq.3 can be rewritten for the first parametric resonance region as follows¹⁰:

$$\frac{d^2\theta}{d\tau^2} + \alpha \frac{d\theta}{d\tau} + (\beta + 2\delta \cos(2\tau))\theta + (\delta_3 + \delta_3 \cos(2\tau))\theta^3 = 0 \quad (5)$$

where,

$$\tau = \frac{\omega t}{2}, \quad \alpha = \frac{2b}{\omega I_m}, \quad \beta = 4 \frac{(r_1 A^2 + K_f)}{\omega^2 I_m}, \quad \delta = \frac{2r_1 A^2}{\omega^2 I_m}, \quad \delta_3 = 4 \frac{r_3 A^2}{\omega^2 I_m}$$

If the damping is small in the system, only β is in the order of 1, whereas the other terms are at least one order of magnitude smaller than β . Therefore, perturbation methods may be utilized in the solution of Eq. 5. If we define the perturbation parameter ϵ as equal to δ , Eq.5 becomes a perturbed Mathieu equation and it can be solved using method of two-variable expansion⁹. This method is based on the fact that possible solution of Eq. 5 includes two different time-scales. One of those time scales is close to τ and defines the period of the motion. The other time scale, on the other hand, is much slower and modulates the amplitude of the oscillations¹⁰. If the time scales are defined as τ and $\eta = \epsilon t$, and we assume that $\theta = \theta_0 + \epsilon \theta_1$, $\beta = 1 + \delta \beta_1$, the solution of Eq.5 is given as follows:

$$\theta = A(\tau) \cos\left(\frac{1}{2}\xi\right) + B(\tau) \cos\left(\frac{1}{2}\xi\right) \quad (6)$$

where A and B are given as the solution of following coupled differential equations:

$$\frac{dA}{d\tau} = -\frac{\mu}{2}B + \frac{B}{2}(\beta_1 - 1) + \frac{B\delta_3}{8\epsilon}(3A^2 + B^2) \quad (7a)$$

$$\frac{dB}{d\tau} = -\frac{\mu}{2}A - \frac{A}{2}(\beta_1 + 1) - \frac{A\delta_3}{8\epsilon}(5A^2 + B^2) \quad (7b)$$

Limits of the bistable region on the β - δ and the map of this region on the voltage-frequency plane are shown in Figure 6. On figure 6a, the frequency range between the arms of the plot at a certain voltage corresponds to the frequency range the stability region; however, the deviation from the model in higher voltage values is evident. This is because that for at atmospheric pressure, the damping term in Eq.5 is not small enough to be assumed as a perturbation in the system. In vacuum environment, the model is predicted to give much accurate results. Vacuum measurements will be performed as future work.

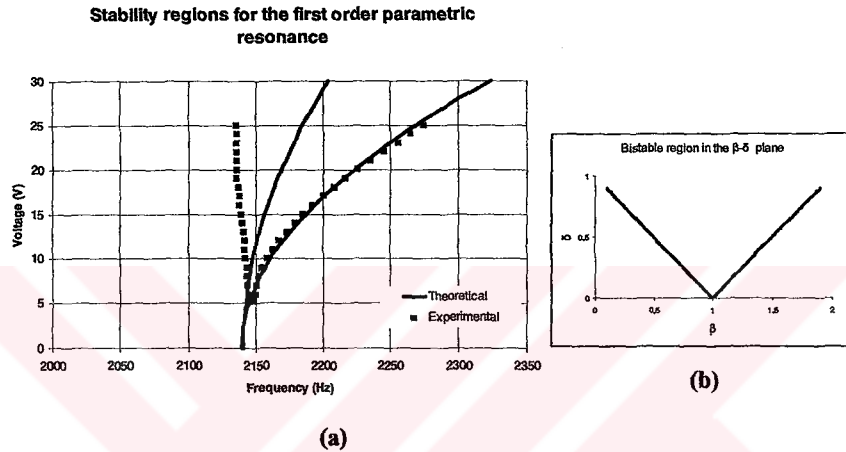
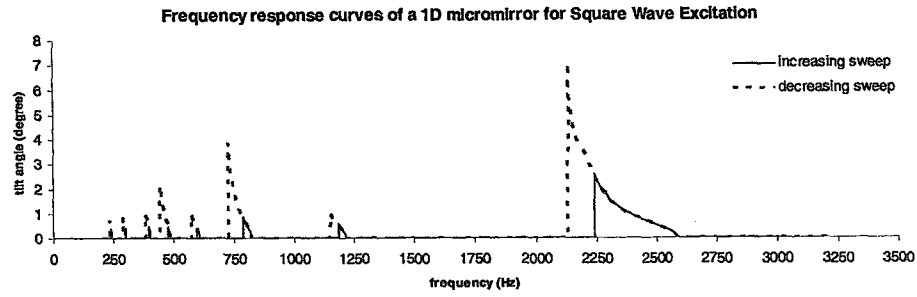


Figure 6: Analytical and experimental results for the stability region a) on the voltage-frequency plane, b) on the β - δ plane. Theoretical plots are drawn assuming that there is no damping in the system. However actual device is operated in the atmospheric pressure and significant damping is present in the system. Therefore, the tip of the stability curve is lifted upwards and the curve is widened considerably.

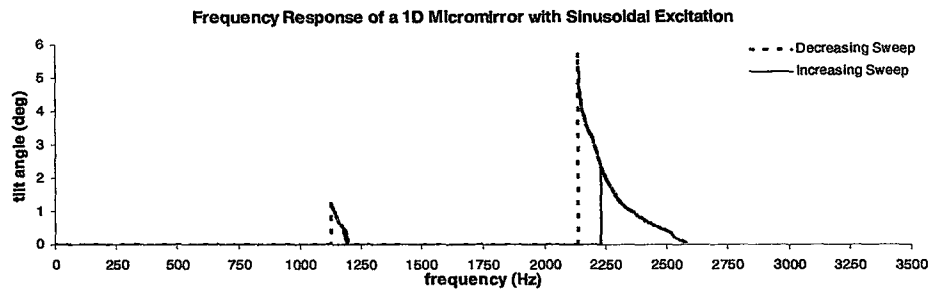
The theoretical plots assume that there is no damping in the system; therefore the minimum points are on the x-axis. However, the experimental data are taken in atmospheric pressure and there is significant air damping in the system (Q factor of the system is only 22). Damping lifts the tongue upwards and smoothes the tip of the stability curve. Analytically, the tip of the curve is found to be at 2242 Hz. The actual value is 2248 Hz, which is in close agreement with the analytical result.

5. HIGHER ORDER PARAMETRIC RESONANCES

In addition to the first order parametric resonance that we have analyzed so far, parametric systems have more resonances located near $2f_r/n$, where f_r is the mechanical resonance frequency of the system, and n is any positive integer greater than one. As shown in the analytical analysis, as the damping in the system is increased, the threshold voltage required for observing the parametric resonances rises. Due to damping, it is difficult to observe higher order parametric resonances at atmospheric pressure for most MEMS devices. However, the device in this work gives rise to higher order parametric resonances even at atmospheric pressure. Figure 7 shows the experimental frequency response curves for the microscanner with both square and sinusoidal excitation. With square wave excitation, it is possible to observe 8 different orders of parametric resonances, whereas with sinusoidal excitation, number of observable parametric resonances is only two.



(a)



(b)

Figure 7: Higher order parametric resonances a) with 20V square wave input, b) 20V sine wave input

For square wave input, the response is not a pure sinusoid for high order resonances. Scan wave shows an unusual behavior and changes oscillation frequency and amplitude at each half cycle of the square wave. When excitation is in the OFF state (meaning that force is not present in the system), the system makes free oscillation at its natural resonant frequency, when the excitation is in the ON state, the mirror oscillates at a higher frequency, which can be calculated using the excitation and natural frequencies. Figure 8 shows the experimental results illustrating this behavior. Such behavior is observed in very high order resonances. In Figure 9 simulated waveforms for varying frequency behavior can be seen.

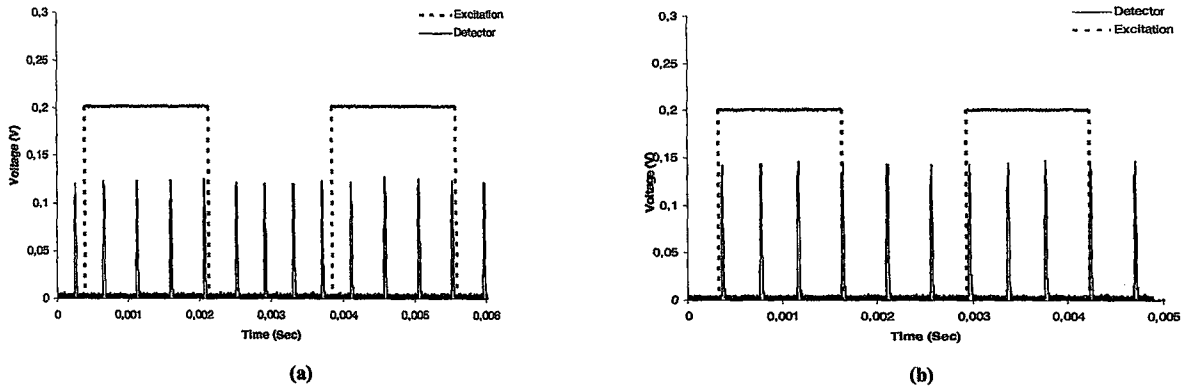


Figure 8: Varying frequency oscillations (a) At 7th order parametric resonance and 289 Hz, (b) At 6th order parametric resonance and 384 Hz.

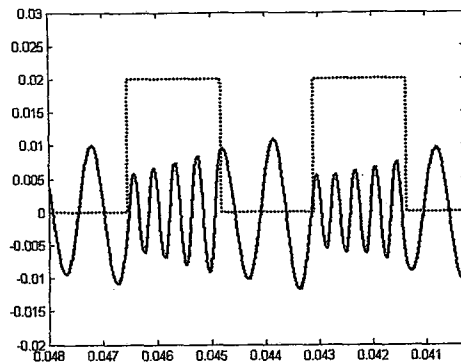


Figure 9: Simulation results for the varying frequency behavior. The simulation was done at 380 Hz, for 20V square wave input.

6. DISCUSSION AND FUTURE WORK

We have presented an analytical and a numerical model for a comb-driven microscanner. The numerical model can be utilized up to 20 degrees of angular displacement (the limit is the validity of small angle approximation) and predicts higher order parametric resonances, as well as the fundamental resonance. The significance of the model is within its ability to simulate high deflection angles, which are common in display and scanning applications. The analytical model is valid for a simplified excitation waveform, small angular displacements, and negligible damping. Analysis in this paper is done for the fundamental resonance; however similar methods can be used to reach approximate analytical solutions for higher order resonances. Analytical results will be extended to higher order resonances in future work. The analytical model cannot predict the instability region of the voltage-frequency curve very accurately. This is primarily, due to the loose satisfaction of the low damping assumption at atmospheric pressure. Vacuum testing of the devices will be carried out as a next step, in order to obtain better agreement between the analytical model and the experimental results.

ACKNOWLEDGEMENTS

We'd like to thank Dr.Wyatt Davis (Microvision Inc) and Dr.Alexander Wolter (Fraunhofer IPMS) for helpful discussions

REFERENCES

1. S. Rodgers, S. Kota, J. Hetrick, Z. Li, B. Jensen, T. Krygowski, S. Miller, S. Barnes, M. Burg, "A new class of high force, low-voltage, compliant actuation systems," Sensors & Actuators Workshop, 2000
2. H. Schenk, P. Dürr, D. Kunze, H. Lakner, H. Kück, "A resonantly excited 2D micro-scanning-mirror with large deflection," Sensors and Actuators A, Vol. 89, p.104-111 (2001).
3. P. R. Patterson, D. Hah, H. Nguyen, H. Toshiyoshi, R. Chao, M. Wu, "A scanning micromirror with angular comb-drive actuation," International Conference on Micro Electro Mechanical Systems, Proc. IEEE, p.544-547 (2002).
4. L. Lin, R. T. Howe, A. P. Pisano, "Micromechanical filters for signal processing," Journal of Microelectromechanical Systems, Vol. 7, No. 3, p.286-294 (1998).
5. C. T. C. Nguyen, "High-Q micromechanical oscillators and filters for communications," International Symposium on Circuits and Systems, Proc. IEEE, p.2825-2828 (1997).
6. J. D. Grade, K. Y. Yasumura, H. Jerman, "A DRIE comb-drive actuator with large, stable deflection range for use as an optical shutter," International Conference on Solid-State Sensors, Actuators and Microsystems, Proc. IEEE/EDS, Boston, Massachusetts, USA (2003).

7. L. Zhou, M. Last, V. Milanovic, J. M. Kahn, K. S. J. Pister, "Two-axis scanning mirror for free-space optical communication between UAVs," International Conference on Optical MEMS and Their Applications, Proc. IEEE/LEOS, p.1-2, Hawaii, USA (2003).
8. Y. Mitropolskii, N. V. Dao, "Applied Asymptotic Methods in nonlinear oscillations", Kluwe Academic Publishers, Boston (1997).
9. R. H. Rand, "Lecture Notes on Nonlinear Vibrations," Version 34a, Available online at <http://www.tam.cornell.edu/randdocs>, (2000).
10. W. Zhang, R. Baskaran, K. L. Turner, "Effect of cubic nonlinearity on auto-parametrically amplified resonant MEMS mass sensor," Sensors and Actuators A, Vol. 102, p.139-150 (2002).
11. K. L. Turner, S. A. Miller, P. G. Hartwells, N. C. MacDonald, S. H. Strogatz, "Five parametric resonances in a microelectromechanical system," Nature, Vol. 396, p.149-152 (1998).
12. H. Schenk, P. Dürr, T. Haase, D. Kunze, U. Sobe, H. Lakner, H. Kück, "Large deflection micromechanical scanning mirrors for linear scans and pattern generation," Journal of Selected Topics in Quantum Electronics, Vol. 6, No. 5, p.715-722 (2000).
13. H. Schenk, A. Wolter, H. Lakner, "Design optimization of an electrostatically driven micro scanning mirror," Conf. on MOEMS and Miniaturized Systems, Proc. SPIE, Vol. 4561, p.35-44, San Francisco, Calif., USA, (2001)
14. J. Chen, S. Kang, "Dynamic macromodeling of MEMS mirror devices," International Electron Device Meeting, Proc. IEEE, p.41.5.1-41.5.4, Washington DC, USA, (2001).



Analysis of Parametric Resonances in Comb-Driven Microscanners

Caglar Ataman, Ozgur Kaya, Hakan Urey

Optical Microsystems Laboratory, Department of Electrical Engineering, Koc University
Rumeli Feneri Yolu, 34450, Sariyer, Istanbul, TURKEY
Phone: +90-212-338-1474, E-mail: cataman@ku.edu.tr, hurey@ku.edu.tr

ABSTRACT

Dynamic behavior of a comb-driven torsional microscanner is governed by a nonlinear parametric differential equation. Theoretically, such systems have multiple resonances located near the integer fractions of twice the mechanical resonance frequency. The number of observable parametric resonances strongly depends on the damping of the system, whereas the stable and unstable operating regions are determined by drive-voltage and drive-frequency. In atmospheric pressure, only first few of these parametric resonances are observable within the operation voltage range of the devices. This paper explores the effect of damping on the various characteristics of parametric resonances and some unusual scanner behavior rarely seen in mechanical structures. A numerical and an analytical model for comb-driven microscanners are presented. Frequency responses of various devices are experimentally measured inside a vacuum chamber at different ambient pressures ranging from atmospheric pressure to 30 mTorr. Experimental results are compared with analytical and simulation results.

Keywords: Comb-drive actuation, microscanner, subharmonic oscillation, parametric resonance, damping, quality factor

1. INTRODUCTION

Electrostatic comb-drive actuation is a common actuation mechanism in microelectromechanical systems (MEMS). Comb-drives can be actuated in in-plane or out-of plane modes, and operation mode of the actuator is the fundamental factor that determines the dynamic behavior of the associated device. In-plane mode comb-actuators are widely utilized in various devices and systems such as tunable capacitors¹, mechanical resonators², optical switches³, and mechanical filters for RF and other applications.^{4, 5} In this mode of operation, the force induced by the actuator is independent of the displacement of the combs, and the actuator exhibits a simple harmonic oscillatory (SHO) behavior. As all other second order harmonic oscillator, in-plane mode comb actuators have one resonance, corresponding to the mechanical resonance of the system. On the other hand, the force in out-of-plane actuator is both time and displacement dependent. This relatively complicated nature of the forcing function leads to the phenomenon of parametric resonance. Parametric systems are seen in different areas of science and engineering, such as photonic crystals⁶, optical cavities⁷, plate vibrations⁸, and quantum devices.⁹ A parametric oscillator is described with a second order differential equation with time-dependant coefficients. In parametric systems, linear relation between the drive signals and the output of the system ceases to exist and the system exhibits subharmonic oscillations and hysterical frequency response.

We have previously proved that a comb-driven torsional microscanner is a typical parametric oscillator and presented experimental results, numerical model, and analytical solutions for the primary resonance (fundamental parametric resonance).¹⁰ This paper explores the effect of damping and drive voltage on the number and width of the stability curves of the microscanners. We applied "method of strained parameters" to obtain stability regions in the analytical solution, and we applied "Floquet Theory" to obtain our approximate transient analytical solutions. Our analytical solutions successfully predict stability regions and other characteristics of primary and higher order resonances. In section II, we give a brief introduction to the microscanner structure. Section III includes the analytical analysis of the stability regions and steady state solutions for the parametric resonance. Experimental frequency response and stability data are also given in section III. Comparisons of this data with analytical and numerical results are also included in this section. In the last part, we included conclusions and a brief discussion on the significance of this work.

2. THE DEVICE

2.1 Device Layout

The device that is investigated in this work is a 1D, 30 μm thick single-crystalline silicon comb-actuated microscanner. The structure consists of a movable, aluminum covered 2 mm x 2mm aluminum mirror, a fixed frame and two flexure beams that bind the mirror to the frame. The flexures are 550 μm in length, 30 μm in width, 20 μm in thickness, and they act as torsional springs that pull the mirror back to its rest position. The mirror and the frame are electrically isolated via the isolation trenches. Therefore, different potentials can be applied to the complementary comb fingers. These fingers are placed on sidewalls of the mirror. The devices were fabricated by Fraunhofer Institute for Photonic Microsystems (IPMS), in Dresden-Germany. More information on the design and fabrication of these devices can be found in the related works by Fraunhofer IPMS^{11, 12, 13}. Figure 1 shows the general micromirror layout.

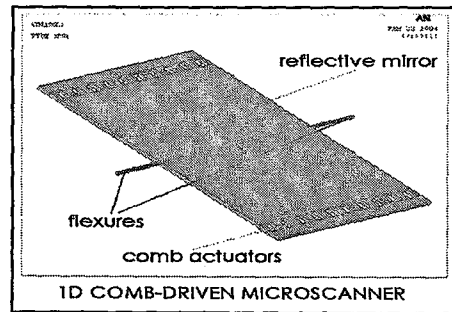


Figure 1 - General layout of the microscanner

2.2 Actuation Mechanism

Torsional movement of these micromirrors is induced by the numerous comb shaped fingers on the edge of the device. These fingers greatly enhance the overlap capacitance between the opposing surfaces and lower the operation voltage of an electrostatic actuator significantly. Figure 2 shows the comb fingers on the microscanner and a first order approximation to capacitance-change – tilt-angle characteristics of the comb actuator.

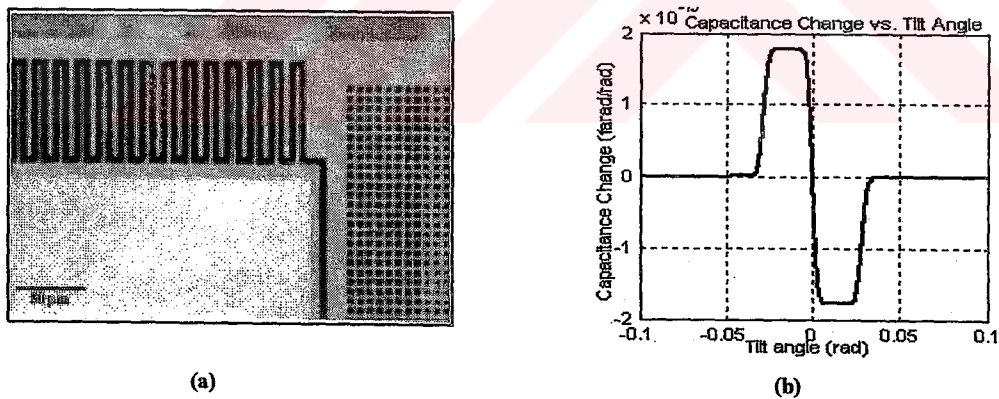


Figure 2 - (a) The comb fingers on the edge of the microscanner mirror. (b) Torque vs. tilt angle characteristic

The amount of torque produced by the comb-drive actuators is given by the expression,

$$M(\theta) = 2N \frac{1}{2} \frac{dC}{d\theta} V(t)^2 \quad (1)$$

where, N is the number of comb fingers. The nonlinear relation between the rate of change of capacitance and the tilt angle is showed in Figure 2(b). In electrostatic actuators, the amount of torque produced is proportional to the square of

the input signal. Therefore, when a time-varying input is applied to the system, the torque function is both time and displacement dependant. We have previously shown that this nature of the torque function leads to parametric oscillations, and comb-drive microscanners exhibit the typical characteristics of parametric systems. Figure 3 shows the frequency response of the device within the first parametric resonance.

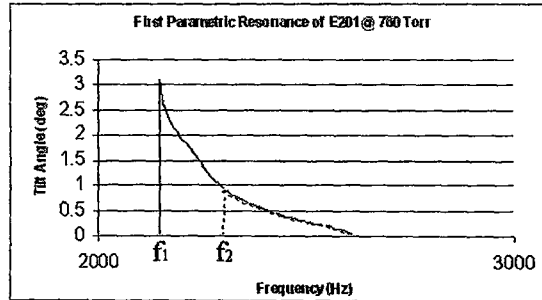


Figure 3 - Frequency response curve of the device in the fundamental parametric resonance. The peak amplitude corresponds to $f \approx 2f_b$, where f_b is the mechanical resonance frequency of the system.

The shape of the response curve is typical for all similar devices. Frequency Response of the torsional comb-driven microscanners is a nonlinear function exhibiting subharmonic oscillations and hysterical behavior. The path traced on the θ - f curve when frequency is increased quasi-statically from a lower frequency is different than the case, in which the frequency is swept down from a higher frequency. The interval between the two jump frequencies f_1 and f_2 is the *unstable region* of the response curve. Oscillations in this region can only be observed if the external frequency is quasi-statically swept down to this region from a higher initial value. At the critical frequencies, the jump in the oscillation amplitude is extremely abrupt – sharper than 10^{-3} Hz, which is the maximum resolution of our measurements. It is uncommon for a macroscopic parametric system to have multiple observable parametric resonances. But we are able observe more than one resonance even in the atmospheric pressure. In vacuum, the number of observable resonances is much higher. The shape of the other orders of resonance is still the same, but they are located around $2f_0/n$, $n=1,2,\dots$. In the first parametric resonance, the oscillation frequency is half the driving signal frequency. This phenomenon is called *subharmonic oscillation*. Subharmonic oscillations in comb-driven microscanners are explored in our earlier work.¹⁰

3. THEORY, EXPERIMENTS AND SIMULATIONS

General equation of motion for a microscanner can be written as follows¹⁸:

$$I_m \frac{d^2\theta}{dt^2} + b \frac{d\theta}{dt} + K_f \theta = M(\theta) \quad (2)$$

where,

- I_m : Mass moment of inertia;
- b : Damping constant;
- K_f : Torsional stiffness;
- $M(\theta)$: Torque function.

For very small tilt angles, the torque function of the comb actuators can be successfully approximated by a 3rd order odd polynomial. With a square-rooted-sine input voltage ($V = A\sqrt{\cos(\omega t) + 1}$), the torque expression is;

$$M(\theta, t) = -(r_3\theta^3 + r_1\theta)A^2(\cos(\omega t) + 1) \quad (3)$$

We can now rewrite Eq.2 as follows:

$$\frac{d^2\theta}{d\tau^2} + \alpha \frac{d\theta}{d\tau} + (\beta + 2\delta \cos(2\tau))\theta + (\delta_3 + \delta_3 \cos(2\tau))\theta^3 = 0 \quad (4)$$

where,

$$\tau = \frac{wt}{2}, \quad \alpha = \frac{2b}{wI_m}, \quad \beta = 4 \frac{(r_1 A^2 + K_f)}{w^2 I_m}, \quad \delta = \frac{2r_1 A^2}{w^2 I_m}, \quad \delta_3 = 4 \frac{r_3 A^2}{w^2 I_m}$$

In this new representation τ stands for the new time variable, which is the actual time scaled by $w/2$. Eq.4 is a nonlinear homogeneous Mathieu equation and there exists two linearly independent solutions for this equation. We have previously presented approximate analytical expressions for the behavior of this system near first parametric resonance.¹⁰ A more general insight for the transient behavior of the system may be gained by using Floquet theory. In order to utilize this theory, we need to express Eq.4 in state space representations, as follows:

$$\begin{aligned} \dot{x}_1 &= x_2 \\ \dot{x}_2 &= -\alpha x_2 - (\beta + 2\delta \cos(2\tau))x_1 - (\delta_3 + \delta_3 \cos(2\tau))x_1^3 \end{aligned} \quad (5)$$

An analytical solution can be obtained when the cubic nonlinearity and the damping terms are ignored. We can now, rewrite this system of equations in matrix form as:¹⁶

$$\begin{bmatrix} \dot{x}_1 \\ \dot{x}_2 \end{bmatrix} = \begin{bmatrix} 0 & 1 \\ -f(\tau) & 0 \end{bmatrix} \begin{bmatrix} x_1 \\ x_2 \end{bmatrix} \quad (6)$$

Where, $f(t) = \beta + 2\delta \cos(\tau)$. Linear system theory suggests that this system of equations has two linearly independent solutions. Let $X(t)$ be a fundamental solution matrix, whose columns are two linearly independent solutions of Eq.6, and satisfy the initial conditions $X(0)=I$, where I is the identity matrix. Floquet theory suggests that the characteristic matrix C of Eq.6 is given by the relation,¹⁴

$$C = X(T) = \begin{bmatrix} x_1(T) & \dot{x}_1(T) \\ x_2(T) & \dot{x}_2(T) \end{bmatrix} \quad (7)$$

Where, T is the period of $f(\tau)$, and equals to 2π for the Mathieu equation. The transient solutions and the stability of the system in Eq.3 can be determined using the characteristics matrix. Let $\theta_{1,2}(t)$ denote the transient solutions of the system of interest; then they are given by the relation.¹⁴

$$\begin{aligned} \theta_1(\tau) &= e^{\gamma_1 \tau} \phi_1(\tau) \\ \theta_2(\tau) &= e^{\gamma_2 \tau} \phi_2(\tau) \end{aligned} \quad (8)$$

where, γ_i are called the characteristic exponents of the equation. Above expression is the general form of the solution for linear Mathieu equation. In torsional comb microscanner case, the periodic functions of $\phi_i(\tau)$ are linear combinations of sinusoidal functions of period π and 2π . γ_i are given by the expression,

$$\gamma_i = \frac{1}{T} \ln(\lambda_i) \quad (9)$$

Where, λ_i are the eigenvectors of the characteristic matrix C . For a linear Mathieu equation, the product of these eigenvectors is unity. Depending on the values of these eigenvectors, steady state and stability characteristics of the system can be determined. If these eigenvectors are complex conjugates, they have unity modulus and therefore they lie on the unit circle. In this case, the steady state output is bounded and the system is stable. However, the amplitude of the output has a damped oscillatory behavior, due to Eq.8. Figure 4(a) shows the experimental data for such a behavior. The

system is within first parametric resonance range, but is far from its resonance peak. The exponential growth and damped oscillations in the output amplitude can be clearly seen from the data. When one of the eigenvectors of the characteristic matrix has amplitude greater than unity, one of the fundamental solutions die out in time, however the amplitude of the other solution grows exponentially. If there is no damping in the system, this growth in the output amplitude is unbounded, and the system becomes unstable. However, both damping and the cubic nonlinearity, -the effects that we both ignored in deriving Eq.8- have a stabilizing effect on the system, and they limit the oscillation amplitude of the unstable system. When $f_{exc}=f_1$ or $f_{exc}=f_2$, the eigenvectors of the characteristic matrix are either -1 or 1, and the oscillatory behavior in the transient response diminishes. Such a characteristic can be observed in Figure4b. Unlike linear systems, exponential terms has positive growth coefficient, and the amplitude grows until it reaches upper bound set by damping and the cubic nonlinearity. Then suddenly, oscillation amplitude stops growing.

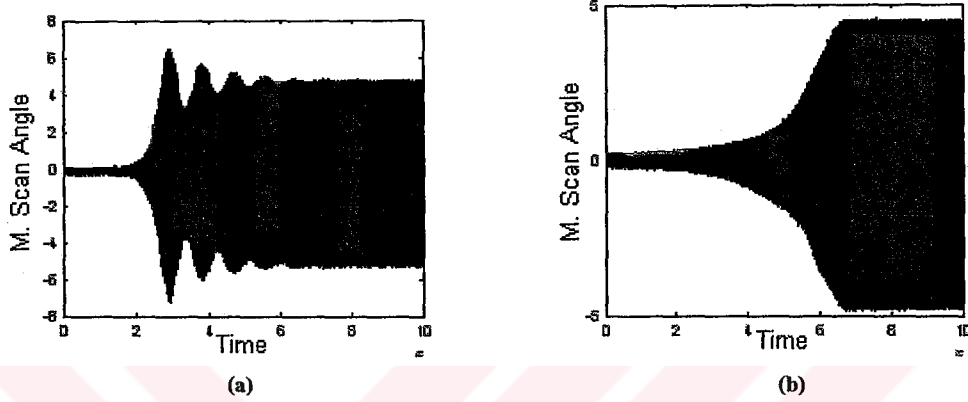


Figure 4 - Transient response of the device to various frequencies. (a) $f_{exc} > f_2$ (stable region);
(b) $f_{exc} = f_2$ (boundary of the unstable region).

3.1 Stability Tongues

According to the Floquet theory, the solutions of Eq.4 on the stability transition curves have periods of π or 2π , and these curves correspond to the positive or negative unity eigenvectors of the characteristic matrix. These stability curves form a tongue-like shape in the drive-voltage – drive-frequency space, and therefore called “stability tongues”. Due to the time scaling of Eq.4, a solution which is of period π in the new time scale correspond to an oscillation of period T in the actual time. Similarly, the 2π periodic solution of Eq.4 is actually an oscillation of period $2T$. This $2T$ periodic solution is half the frequency of the drive signal and corresponds to the subharmonic oscillation in the 1st order parametric resonance. Based on the result of Floquet theory that on boundaries of the stability tongues the solution of Eq.4 is either π or 2π periodic, we utilized the method of strained parameters, in order to find analytical expressions for determining these tongues. In this method the characteristic exponents are chosen so that the periods of the possible solutions of Eq.4 are π or 2π . Then, the required parameters are determined in such a way that this assumption holds. With the effect of small viscous damping, which is the case in comb-driven microscanners within small oscillation amplitudes, the transition curves separating the stable and unstable regions are given by¹⁴:

$$\beta = n^2 \pm \frac{1}{2} \left[(a_{1n}^2 + b_{1n}^2) \delta^2 - 16\alpha^2 n^2 \right]^{\frac{1}{2}} + O(n), \quad n=1,2,3,\dots \quad (10)$$

Where, a_{1n} and b_{1n} are the Fourier series coefficients of $f(t)$, and $O(n)$ stands for higher order terms. For the first two orders of parametric resonances, the expressions for the associated stability tongues can be found as:¹⁵

$$\beta = 1 \pm (\delta^2 - 4\alpha^2)^{\frac{1}{2}} - \frac{1}{8} \delta^2 + O(n) \quad (11a)$$

$$\beta = 4 + \frac{1}{6} \delta^2 \pm \left(\frac{1}{16} \delta^2 - 16\alpha^2 \right)^{\frac{1}{2}} + O(n) \quad (11b)$$

Figure 5 shows the experimental results and analytical approximations for the stability tongues for the observable parametric resonances at two different ambient pressure levels. The tongues are mapped in to drive-voltage – drive-frequency plane using the relations in Eq.4.

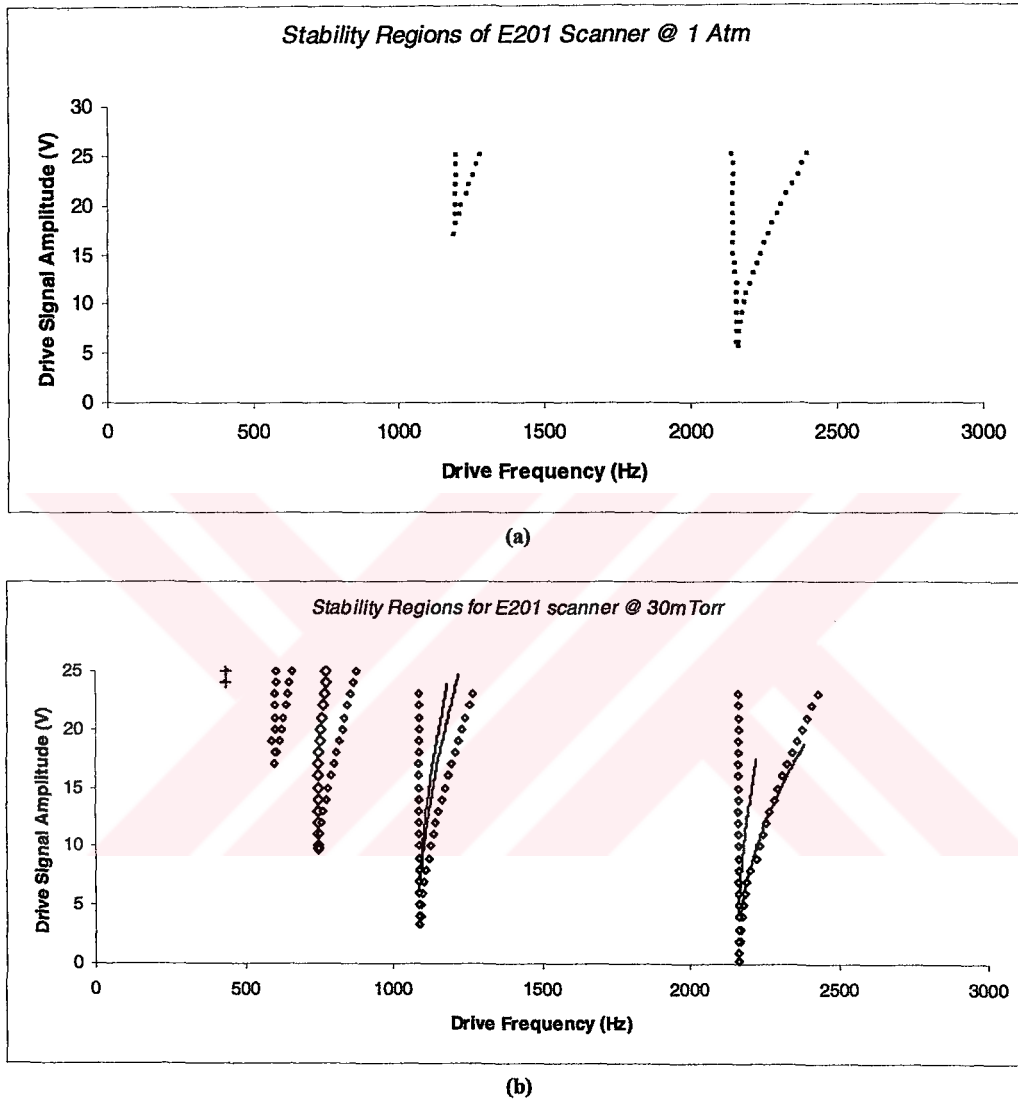


Figure 5 - Stability tongues for the device (a) At atmospheric pressure; (b) At an ambient pressure of 30 mTorr. Dotted lines show experimental results and solid lines in (b) show the stability tongues evaluated using the analytical formulas.

Figure 5(a) shows the stability tongues of the microscanner in the atmospheric pressure. There is a significant viscous air damping between the comb fingers in the atmospheric pressure (we have measured a Q factor of 22), so that there are only two observable parametric resonances within the operation voltage of the device. Additional orders or resonances would be observed with higher drive voltages, but we avoided such high voltages in order to prevent device failure. The stability tongues of the microscanner in 30 mTorr ambient pressure can be seen in Figure 5b. Voltage and frequency span of the two plots are identical. In low pressure, air damping is much less and therefore the device has a much higher quality factor (~1250). As seen in the Figure 5(b), there are 5 observable parametric resonances and the width of the stability tongues are increased, and their tips came much closer to the $V=0$ axis. In Figure 5b, solid lines represent the

results of the analytical expressions of the stability tongues. The analytical results are in good agreement with the experimental data. However, as the input voltage increases, the deviation of the analytical approximation from the experiments increases. This is due to the fact that for higher voltages, the small driving signal and small tilt angle approximations are becoming invalid and therefore our perturbation analysis ceases to be accurate. Another reason of the difference between the experimental and analytical results is the cubic nonlinearity in Eq.3. As the driving voltage increases, this cubic nonlinearity term also grows and it prevents the left hand of the stability curve to bend rightward.

3.2 Frequency Response

Damping of system also has a significant effect on the frequency response of the device. Figure 5 compares the frequency response of the comb-driven microscanner at two different ambient pressures. The solid line represents the experimental data for backward frequency sweep, and the dotted line represents forward frequency sweep. The driving signal was a square-root sine wave with peak-to-peak value of 20V.

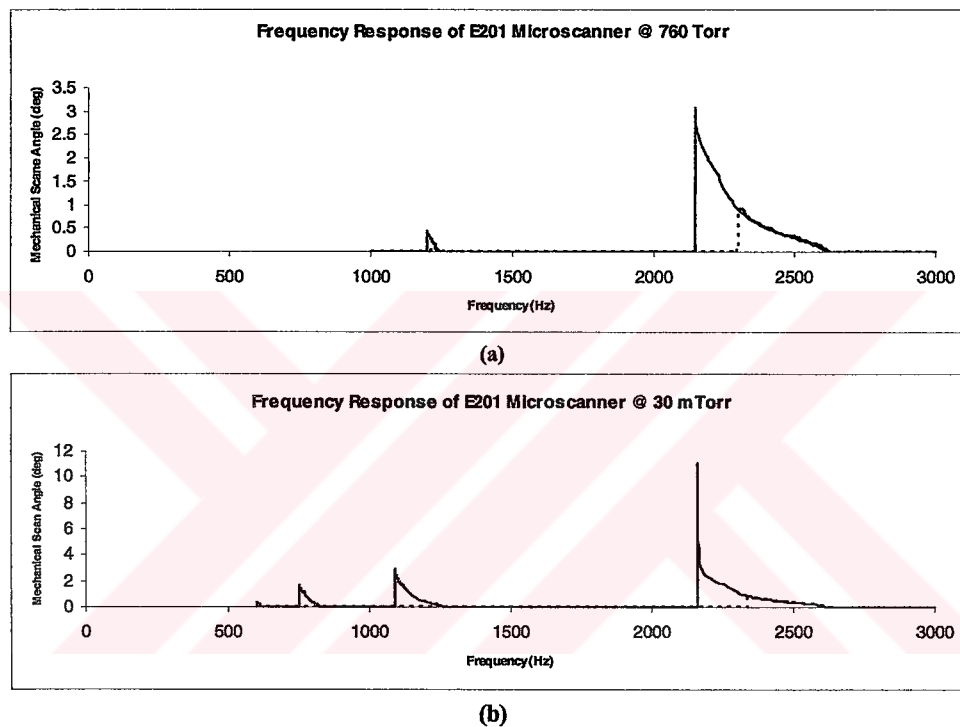


Figure 6. Frequency response of the microscanner; (a) at atmospheric pressure, (b) at 30 mTorr.

With this drive signal, we can observe two parametric resonances in the atmospheric pressure and four resonances in 30 mTorr. The amplitude of the oscillations is significantly increases in low pressure due to lower damping. Near the peak of the first parametric resonance, the oscillation amplitude reaches almost 12° . In atmospheric pressure, the maximum oscillation amplitude is around 3.5° . Another effect of the damping is the modification of the resonant frequency.¹⁴ When the pressure changed from ambient to 30 mTorr, resonance frequency of the device increased from 1068.9 Hz to 1081.7 Hz. This shift is due to the frequency tuning effect of damping.

3.3 Simulation Results

Frequency and transient response of the devices were simulated using our numerical model. The simulations are done by numerically solving Eq.2 using the differential equation solvers in MATLAB[®]. The torque associated with the comb actuators is computed using a first order approximation of the total capacitance in the system (Figure 2(b)). We have presented the detailed modeling procedure elsewhere.¹⁰ Figure 7 is presents the results of some simulations run with this model. Figure 7(a) compares the experimental data and simulation results for the frequency response of the device at atmospheric pressure. The model accurately predicts the values of frequencies, where abrupt changes in the amplitude occur. There is a slight disagreement between the amplitudes of two data sets, which is due to the ignored fringing

electric fields between the comb fingers. Figure 7(b) shows the result for a sample transient response simulation, which verifies the exponential increase and oscillatory decay in the output amplitude in this operation region observed in the experiments (see. Figure 4a). The numerical results show good agreement with the experimental data and verify the validity of the model.

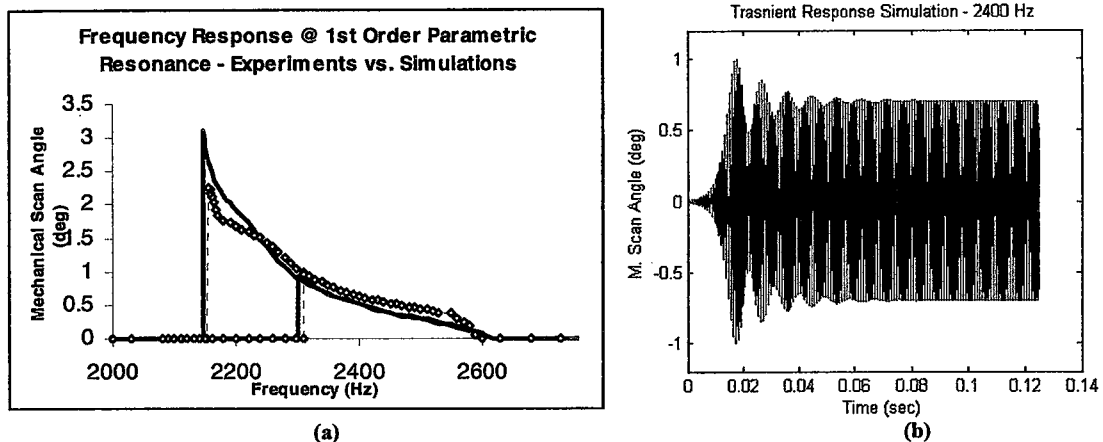


Figure 7 – Simulation results for; (a) frequency response at 1st order parametric resonance, (b) sample transient response at stable region.

3.4 Experimental Setup

The microscanner structure does not employ an angular displacement feedback feature; therefore, we have used various optical characterization methods, in order to obtain desired data. Figure 8 shows a picture of our frequency response, transient response stability analysis measurements setup. Transient response measurements are done using a fast 2D-Position Sensing Detector (PSD) and a PC with data acquisition hardware. A laser beam is sent on the microscanner, and the scan waveform of the microscanner is recorded by reflecting the scan-line onto the PSD. Response time of the PSD is much faster than the scan frequency, therefore no deformation of the scan waveform is allowed. For the frequency response and stability measurements, we used a computer-controlled setup, based on a single photodetector. A similar method is used for the damping measurements. For the low-damping experiments, the device is placed inside a vacuum chamber with a transparent bell jar.

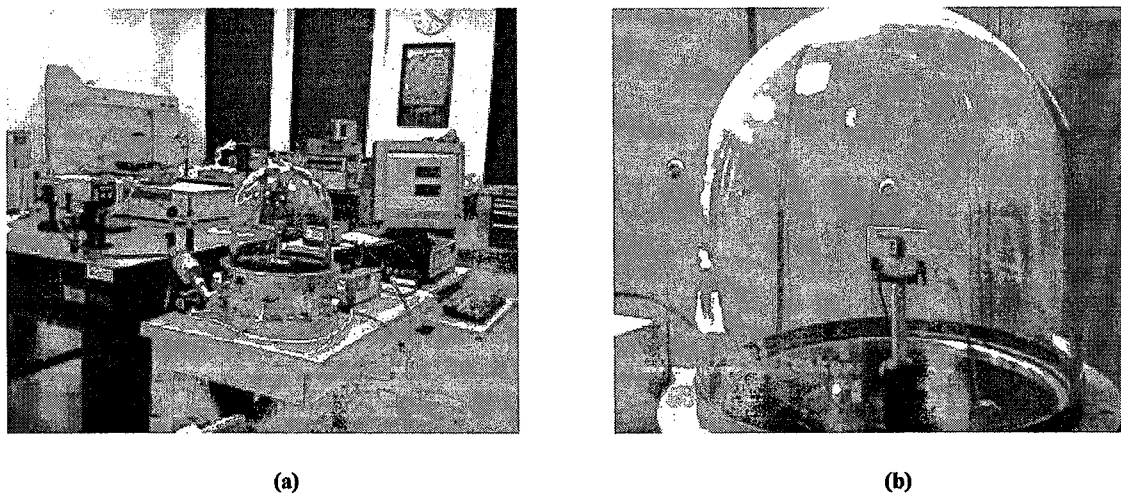


Figure 8 - Experiment setup. (a) General view of the setup. (b) Microscanner inside the vacuum chamber

3. DISCUSSION AND CONCLUSIONS

In this work, we have presented analytical expressions describing the many fundamental characteristics of comb-driven microscanners. Having an analytical and numerical tool for predicting microscanner behavior is very valuable. In linear scanners, one avoids having other resonances in the system close to the primary resonance of the scanner and its harmonics. For the nonlinear parametric resonance scanner, one should also pay attention to the subharmonic frequencies in the system. Theory presented here is applied to various science and engineering problems, but to our knowledge, this is the first time that a detailed analysis of the stability, transient and frequency behavior of a parametric resonance device is presented. Together with the analytical expressions, we have presented experimental and simulation data and they confirm the analytical predictions very well. Our analytical model is valid within small damping and small oscillation angles, but it gives a good understanding of the stability and transient response. On the other hand, our numerical model is valid for both small and large scan angles, providing a very useful tool for scanner design and characterization.

REFERENCES

1. Z. Xiaoa, W. Penga, R.F. Wolffenbuttel, K.R. Farmera, "Micromachined variable capacitors with wide tuning range," *Sensors and Actuators A*, Vol.104, p.299-305 (2003).
2. C. T. C. Nguyen, "High-Q micromechanical oscillators and filters for communications," *International Symposium on Circuits and Systems*, Proc. IEEE, p.2825-2828 (1997).
3. J. D. Grade, K. Y. Yasumura, H. Jerman, "A DRIE comb-drive actuator with large, stable deflection range for use as an optical shutter," *International Conference on Solid-State Sensors, Actuators and Microsystems*, Proc. IEEE/EDS, Boston, Massachusetts, USA (2003).
4. L.-J. Yanga, T-W. Huangb, P-Z. Changb, "CMOS microelectromechanical band-pass filters," *Sensors and Actuators A*, Vol. 90, p.148-152 (2001).
5. L. Lin, R. T. Howe, A. P. Pisano, "Micromechanical filters for signal processing," *Journal of Microelectromechanical Systems*, Vol. 7, No. 3, p.286-294 (1998).
6. V. V. Konotop, V. Kuzminak, "Parametric resonance of a defect mode in a 2D photonic crystal," *Physical Review B*, Vol. 64, p.1-7, (2001).
7. P. Wegrzyn, "Parametric resonance in a vibrating cavity," *Physics Letters A*, Vol.322, p.263-269 (2004).
8. A.A. Popov, "Parametric resonance in cylindrical shells: a case study in the nonlinear vibration of structural shells," *Engineering Structures*, Vol.25, p.789-799 (2003).
9. M-F. Yu, G. J. Wagner, R. S. Ruoff, M. J. Dyer, "Realization of parametric resonances in a nanowire mechanical system with nanomanipulation inside a scanning electron microscope," *Physical Review B*, Vol.66, (2002).
10. C. Ataman, H. Urey, "Nonlinear frequency response of comb-driven microscanners," *MOEMS Display and Imaging Systems II*, Proc. SPIE Vol. 5348 (2004).
11. H. Schenk, P. Dür, D. Kunze, H. Lakner, H. Kück, "A resonantly excited 2D micro-scanning-mirror with large deflection," *Sensors and Actuators A*, Vol. 89, p.104-111 (2001).
12. H. Schenk, P. Dür, T. Haase, D. Kunze, U. Sobe, H. Lakner, H. Kück, "Large deflection micromechanical scanning mirrors for linear scans and pattern generation," *Journal of Selected Topics in Quantum Electronics*, Vol. 6, No. 5, p.715-722 (2000).
13. H. Schenk, A. Wolter, H. Lakner, "Design optimization of an electrostatically driven micro scanning mirror," *Conf. on MOEMS and Miniaturized Systems*, Proc. SPIE, Vol. 4561, p.35-44, San Francisco, Calif., USA, (2001)
14. A. H. Nayfeh, D. T. Mook, "Nonlinear Vibrations," *Jon Wiley and Sons*, New York, (1995).
15. J.S. Rao, "Advanced Theory of Vibration," *Jon Wiles and Sons*, New York, (1992).
16. R. H. Rand, "Lecture Notes on Nonlinear Vibrations," Version 34a, Available online at <http://www.tam.cornell.edu/randdocs>, (2000).
17. K. L. Turner, S. A. Miller, P. G. Hartwell, N. C. MacDonald, S. H. Strogatz, "Five parametric resonances in a microelectromechanical system," *Nature*, Vol. 396, p.149-152 (1998).
18. J. Chen, S. Kang, "Dynamic macromodeling of MEMS mirror devices," *International Electron Device Meeting*, Proc. IEEE, p.41.5.1-41.5.4, Washington DC, USA, (2001).